Deliverable 16.3: Report on selected experiments for assessing the evolution of concrete, their mechanical safety function and performance targets

Work Package 16

This project has received funding from the European Union's Horizon 2020 research and innovation programme 2014-2018 under grant agreement N°847593.

Document information

Project Acronym	**EURAD**
Project Title	**European Joint Programme on Radioactive Waste Management**
Project Type	**European Joint Programme (EJP)**
EC grant agreement No.	**847593**
Project starting / end date	**1st June 2019 – 30 May 2024**
Work Package No.	**16**
Work Package Title	**Chemo-Mechanical AGIng of Cementitious materials**
Work Package Acronym	**MAGIC**
Deliverable No.	**D16.3**
Deliverable Title	**Selected experiments for assessing the evolution of concrete, their mechanical safety function and performance targets**
Lead Beneficiary	**COVRA**
Contractual Delivery Date	**November 2021**
Actual Delivery Date	**January 2022**
Type	**Report**
Dissemination level	**Public**
Authors	**Erika Neeft, Ton de Bruin and Roos van Kleef (COVRA), Quoc Tri Phung, Janez Perko, Suresh, Seetharam, Kristel Mijnendonckx and Xianling Li (SCK CEN), Lucie Hausmannová (SURAO), Radek Vašíček (CTU), Petr Večerník (UJV), Veronika Hlaváčková and Kateřina Černá (TUL), Tomáš Černoušek (CV Řež), Olivier Helson, Xavier Bourbon and Jad Zghondi (ANDRA), Thierry Vidal and Alain Sellier (LMDC/INSA Toulouse-UPS), Jianfu Shao and Thomas Rougelot (LaMcube/CNRS), Kyra Jantschik (GRS), Johannes Kulenkampff (HZDR), Guido Deissmann (FZJ), Michele Griffa (Empa), Sergey Churakov, Thomas Gimmi and Bin Ma (PSI)**

To be cited as:

Neeft E., de Bruin T., van Kleef R., Phung Q T., Perko J., Seetharam S., Mijnendonckx K., Li X., Hausmannová L., Vašíček R., Večerník P., Hlaváčková V., Černá K., Černoušek T., Helson O., Bourbon X., Zghondi J., Vidal T., Sellier A., Shao J., Rougelot T., Jantschik K., Kulenkampff J., Deissmann G., Griffa M., Churakov S, Gimmi T., Ma B. (2021): Selected experiments for assessing the evolution of concrete, their mechanical safety function and performance targets. Final version as of 28.01.2022 of deliverable D16.3 of the HORIZON 2020 project EURAD. EC Grant agreement no: 847593.

Disclaimer

Acknowledgement

This document is a deliverable of the European Joint Programme on Radioactive Waste Management (EURAD). EURAD has received funding from the European Union's Horizon 2020 research and innovation programme under grant agreement No 847593.

Status of deliverable		
	By	Date
Delivered (Lead Beneficiary)	E. Neeft (COVRA)	04 November 2021 (draft) 06 December 2021 (Revised) 20 January 2022 (Revised)
Verified (WP Leader)	A. Dauzères (IRSN)	13 November 2021 (first review) 10 December 2021 (initial version validated) 27 January 2022 (final version validated)
Reviewed (Reviewers)	J. Zghondi (ANDRA)	19 & 29 November 2021
Approved (PMO)	B. Grambow (PMO)	10 January 2022
Submitted to EC (Coordinator)	ANDRA	28 January 2022

Executive Summary

Cementitious materials are used in disposal facilities for radioactive waste as a construction material to ensure a safe operation of this facility for example the lining. These materials can also be used to contribute to the containment of radionuclides in the post-closure phase. The required mechanical strength class of concrete is determined by its function. The strength of concrete is determined by the strength of millimetre sized aggregates and the attachment of these aggregates with the cementitious phase in concrete. Only samples of concrete with aggregates are therefore included in this report since Task 2 of EURAD Work Package MAGIC is dedicated to study the chemo-mechanical behaviour at the macro scale i.e. for centimetre and decimetre sized samples.

The required strength class for a construction material is usually higher than the required strength for a containment material especially if unreinforced concrete is used. It may take several trials to obtain a concrete recipe that can achieve the required strength after 28 days of hardening. The concrete also needs to maintain the majority of this strength during the operation of the disposal facility. The service life of a disposal facility can be 100 years or more for many countries. The hardening process may continue during the operational life by which the strength of concrete increases. This increase in strength has been measured for the Czech, Dutch and French samples. For well cured concrete, there can also be an additional contribution in strength by the suction force of empty pores within the concrete as have been determined by the studies on the Dutch samples. Concrete may also need to maintain its strength for a required period in the post-closure phase. The strength of concrete is highly related to the permeability of concrete i.e. a higher strength of concrete is also less permeable hence the rate of ingress of species that can alter the chemistry of concrete is smaller. Some alterations may result into a decrease in strength of concrete.

Luckily, a lot of knowledge has been generated by civil engineering and this knowledge has been translated into standards. Two examples with this known decrease in strength are highlighted:

- Reaction between siliceous aggregates and cementitious phase by which the strength of the aggregates is reduced;
- Formation of a sulphate mineral within the cementitious phase by which the aggregates become less strongly hold together by which the strength of the concrete is reduced.

A too early loss in the mechanical strength of concrete by a reaction between the siliceous aggregates and the cementitious phase in concrete can be prevented by following these standards although irradiation of cementitious materials by the radionuclides contained in a waste form may introduce some special considerations. The reaction is caused by a specific polymorph of silica and a high alkali content of cement. Quartz is a polymorph of silica with such a low reactivity with this cementitious phase that the strength of the aggregate is not reduced. Irradiation can however change the polymorph of quartz into polymorph of silica that is more reactive with such high alkali content cementitious phase. Prevention in the framework of the handling radioactive waste can then take place by choosing a concrete recipe by which quartz aggregates are replaced by non-siliceous aggregates or replacing the cement with a high alkali content for a lower alkali content. Consequently, these considerations are known and this detrimental reaction can therefore be prevented by a careful selection of the ingredients for the concrete recipe to manufacture concrete. The reaction with siliceous aggregates can be excluded for most of the samples studied in Task 2 of MAGIC.

Delayed ettringite formation (DEF) is another familiar process in which the strength of concrete is too early lost by ingress of dissolved sulphate reacting with a calcium aluminium mineral into ettringite. DEF can also be prevented by a careful selection of the type of cement used to manufacture concrete and considering the exposure environment of concrete. This carefulness is especially required for saline environments for example the pore water in crystalline and clay formations. The pore water chemistries in these formations are country specific. There are countries that consider geological formations with fresh water. DEF can considered to be negligible in those environments.

The chemo-mechanical evolution of concrete is a very slow process, especially when the existing standards for civil engineering have been followed and blended cements have been used to

manufacture concrete. Mainly concrete from existing experiments have therefore been selected. Concrete made with blended cements usually has a smaller permeability than concrete made with Ordinary Portland Cement. The samples studied within MAGIC are frequently manufactured with blended cements. All samples in Task 2 of MAGIC are being exposed or have been exposed to disposal representative conditions for several years. These conditions are frequently limited to chemical representative conditions; microbiological conditions are unknown. The chemical exposure may result into a gaseous carbonation of concrete by which the pH of the concrete pore water is reduced or a complex chemical alteration of cement minerals in the cementitious phase by exposure of concrete to a multi-ionic solution. This multi-ionic solution can be present in clay. The ingress of dissolved species can be smaller for concrete exposed to clay compared to concrete exposed to a solution. All samples are made of plain concrete except in the French programme that also considers reinforced concrete, knowing that corrosion of the steel bars is favoured by initial defects and that this corrosion is responsible in the long term for the mechanical degradation of a structure such as a lining. Not all linings are manufactured with reinforced concrete for example unreinforced concrete has been for the lining in the underground research laboratory in Mol (Belgium).

There are three types of exposures to concrete samples within MAGIC:

1. Clay and ventilation air in underground research laboratories i.e. lining;
2. Air with a natural carbon dioxide concentration of 0.04% or far larger concentrations of CO2;
3. Underground pore water only.

The exposed concrete in a lining in underground laboratories have the combined effect of the mechanical loading of concrete and ingress of gaseous and dissolved species. Belgian and French samples have this chemo-mechanical combination. Samples of concrete need to be taken by drilling or sawing and the number and size of samples is limited in order to preserve the construction. Both, the size of the samples and the number of samples are however very important to measure reliably the strength of concrete with the current available standards. It is therefore strongly advised to make many concrete samples with the same concrete recipe from which the lining has been made by which the detrimental effects of the exposure environment to the strength of concrete can be monitored for example sequentially in decades.

The difference between a strength measurement from mechanically loaded samples and with ingress of dissolved species and strength measurement from a mechanically unloaded sample and with ingress of dissolved species is yet unknown. In Task 2, the strength of concrete is mainly measured from samples that have been exposed to dissolved species in a mechanically unloaded state.

Sample preparation and the early age treatment have a high impact on the measured strength. The mixing of ingredients, curing conditions and sawing samples from larger concrete specimens can all have an influence on the measured strength. After 3 years of exposure, the studies performed on the Dutch samples showed that the samples made by sawing of hardened concrete have a significantly smaller strength than only casted samples.

Following the standards, carbonation of concrete is considered as a process that is detrimental to the strength of reinforced concrete. Ingress of dissolved magnesium can be detrimental to the strength of reinforced and unreinforced concrete. A range in dissolved magnesium concentrations is considered in MAGIC. The solutions with dissolved magnesium also have other dissolved species that can be found in saline water. The dissolved concentration of magnesium ranges from as saline as brackish water till more than saline as seawater in Task 2 of MAGIC. Concrete in MAGIC is either exposed to these saline solutions or fresh solutions in which the dissolved concentration of magnesium is negligible. The solutions can be present in clay to which concrete is exposed.

Only for the Dutch samples, preliminary results of the macro scale impact of a multi-ionic solution with dissolved magnesium is available. The studies on these samples that were exposed to a solution as saline as seawater for 5 years showed a decrease in compressive strength for the lower strength class samples. After 5 years of exposure, the measured compressive strength was not decreased for the

higher strength samples. This difference between results in strength class is currently attributed to the higher porosity and larger size in pores of the lower strength concrete by which the ingress rate of detrimental dissolved species such as magnesium was larger for the lower strength concrete than the higher strength concrete. No microbial studies have yet been performed.

Microbial activity can have an impact on the rate of precipitation of secondary minerals for example biogenic calcite followed by an alteration of the dissolution of cement minerals inside concrete. This activity is envisaged to be negligible by space restriction especially within higher strength concrete that usually have a small porosity and refined pore structure. This activity cannot yet be excluded for concrete with cracks and lower strength concrete with a higher porosity and large size in pores. Apart from ingress of species, also the additional impact of microbial activity is therefore studied in Task 2 of MAGIC.

Table of content

Executive Summary 4

Table of content 7

List of figures 10

List of Tables 13

1. Introduction 16

1.1 Some available knowledge for manufacturing concrete 16

1.2 Construction for safe operation of the facility 18

1.3 Preparation of the post-closure phase 20

1.4 References 21

2. Characteristics of samples studied in MAGIC 22

2.1 Rationale of sample size 22

2.2 Type of cement 23

2.3 Limitation of water content in concrete recipe 24

3. Age, exposure and available strengths of concrete samples 26

4. Belgian samples 29

4.1 Mechanical safety function and performance target 29

4.2 Size of samples, concrete recipe 29

4.3 Available characterisation of cementitious material 30

4.3.1 Mechanics 30

4.3.2 Chemistry 34

4.4 Description of experimental set-up 35

4.4.1 Part A: Microstructure and mineralogical characterization 37

4.4.2 Part B: Determination of transport properties 37

4.5 Characterisation of cementitious material to be performed in MAGIC 40

4.5.1 Mechanics 40

4.5.2 Transport properties 40

4.5.3 Chemical and mineralogical properties 40

4.5.4 Microbical 41

4.6 References 42

5. Czech samples 43

5.1 Mechanical safety function and performance target 43

5.2 Size of the samples, concrete recipe 43

5.3 Characterisation of the cementitious material 43

5.3.1 Mechanics 44

5.3.2 pH 44

5.4 Description of the experimental set-up 45
5.5 Characterisation of the cementitious material to be performed in MAGIC 45
5.5.1 Planned analysis 45
5.6 References 52
6. Dutch samples 54
6.1 Mechanical safety function and performance target 54
6.1.1 Buffer 55
6.1.2 Backfill 57
6.1.3 Expected chemo-mechanical evolution 57
6.2 Size of samples, concrete recipe 59
6.3 Available characterisation of cementitious materials 60
6.3.1 Mechanics 60
6.3.2 Chemistry 72
6.4 Description of experimental set-up 78
6.5 Characterisation of cementitious material to be performed in MAGIC 78
6.5.2 Chemistry 78
6.5.3 Microbiology 79
6.6 References 80
7. French samples 82
7.1 Mechanical safety function and performance target 82
7.2 Size of samples, concrete recipe 83
7.3 Available characterisation of cementitious material 86
7.3.1 Mechanics 87
7.3.2 Chemistry 89
7.3.3 Microbiology (if available) 92
7.4 Description of experimental set-up 92
7.5 Characterisation of cementitious material to be performed in MAGIC 92
7.6 References 94
8. German samples 95
8.1 Mechanical safety function and performance target 95
8.2 Size of samples, concrete recipe 95
8.3 Available characterisation of cementitious material 95
8.3.1 Mechanics 96
8.3.2 Chemistry 96
8.4 Description of experimental set-up 97
8.4.1 Part A: Flow through of corrosive solutions through low-pH concrete 97

8.4.2 Part B: Determination of material strength dependent on degree of degradation 98
8.5 Characterisation of cementitious material to be performed in MAGIC 98
8.5.1 Mechanics 98
8.5.2 Chemistry 100
8.6 References 101
9. Swiss samples 102
9.1 1 Mechanical safety function and performance target 102
9.2 Size of samples, concrete recipe 103
9.2.1 Introduction: Casting, curing and specimen preparation history 103
9.2.2 Mix design and detailed history of each barrel 107
9.3 Available characterisation of cementitious material 113
9.3.1 Poromechanics 113
9.3.2 Chemistry 114
9.4 Description of experimental set-up 115
9.5 Characterisation of cementitious material to be performed in MAGIC 116
9.5.1 Poromechanical characterisations 116
9.5.2 Chemical and mineralogical characterizations 120
9.6 Time plan vs delivered data/information 121
9.7 References 122
Appendix A. Template 126
Appendix B. Properties used for the calculations in the description of the Dutch samples 129

List of figures

Figure 1-1: Disposal cells in the operational phase before emplacement of a waste package, ingress of species are indicated with an arrow, solid ones are considered to be detrimental for the mechanical strength of (reinforced) concrete. Host rocks: crystalline rock, poorly indurated clay and indurated clay. 19

Figure 4-1: Concrete used for disposal gallery lining, buffer, and backfill in high level waste facility – Belgian Supercontainer concept 29

Figure 4-2: Cumulative pore volume and pore size distribution of lining concretes obtained by N_2-adsorption (top) and MIP (bottom)..... 32

Figure 4-3: An example of SEM imaging analysis procedure to obtain the pore size distribution: (a) original SEM image, (b) binary segmented image (black = pore), (c) SEM cumulative porosity and pore size distribution and (d) an example of pore size measuring and counting, in which the different pores are numbered (1 to 21). 33

Figure 4-4: Pore size distribution for lining and supercontainer concrete, combined from N_2-asdsorption, MIP and SEM measurements..... 34

Figure 4-5: Chemical evolution of the concrete toward the interface – measured in 2 mm thickness from the interface 35

Figure 4-6: In-situ drilling procedure: (a) Drilling small hole using guiding system; (b) Two small holes for resin filling; (c) Resin filling into two small holes to make two anchors after polymerization; (d) Dry drilling concrete-clay interface after reinforcing by anchors; (e) Concrete-clay interface sample after retrieving from drilling bit; and (f) Sample packaged in aluminium foil 36

Figure 4-7: Schematic test setup for percolation experiment – the percolation cell (left) composes (1) steel lid, (2) steel body, (3) inner polycarbonate body, (4) bolt, (5) inner O-ring, (6) outer O-ring, and (7) threaded rod. 37

Figure 4-8: Schematic test setup for permeability determination 38

Figure 4-9: Schematic experimental setup to measure diffusivities of dissolved gases (Jacops et al., 2013; Phung, 2015; Phung et al., 2015)..... 39

Figure 4-10 Schematic experimental setup to measure water sorptivity 39

Figure 6-1: Cross section of a closed disposal cell considered in COVRA's research programme. 55

Figure 6-2: Calculated temperatures within the concrete buffer in the operational phase of the disposal process; heat source (blue): 200 W, heat transfer coefficient: 0.25 W m-2K-1, steel and concrete (buffer and floor) properties in Appendix..... 56

Figure 6-3: Calculated temperatures at two interfaces as a function of time and calculated pressures at these interfaces at the mid of the heat source without floor (solid) and with floor (dashed) lines. 56

Figure 6-4: Temperature as a function of time at different interfaces for the geometry shown in Figure 6-1 in which the pedestal is assumed to have the same properties as the backfill for simplicity. 57

Figure 6-5: Cross section of the experimental set-up for exposure of certified concrete samples to a relative humidity. 61

Figure 6-6: Compressive strength of buffer-like material as a function of the relative humidity at 20°C 62

Figure 6-7: Compressive strength of buffer liker material as a function of the relative humidity at 5°C; samples on which salt has been observed on the surface are marked red. 63

Figure 6-8: Compressive strength of backfill samples as a function of the relative humidity at 20□C. Samples on which salt has been observed on the surface are marked red. 65

Figure 6-9: Compressive strength of backfill samples as a function of the relative humidity at 5□C. Samples on which salt has been observed on the surface are marked red. 66

Figure 6-10: Total loss of water after achieving a constant in weight as a function of the relative humidity at 20°C for buffer-like material. 68

Figure 6-11: Total loss of water after achieving a constant in weight as a function of the relative humidity at 5°C for buffer-like material. 69

Figure 6-12: Distribution in size of pores determined at 20°C and 5°C for buffer-like material. 69

Figure 6-13: Total loss of water after achieving a constant in weight as a function of the relative humidity at 20°C for the backfill. 70

Figure 6-14: Total loss of water after achieving a constant in weight as a function of the relative humidity at 5°C for the backfill. 70

Figure 6-15: Distribution in size of pores determined at 20°C and 5°C for backfill. 71

Figure 6-16: Determination of the Genuchten parameters for the buffer-like material and backfill assuming a residual water content of zero. 72

Figure 6-17: Saturation degree with the Genuchten parameters. 72

Figure 6-18: Carbonation rims at 20°C for buffer-like material after 1000 days exposure to a relative humidity of cubical samples with an edge of 5 cm, blue arrow is 1 cm. 74

Figure 6-19: Carbonation rims at 20°C for (certified) backfill after 1000 days exposure to a relative humidity of cubical samples with an edge of 5 cm, blue arrow is 1 cm. 75

Figure 6-20: Oxidation at 20°C for buffer-like material after 1000 days exposure to a relative humidity of cubical samples with an edge of 5 cm. 76

Figure 6-21: Oxidation at 5°C for buffer-like material after 1000 days exposure to a relative humidity of cubical samples with an edge of 5 cm. 76

Figure 6-22: Oxidation at 20°C for backfill after 1000 days exposure to a relative humidity of cubical samples with an edge of 5 cm. 77

Figure 6-23: Fractured surfaces of a cubical samples with an edge of 5 cm, buffer-like material (left), backfill sample (right). Samples exposed for 4.5 years to a synthetic clay pore water solution. 77

Figure 7-1: Measured compositions at a depth of -430, -460, -475, -504 m in the Callovo-Oxfordian Clay in Bure and estimation based on the experimental results of the water circulation experiment at -505 m [2]. 82

Figure 7-2: Schematic section of a long-lived intermediate-level waste disposal cell. 83

Figure 7-3: Evolution of compressive strengths as function of time for CEM I and CEM V concretes [11]. 87

Figure 7-4: Evolution of elastic modulus as function of time for CEM I and CEM V concretes [11]. 88

Figure 7-5: Comparison of creep curves between sound concretes and leached ones [12]. 88

Figure 7-6: Result of mercury porosity distribution and pore inlet diameter distribution [16]. 89

Figure 7-7: TGA and DTG curves obtained on carbonated CEM I concrete [10] 90

Figure 7-8: ATG and DTG curves obtained on sound and carbonated cement paste [9] 91

Figure 7-9: *Diffractogram of carbonated cement paste [9]* 91

Figure 7-10: Experimental setup to carry out pull-out test. 93

Figure 7-11: Experimental setup for the triaxial (left) and creep tests (right) [16]. 93

Figure 9-1: Conceptualization of the repository design for the high-level waste [1] 103

Figure 9-2: Cross section of a L/ILW repository emplacement cavern after closure (left) and possible design of the longitudinal section of the L/ILW emplacement cavern (right) [2] 103

Figure 9-3: Example of the high energy X-ray tomography measurements configuration, which were performed on the barrels to approximately locate the position of the Opalinus Clay (OPA) core embedded in the cast concrete/mortar. The X-ray beam, produced by a compact linear electron accelerator (LINAC), was collimated to produce a so-called fan beam, which irradiates the investigated object only at one position along its vertical height (Z-axis in the photo). X-ray tomography was performed, for each barrel, only at three heights along such direction, thus producing only three 2D cross-sectional images (tomographic slices). Such slices provided the internal reconstruction of the barrel at the respective heights. The photon beam energy was 6 Mev. The pixel size of each tomographic slice was 0.2 mm. 105

Figure 9-4: An example of results from high energy X-ray tomography of the barrels. The image on the left side shows one tomographic slice acquired for the barrel of the interface system 2276 (photograph on the right side, see below for that barrel's details), where the OPC concrete was cast around the Opalinus Clay (OPA) core. The horizontal dashed red line in the photograph on the right provides an indication of the barrel's height at which the slice on the left was reconstructed by high energy X-ray tomography. The pixel size of the tomographic slices was always 0.2 mm. Brighter grey pixels indicate higher local X-ray attenuation, due to either higher local mass density or higher local effective atomic number or a combination of the two. The bright, concentric rings in the slice are tomographic reconstruction artefacts, called ring artefacts, stemming from defective X-ray detector's pixels. 106

Figure 9-5: . Example of slicing off of the top part of a barrel, containing only/mainly concrete/mortar, to provide access for coring/cutting specimens in the concrete/mortar volume and surrounding the Opalinus Clay (OPA) core. The barrel in this case was the one containing the interface system 2278 (ESDRED mortar/OPA interface) described below. 106

Figure 9-6: Example of choice of locations for specimen coring from one sliced-off barrel and of respective specimen labeling scheme. The barrel was the one of the interface system 2277 (OPC mortar/Opalinus Clay (OPA) core, see details below). The locations labelled as AY, ∀ Y=1,2,…, were for cylindrical cores of 28 mm diameter directly close to the interface. The locations labelled as BY, ∀ Y=1,2,…, are for 28 mm-diameter cores whose centers were about 45 mm away from the interface. The CY, ∀ Y=1,2,…, labelled locations were also for 28 mm-diameter cores 10 mm away from the barrel's external boundary and with center about 60-65 mm far away from the interface. 107

Figure 9-7: View of the setup for performing SIngle MOde linear and Nonlinear Resonant Ultrasound Spectroscopy (SIMO(N)RUS) measurements on rod-like (i.e., elongated) specimens under controlled temperature and relative humidity (RH) conditions. The specimen (in this example, a cylindrical Berea sandstone core, 28 mm in length, 150 mm in diameter) hangs on plastic supports located at the nodal regions for its 1st longitudinal vibration eigenmode, in order to realize stress-free boundary conditions (BC). It is excited by a piezoelectric disk attached to its bottom side. The corresponding vibration signal is measured in a non-contact way by a single point Laser Doppler Vibrometer (LDV). The specimen is located inside a glove box conditioned at a chosen RH value by the use of a respective supersaturated salt solution laid in containers and by additional, external air conditioners. The LDV is located outside of the glove box, its laser beam shining on the specimen's top surface through a small window on one side of the glove box. 118

List of Tables

Table 1-1: The three exposure classes for groundwater according to EN 206 17

Table 1-2: Some examples of ranges in blends of commercially available types of cement according to EN 206 18

Table 2-1: Size of aggregates, sample size and specification of loading 22

Table 2-2: Combination of aggregates and cement 23

Table 2-3: Water to cement ratio and porosity of the samples studied in MAGIC 24

Table 3-1: Measurements of compressive strength and strength class 26

Table 3-2: Years of exposure of samples at start of MAGIC 27

Table 4-1: Mix compositions of in-situ concrete: SP – Superplasticizer 29

Table 4-2: Microstructural properties of lining concretes characterized by N_2-adsoprtion 31

Table 4-3: Summary of measured properties. 34

Table 5-1: LPC_SURAO recipe 43

Table 5-2: Compressive strength, modulus of elasticity and pH of LPC_SURAO (N.A. = not analysed) 44

Table 5-3: Overview of the planned analysis 46

Table 5-4: Overview of the planned analysis of the samples (performed -x, not performed – o) 50

Table 5-5: Primers used for the 16S rRNA amplicon sequencing 50

Table 5-6: Primers used for the qPCR analysis of bacterial metabolic communities 51

Table 6-1: Recipe for the synthetic pore solution to which buffer-like samples and samples of backfill have been exposed 58

Table 6-2: Mortar recipe for 6 buffer-like samples casted in 30 June 2015 and 1 July 2015 59

Table 6-3: Mortar recipe for backfill samples casted 9 May [a] 2016 and 17 May [b] 2016 59

Table 6-4: Mortar recipe for buffer-like samples casted 13 July 2016 59

Table 6-5: Mortar recipe for backfill samples casted 6, 8 and 9 September 2016 60

Table 6-6: Compressive strength and weight of buffer-like materials measured on 9 August 2016 of samples casted on 13 July 2016. 60

Table 6-7: Compressive strength and weight of sawn buffer-like samples measured on 18 January 2017 61

Table 6-8: Relative humidity's to which samples have been exposed. 61

Table 6-9: Compressive strength of buffer-like samples with an edge of 5 cm exposed at around 20°C. 64

Table 6-10: Compressive strength and weight of certified backfill samples. 64

Table 6-11: Compressive strength and weight of sawn backfill samples measured on 18 January 2017. 65

Table 6-12: Compressive strength of backfill samples with an edge of 5 cm exposed at around 20°C. 66

Table 6-13: Compressive strength and weight of backfill CEM III samples casted on 9 May 2016. 67

Table 6-14: Compressive strength and weight of backfill CEM I samples casted on 17 May 2016. 67

Table 6-15: Genuchten parameters determined with a best fit by the eye 71

Table 6-16: Average oxide compositions of the two types of cement in wt%. 73

Table 6-17: Mineralogical composition from average oxide compositions. 73

Table 6-18: Assumed concentrations of minerals in the samples after 28 days. 73

Table 6-19: Modelled and measured pore water chemistries for mortar or paste fabricated with CEM I and CEM III (Neeft et al., 2019) 74

Table 7-1: Reference concrete recipe 83

Table 7-2: Summary of the number of tests per action for the LaMcube: C40/50 concrete 84

Table 7-3: Summary of the number of tests by action for LMDC: C40/50 concrete 84

Table 7-4: Time and exposure conditions of the materials 86

Table 7-5: Mechanical and physical properties of the CEM I concrete [10]. 86

Table 7-6: Summary of characterization tests with porosity accessible to water values and dispersion of results (Andra data compilation). 89

Table 7-7: Mineralogical Composition of Concrete [17] 90

Table 7-8: Chemistry of concrete pore solution studied [18] 92

Table 7-9: Estimated planning of tests by action for the LaMcube 93

Table 8-1: Formulation of low-pH-cement S5 [Herold et al 2020] 95

Table 8-2: Compressive strengths of low-pH cement S5 [Herold et al 2020] 96

Table 8-3: Young's modulus of low-pH cement S5 [Herold et al 2020] 96

Table 8-4: Composition of the components of low-pH-cement S5 [Herold et al 2020] 96

Table 8-5: Parameter for "Konrad-solution" at 25°C [Herold et al 2020] 97

Table 9-1: Mix design [4]; Water-to-binder ratio (w/b): 0.5 108

Table 9-2: Specimen size and Nr. of specimens per size 108

Table 9-3: Average distance from the concrete/OPA core interface 108

Table 9-4: Mix design [4]; water-to-binder ratio (w/b): 1.08 109

Table 9-5: Specimen size and Nr. of specimens per size 109

Table 9-6: Average distance from the concrete/OPA core interface 109

Table 9-7: Mix design[§]; Water-to-binder ratio (w/b): 0.8 110

Table 9-8: Specimen size and Nr. of specimens per size 110

Table 9-9: Average distance from the concrete/OPA core interface 110

Table 9-10: Mix design[†]; water-to-binder ratio (w/b): 0.47; fresh mass density (kg m^{-3}): 2050 111

Table 9-11: Specimen size and Nr. of specimens per size 111

Table 9-12: Average distance from the concrete/OPA core interface 111

Table 9-13: Mix design[†]; water-to-binder ratio (w/b): 0.5; fresh mass density (kg m^{-3}): 1860 112

Table 9-14: Specimen size and Nr. of specimens per size 112

Table 9-15: Average distance from the concrete/OPA core interface 112

Table 9-16: 90-day compressive strength of the same type of concrete cast in the barrels, as reported in a technical note accessible only to the CI campaign's partners. The average of three values measured on respective specimens and according to the SN EN 12390-3 standard was reported in such technical note. 113

Table 9-17: Local porosity values of the three distinct concrete types as measured by ^{14}C MMA-based autoradiography for regions at distinct average distances from the concrete/OPA interfaces. Adaptation from [7] and from a technical report of the CI experimental campaign available only to the campaign's partners. 114

Table 9-18: 90-day mass density measurements performed according to the SN EN 12390-7 standard on the same specimens used for the 90-day compressive strength measurements. Since such specimens were stored for 90 days under water, the measured values refer to a water-saturated state. The values are the average ones from the three distinct specimens, for each concrete type. They were documented in a technical report available only to the partners of the CI experimental campaign. ... 114

1. Introduction

Cementitious materials are used as a construction and containment material in the implementation of disposal of radioactive waste. Examples are linings for the construction of galleries in the disposal facility that are required for a safe operation of this facility and concrete buffers and plugs to contribute to the containment of radionuclides in the post-closure phase of the disposal system. These cementitious materials have in common that these materials are manufactured with aggregates. The strength of concrete is determined by the strength of aggregates and the attachment of the aggregates with the cementitious phase in concrete. For reinforced concrete, also the attachment between steel and the cementitious phase is important. Steel rebars have usually ribbons and are commonly oxidised in air before concrete pouring in order to obtain a well attachment between concrete and steel. Gaps between steel and the cementitious phase of concrete may arise due to shrinkage of the cementitious phase during hardening when polished and smoothen steel is used.

The chemo-mechanical behaviour at the macro scale is studied in Task 2 of the EURAD Work Package MAGIC. Therefore, only reinforced concrete and cementitious materials with aggregates are considered. The cementitious materials investigated in Task 2 are already used, are envisaged to be used in the disposal facility or are being tested within a range of other cementitious materials. There are samples drilled or sawed from existing underground facilities in Belgium and France. There also samples that have been fabricated as part of the Czech, Dutch, French, German or Swiss programme.

The description of all samples, the available and future mechanical, chemical and microbiological characterisation, the type of chemical and microbial exposure and whether exposure includes mechanical loading can be found in Chapter 4 till 9. These descriptions have been made by completion of a template (see Appendix A). This Chapter continues with some available civil engineering knowledge that can be used for the manufacturing of concrete and expected loadings in the disposal facilities. Chapter 2 overviews common characteristics of the MAGIC samples in line with this available knowledge. Chapter 3 focusses on the available mechanical characteristics of the samples in Task 2, age and their exposure environments.

1.1 Some available knowledge for manufacturing concrete

A choice needs to be made in features such as type of cement, cement content and the use of reinforced concrete in order to make an appropriate design of the construction and closure of the disposal facility. The required strength of concrete, environmental class, fluidity during pouring and distribution in size of aggregates have all been defined before fabrication of any cementitious material. Choices in concrete recipe and type of mixing of ingredients follow from these requirements and available knowledge. This available knowledge is integrated in standards for civil engineering. These standards are regularly updated. The European standard EN 206 divides the potential degradation of concrete or the reinforcement inside the concrete into 18 exposure classes. There are three exposure classes for ranges in dissolved sulphate content, pH, amount of dissolved CO_2, dissolved ammonium and magnesium content. Table 1-1 shows the ranges and the associated requirements for these ranges for a specified minimum in strength class.

Table 1-1: The three exposure classes for groundwater according to EN 206

Environmental class	XA1	XA2	XA3
Dissolved species			
SO_4^{2-} [mg/l]	200 to 600	600 to 3000	3000 to 6000
pH	5.5 to 6.5	4.5 to 5.5	4.0 to 4.5
CO_2 [mg/l]	15 to 40	40 to 100	≥ 100
NH_4^+ [mg/l]	15 to 30	30 to 60	60 to 100
Mg^{2+} [mg/l]	300 to 1000	1000 to 3000	≥ 3000
Requirements			
Water to cement ratio	0.55	0.50	0.45
Cement content [kg m^{-3}]	320	340	360
Minimum in strength class for indicated w/c and cement content	C30/37	C30/37	C32/40
Concrete cover [mm]	30	35	40

All these complexes are also present in the pore water of clay and crystalline host rock except for dissolved ammonium which is characteristic for polluted groundwater. Polluted groundwater may not be relevant for disposal studies. The environmental class determines many requirements. For example, reinforced concrete being exposed to the highest magnesium concentration (XA3) requires:

- The smallest water to cement ratio since this ratio has an impact on the permeability of concrete and thereby ingress rate of dissolved magnesium. A small permeability is characteristic for a concrete with a high strength and has the smallest ratio in water to cement;
- The largest cement content in order to buffer the ingress of magnesium;
- The largest concrete cover in order to delay, minimize and sometimes even prevent detrimental species reaching the steel bar being most close to the interface between concrete and for example air or clay. Species in air or clay can increase the corrosion rate of steel for example oxygen in air and chlorine in clay pore water. The corrosion rate of steel is minimized if steel is exposed to a reducing, alkaline conditions since a passivation layer on the steel surface that limits corrosion is stable at these chemical conditions. Consumption of oxygen by corrosion of steel can deplete oxygen in the vicinity of the steel bar by which aerobic corrosion is followed by a lower anaerobic corrosion rate. Higher aerobic corrosion rates caused by the insufficient coverage of the steel bar by concrete may result into the spallation of concrete during the operational phase of the disposal facility. Especially if carbonation of the concrete cover has occurred by which the alkaline environment is no longer provided. Aerobic corrosion rates are higher when too much chlorine has achieved the rebar.

Dissolved magnesium and sulphate are present in saline solutions such as seawater. Chlorine is also present in seawater and even in higher amounts than magnesium and sulphate. Please note that chlorine is not included in Table 1-1 since the ingress of chlorine may not be detrimental to the strength of concrete. Ingress of chlorine may result into Friedel-salt precipitation which reduces the porosity of concrete and this reduction may result in an increase of the mechanical strength of concrete. Another process that results into a decrease in porosity and thereby increasing locally the concrete's strength is precipitation of calcite. This calcite precipitation occurs by reaction of cementitious minerals with CO_2 and bicarbonate.

Ingress of gaseous and dissolved species may alter the chemical composition of the cementitious phase in concrete. There are chemical alterations in which the mechanical strength of fabricated concrete is too early too much decreased in the operational phase of the disposal facility or in the post-closure phase of the disposal system. These alterations can be prevented with a proper choice in:

- Type of cement;
- Content of cement in concrete
- Combination of type of cement and type of aggregates.

These alterations and therefore not studied within MAGIC. For example, sulphate resistant cement is used to prevent Delayed Ettringite Formation (DEF). DEF can be caused by:

- An internal sulphate attack when the temperate during hydration has achieved a too high value;

- An external sulphate attack by ingress of dissolved sulphate species reacting with tri calcium aluminate (C_3A).

The hardened cement between the aggregates is cracked. Both cases of DEF can be prevented by limiting the C_3A concentration. A Portland cement blended with microsilica, fly ash or slag also reduces the temperature for hydration by which internal sulphate attack is prevented. These blended cements can be called sulphate resistant cements for example CEM III/B. Table 1-2 shows examples of ranges in blends. The range in amount of fillers to these cements is 0 to 5 wt%.

Table 1-2: Some examples of ranges in blends of commercially available types of cement according to EN 206

Main constituent	Cements	Clinker [wt%]	Blast furnace slag [wt%]	Microsilica [wt%]	Pozzolan [wt%]	Fly ash [wt%]
CEM I	CEM I	95-100	-	-		-
CEM II	CEM II/A-D	90-94		6-10		
	CEM II/A	80-94				6-20
	CEM II/B	65-79				21-35
CEM III	CEM III/A	80-94	36-65			
	CEM III/B	20-34	66-80			
CEM V	CEM V/A	40-64	18-30		18-30	
	CEM V/B	20-38	31-50		18-30	

Concrete made with blended cements are called low-permeability concretes due to their more refined pore structure compared to concrete made with Portland cement (Atkins, et al. 1991) (Atabek et al. 1991) (Jackson, et al. 2017). Another example of a proper choice to prevent chemical alteration in which the mechanical strength of fabricated concrete is too early too much decreased is using calcite or quartz aggregates instead of aggregates with silica polymorphs. For example, chalcedony, a siliceous mineral, reacts with the alkalis in the concrete pore water into the formation of silica gels; cracks become present through the reactive siliceous aggregates. The use of blended cements also reduces the probability of the alkali silica reaction (ASR) due its low-permeability.

1.2 Construction for safe operation of the facility

A concrete lining is applied to crystalline and clay host rocks. The emplacement technique of this lining highly determines how well the concrete can be cured. Curing has an important impact on the achieved mechanical strength of concrete. The period in time at which a particular strength is necessary for safety depends on the strength of the host rock and its interaction with the lining.

- Lining made by emplacing pre-fabricated concrete segments:
  - Poorly indurated clay: Concrete segments need to be applied directly after excavation of poorly indurated clay due to the fast convergence of this clay. These segments are cured and hardened at well controlled above ground conditions. Direct emplacement of these segments takes place through a special designed tunnel boring machine. The lining provides mechanical support and is necessary in order to have sufficient time to emplace the waste packages in the disposal facility.
  - Indurated clay: For LILW disposal cells in indurated clays, such controlled cured and hardened concrete are considered as well, except that a pre-fabricated compressible layer is present between the extrados of the concrete segment and indurated clay.
- Lining made with in-situ curing of concrete:
  - There is more time available to apply a lining after excavation of crystalline and indurated clay rock compared to poorly indurated clay since the convergence of indurated clay and crystalline rock is very slow. The lining is usually applied with shotcrete after excavation of a whole gallery. Depending on the fracture extent of the host rock by drilling or blasting to excavate the rock, also bolts and anchors may be required apart from (reinforced) shotcrete. Hereto, sufficient mechanical support is provided and the shotcrete prevents falling of pieces of rock. The curing and hardening conditions of this concrete lining is in situ and therefore controlled by the exchange of

dissolved species in the host rock pore water and the cementitious fluid as well as the ventilation rate in the disposal facility.

All linings limit or prevent the extension of the excavated damaged zone in the host rock by providing mechanical support to the host rock as well as providing stability during the operational period. The self-healing of cracks in the host rock by precipitation of minerals within the cracks or self-sealing of cracks in the host rock by swelling of clay minerals can start in the operational phase when there is sufficient access of water. These cracks can initially have a size of several metres. Seal-healing by precipitation of minerals within the cracks is characteristic for indurated clays and crystalline rocks. Swelling clay minerals such as montmorillonite (a smectite) can be altered into non-swelling secondary minerals by alkaline water (Deissmann, et al. 2021) and alkaline pore water is present in fresh concrete. The majority of clay minerals are (Neeft et al. 2019):

- Swelling clay minerals in poorly indurated clays considered as host rocks for example in Belgium and the Netherlands;
- Non-swelling clay minerals such as illite in indurated clays considered as host rocks for example in France and Switzerland.

Consequently, this potential interaction between concrete pore water and clay has mainly an impact on the seal-sealing of cracks in poorly indurated clays. This potential interaction is however negligible since the pre-fabricated concrete segments to construct the lining have a very small permeability, a much smaller permeability than the poorly indurated clay host rock. The permeability of the lining is also smaller than the permeability of the crystalline rock. Consequently, the concrete lining acts as a barrier for further transport of water into the facility. This water transport barrier function provides sufficient access of water to seal or heal the cracks in the operational phase. But also, the ingress of dissolved species from the host rock pore water that can alter the cement mineralogy of the lining starts in the operational phase for facilities constructed in crystalline rocks and poorly indurated clay.

The lining for a facility built in indurated clay decreases further drying by ventilation and the associated formation of drying shrinkage cracks of this clay host rock is limited. After the concrete of the lining has been hardened in the case of a lining made with in-situ curing, the clay may be too dry for dissolved species in the clay pore water to enter the lining in the operational phase.

The design life of the operational phase is envisaged to last at least 100 years. Figure 1-1 shows an artist impression of possible disposal cells in the operational phase. Only the facility constructed in the crystalline rock is shown here to have reinforced concrete i.e. caisson in Figure 1-1. All linings are drawn here without reinforcement but reinforced concrete may be used for linings. The artist impression for the crystalline rock has been extracted from the Swedish programme (SKB 2015), the one for poorly indurated clay is described in Chapter 6 and the one for indurated clay in Chapter 9 which is from the Swiss programme (Leupin et al. 2016).

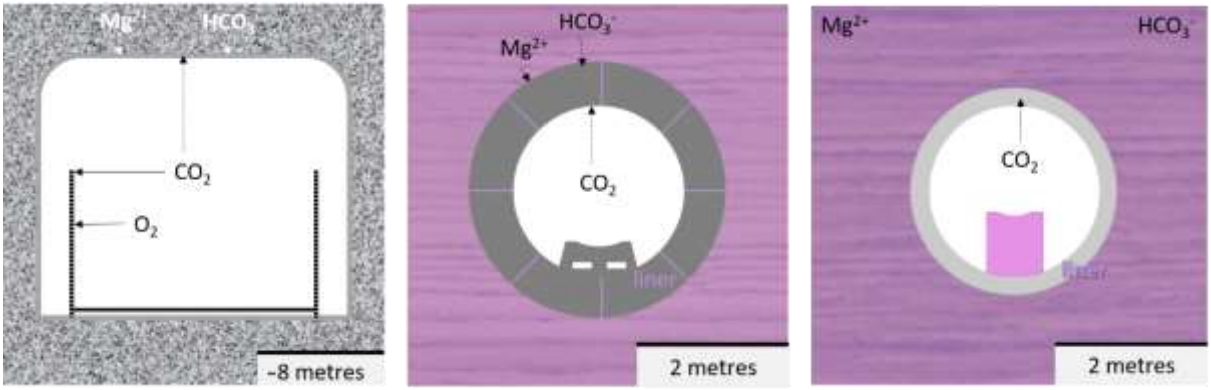

Figure 1-1: Disposal cells in the operational phase before emplacement of a waste package, ingress of species are indicated with an arrow, solid ones are considered to be detrimental for the mechanical strength of (reinforced) concrete. Host rocks: crystalline rock, poorly indurated clay and indurated clay.

Gaseous carbonation of concrete has so far been specified to be detrimental to the reinforcement within concrete. Carbonation of concrete by ingress of gaseous CO_2 from the ventilation of the air in the disposal facility takes place for all linings. The rate of ingress of this CO_2 into the concrete is determined by the water content within the lining. At the intrados of the lining, this water content depends on the temperature and on the relative humidity within the disposal facility. This water content is higher at lower temperatures and higher relative humidity's. The rate of ingress of CO_2 is smaller when the water content is higher. At the extrados of the lining, the ingress of host rock pore water and its dissolved species depends on the difference in permeability between the host rock and lining and how drying by ventilation has limited the potential diffusional paths of dissolved species in the concrete of the lining.

The concentration of dissolved bicarbonate in the host rock pore water can be hundreds of times larger than the concentration of gaseous CO_2 but the rate of ingress of dissolved bicarbonate can be multiple times slower than gaseous CO_2. Carbonation of concrete is envisaged to take place from the intrados and whether it also occurs at the extrados of the lining in the operational phase depends on the difference in water permeability between the host rock and lining.

For reinforced concrete, there can be spallation of concrete at the intrados due to the corrosion of steel when the concrete coverage has been too small manufactured. The manufactured strength of concrete cannot accommodate the local stresses induced by the increasing volume of corrosion products at the steel rebar. The strength of concrete itself may however not have been reduced when spallation occurs. Detrimental to the strength of concrete may be limited to ingress of dissolved magnesium if the cement to manufacture concrete has been carefully selected. The continuous mechanical loading by the host rock pressure on the lining can make the progressive reduction in strength of concrete more severe if the rate of ingress of species that are detrimental to concrete or reinforced concrete is increased by this mechanical loading.

1.3 Preparation of the post-closure phase

Cementitious materials can be used for three different purposes to be prepared for the post-closure phase:

1. As a backfilling;
2. In the waste package for disposal;
3. As a plug.

Backfilling of the volume left empty after emplacement of the waste packages is envisaged by most countries. This backfill can also be a cementitious material with a specified mechanical strength in concrete to contribute to the mechanical support. Its required strength can be smaller than the required strength of concrete for the lining.

The waste packages can also have cementitious material as engineered barriers in the disposal system. This barrier can be a:

- Waste form or a waste matrix to contain the radionuclides in the waste in the post-closure phase;
- Chemical buffer to provide the beneficial conditions to limit corrosion of a steel overpack surrounding the waste form. Hereto, any contact between the waste form of HLW and pore water is prevented, especially in the period of the post-closure phase when the waste emits heat. There is mechanical stress associated with the thermal gradient inside the buffer.

The technique to close the disposal galleries is a combination of a concrete plug and bentonite seal in many countries. The plug is mechanically radially loaded by the host rock pressure as well as axially loaded by the swelling pressure of bentonite.

1.4 References

Atabek, R., A. Beziat, H. Coulon, M. Dardaine, P. Debrabant, A. Eglem, C. Farcy, N. Fontan, C. Gatabin, P. Gegout, A. Lajudie, O. Landoas, J. Lechelle, F. Plas, D. Proust, J. Raynal, and E. Revertegat. 1991. Nearfield behaviour of clay barriers and their interaction with concrete - Task 3 Characterization of radioactive waste forms A series of final reports (1985-89 No 26 (Nuclear Science and Technology EUR 13877).

Atkins, M., N. Beckley, S. Carson, J. Cowie, F.P. Glasser, A. Kindness, D. Macphee, C. Pointer, A. Rahman, J.G. Jappy, P.A. Evans, G. McHugh, N.J. Natingley, and C. Wilding. 1991. Medium-active waste form characterization: the performance of cementbased systems Task 3 Characterization of radioactive waste forms A series of final reports (1985-1989) No 1 (Nuclear Science and technology EUR 13452).

Deissmann, G., N. Ait Mouheb, C. Martin, M.J. Turrero, E. Torres, B. Kursten, E. Weetjens, D. Jacques, J. Cuevas, J. Samper, L. Montenegro, M. Leivo, M. Somervuori, and L. Carpen. 2021. "Experiments and numerical model studies on interfaces. Final version as of 12.05.2021 of deliverable D2.5 of the HORIZON 2020 project EURAD. EC Grant agreement no: 847593." www.ejp-eurad.eu.

Jackson, M.D., S.R. Mulcahy, H. Chen, Y. Li, Q. Li, P. Cappelletti, and H.-R. Wenk. 2017. 'Philipsite and Al-tobermite mineral cements produced through low-temperature water-rock reactions in Roman marine concrete', American Mineralogist, 102: 1435-50.

Leupin, O.X., P. Smith, P. Marschall, L. Johnson, D. Savage, V. Cloet, J. Schneider, and R. Senger. 2016. "High-level waste repository-induced effects." NAGRA Technical Report www.nagra.ch.

Neeft, E., E. Weetjens, A. Vokal, M. Leivo, B. Cochepin, C. Martin, I. Munier, G. Deissmann, V. Montoya, P. Poskas, D. Grigaliuniene, A. Narkuniene, E. García, J. Samper, L. Montenegro, and A. Mon. 2019. "Treatment of chemical evolution in National Programmes. D 2.4 of the HORIZON 2020 project EURAD. EC Grant agreement no: 847593." www.ejp-eurad.eu.

SKB. 2015. "Safety analysis for SFR Long-term safety Main report for the safety assessment SR-PSU." SKB TR 14-01 available at www.skb.se.

2. Characteristics of samples studied in MAGIC

2.1 Rationale of sample size

All cementitious materials used in the construction and closure of the disposal facility are made with aggregates. These aggregates take about 75 vol% of concrete. Usually two types of aggregates are used to manufacture concrete: a coarse type and a fine type. The finer type of aggregates is used to fill the empty volume within the stacking of the coarse aggregates. The strength of aggregates and the attachment of the aggregates with the hardened cementitious phase determine the strength of concrete. The preferred shape of the aggregates is corner-like for a well attachment between the aggregates and hardened cementitious phase. Gaps between rounded of aggregates and cementitious phase may arise due to shrinkage of the cementitious phase during hardening. Sample size is a key issue in the determination of the altered strength of hardened concrete by ingress of species. The sample size should at least be three and a half times the maximum aggregate size for testing hardened concrete according to the European standard 12390. In this European standard, the recommended edges of cubical samples, smallest edge of prisms and diameters of cylinders in the measurement of the compressive strength are in mm: 100, 150, 200, 250 and 300. The height of cylinders should be twice as large as the diameter. The largest edge of a prism should at least be 3.5 times larger than the smallest edge. These sizes have been determined with a maximum in aggregate size of 32 mm which is common for ordinary civil engineering. Table 2-1 shows that the size of the aggregates of the samples studied within MAGIC is smaller than 32 mm.

Table 2-1: Size of aggregates, sample size and specification of loading

Origin	Aggregates				Sample size for measurement in strength	Comment
	Type		Content [kg m^{-3}]	Range in size [mm]		
Belgian samples	Quartzite gravel	Coarse	1252	4 to 15	To be determined	Cored from liner in Underground Research Laboratory (URL)
	Sand	Fine	540	-		
Czech samples	Quartz	Coarse	413	4 to 8	To be determined	Cast in cubical samples with an edge of 150 mm
	Sand	Fine	895	0 to 4		
Dutch samples	Quartz gravel	Coarse	866	2 to 8	Edge of cubical samples is 150 mm, 100 mm and 50 mm	Cast in samples. Also cubical samples with an edge of 50 mm have been sawn from cubical samples with an edge of 150 mm
	Sand	Fine	827	0 to 4		
	Sand	Fine	1131	0 to 2		Three types other mortars with no coarse aggregates
			1018			
			955			
French samples	Limestone gravel	Coarse	945	5 to 12.5	Diameter of cylindrical samples is 37 mm Smallest edge of prisms is 70 mm	Sample sizes for the lower strength concrete i.e. C40/50 Sample with higher strength class C60/75 will be taken from URL.
	Limestone sand	Fine	858	0 to 4		
German samples	Sand gravel	Coarse	793	2 to 8	Diameter of cylindrical samples is 50 mm	
	Sand	Fine	793	0 to 2		
Swiss samples	Rounded river sediment	Coarse and fine	1800	0 to 8	Diameter of cylindrical samples is 40 mm	Samples are cored from concrete cast in 120 litre barrels
			1704	0 to 16		
			1904	0 to 16		
	Sand	Fine	728	0.1 to 0.3	Diameter of cylindrical samples is 28 mm	Samples are cored from mortar cast in 60 litre barrels
		Fine	573	0.1 to 0.3		

Table 2-1 clearly shows that, if known, the sample size to measure the strength of concrete in MAGIC is almost always smaller than 100 mm. The smaller size does not necessarily has to result in erroneous measurements if the machine with which the strength is destructively measured is calibrated with this smaller size of sample and the envisaged ranges in strength of concrete. Also, the sample size

frequently remains larger than 3.5 times the maximum size in aggregates. Manufacturing of reinforced concrete may also need aggregates with a smaller range in size in order to achieve a uniform coverage of the steel bars by concrete.

Only samples being mechanically loaded till the host rock pressure and exposed to an environment in which ingress of species into (reinforced) concrete can provide the experimental result of the chemo-mechanical evolution of concrete representative for disposal. However, most experiments use samples being exposed to an environment in which ingress of species takes place without mechanical loading. The strength is measured after several periods of chemical and microbiological exposure of the concrete. These experiments are aimed to elucidate the microbial impact on the chemo-mechanical behaviour of concrete.

The chemo-mechanical evolution of the lining can be determined by sequentially measuring the strength of concrete from cores drilled from a lining and additional characterisations. The size and number of cores that can be taken from a lining in underground research laboratories and disposal facilities is limited to preserve the construction. It is therefore recommended to make many witness samples of the same (reinforced) concrete used for the lining in order to have sufficient samples that can be used to obtain a first indication of the alteration of the concrete strength after different decades in the operational phase. Whether a continuous loading representative of the host rock to concrete is necessary for the prediction of the chemo-mechanical evolution of concrete is yet unknown.

2.2 Type of cement

Any combination of aggregates and type of cement is determined by the exposure environment. As explained in Chapter 1, the deterioration of concrete too early in the operational and post-closure phase by ASR and DEF can be prevented. Table 2-2 shows the combinations of aggregates and cement of the samples investigated in MAGIC.

Table 2-2: Combination of aggregates and cement

Kind of samples	Type of aggregates	Cements	CEM I [wt%]	CEM III/B [wt%]	Clinker [wt%]	BFS[a] [wt%]	silica[b] [wt%]	Fly ash [wt%]	Filler [wt%]
Belgian samples	Quartz gravel and sand	Blend	62				17	21	
Czech samples	Coarse Quartz and sand	Blend	40			9	51		
Dutch samples	Quartz gravel and sand	CEM III/B			20-34	66-80			0-5
	Sand	CEM III/B			20-34	66-80			0-5
	Sand	CEM I			95-100				
	Sand	CEM III/B			20-34	66-80			
French samples	Limestone gravel and limestone sand	CEM I			95-100				0-5
German samples	Sand gravel and sand	Blend	31				23		46
Swiss samples	Rounded river sediment	Blend	60				40		
		Blend		90			10		
		CEM I			95-100				0-5
	Sand	CEM I			95-100				0-5
	Sand	Blend	60				40		

[a] *Blast furnace slag,* [b]*Micro or nano silica or silica fume*

Table 2-2 shows that many samples have been fabricated with blended cements. Commercially available blends have a range in composition while the range in composition with own made blends is limited to 5 wt%. The use of pure CEM I (or OPC) requires a careful look to the risk of ASR for experiments in which sufficient moisture can be present within the sample. ASR can be eliminated by manufacturing concrete with non-siliceous aggregates such a limestone. Another elimination is the use of quartz aggregates but the manufactured concrete with CEM I may then not be irradiated since irradiation can alter the crystal structure of silica by which it can become a reactive aggregate. From the provided available information, it is not clear whether the sand as aggregates are actually quartz aggregates. Also, samples with solutions may need to be sterilized with radiation in order to investigate the impact of microbial activity.

DEF made by an internal sulphate attack has a too low strength at the start of an experiment. For well-cured and hardened concrete with sufficient strength, DEF by an external sulphate attack can occur by ingress of sulphate species. Commercially available cements have indicated that with Sulphate Resistance (SR) and for CEM I also with different SR degrees. This detail in sulphate resistance has frequently not been provided in the descriptions (see Chapter 4 to 9). Consequently, an overview of DEF cannot be given.

2.3 Limitation of water content in concrete recipe

The water to cement ratio should be as small as possible for the durability of concrete as explained in Chapter 1. Frequently, aggregates with a size smaller than 32 mm have been used or will be used to manufacture the concrete studied in MAGIC as shown in Table 2-1. The disadvantage of the use of finer aggregates is that the concrete recipe requires a higher water content in order to achieve a well mixing of the ingredients and processability of the cementitious fluid. A higher water content is associated with the formation of a rougher pore structure in the cementitious phase by which the rate of ingress of detrimental species is larger. Superplasticisers are used to achieve a well mixing and processability of cementitious fluid with a reduced water content. Table 2-3 shows the water to cement ratio of the samples that are studied within MAGIC; only porosities determined by the evaporation of water from initially saturated samples have been included. For simplicity, any additions to cement such as silica fume, microsilica or nanosilica, fly ash or blast furnace slag and filler are also considered to be part of cement.

Table 2-3: Water to cement ratio and porosity of the samples studied in MAGIC

Origin	Range in size of aggregates [mm]	Aggregate [kg m^{-3}]	Water [kg m^{-3}]	Cement incl. add. [kg m^{-3}]	Water / Cement incl. add.	Superplasticiser used? yes / no	Porosity determined by evaporation
Belgian samples	4 to 15	1252	135	540	0.25	yes	11%
	-	540					
Czech samples	4 to 8	413	200	351	0.57	yes	MAGIC
	0 to 4	895					
Dutch samples	2 to 8	866	184	402	0.46	yes	13%
	0 to 4	827					
	0 to 2	1131	144	411	0.35	yes	21%
	0 to 2	1018	165	417	0.40	no	-
	0 to 2	955	154	391	0.39	no	-
French samples	5 to 12.5	945	171	400	0.43	yes	13%
	0 to 4	858					
German samples	2 to 8	793	160	520	0.31	no	MAGIC
	0 to 2	793					
Swiss samples	0 to 8	1800	175	350	0.50	yes	local porosity
	0 to 16	1704	247	228.9	1.08	yes	local porosity
	0 to 16	1904	190	238	0.80	no	local porosity
	0.1 to 0.3	728	423	899	0.47	no	MAGIC
	0.1 to 0.3	573	411	827	0.50	no	MAGIC

Most water to cement ratios are smaller than 0.50 for the samples studied with MAGIC. The water to cement ratio may however be underestimated in Table 2-3 since the additions can have their own water content for example silica fume is a slurry with 50 wt% silica and 50 wt% water. Information about the porosity is available for about half of the samples at the start of MAGIC. The porosity will become available at the end of MAGIC for all samples.

Usually samples with the largest content of aggregates and size of aggregates have the smallest porosity for well-mixed and hardened concrete. Aggregates are usually so dense that their porosity is virtually zero and the porosity is then only determined by the cementitious phase within concrete and the attachment between this phase and aggregates.

The variation in porosity between the samples can be large if the ingredients are not well mixed. This variation has a large impact on the interpretation of the measured mechanical strength. For example, is the decrease in strength caused by the chemical alteration or did the sample have a smaller strength due to its higher porosity than other samples at the start of the chemical and microbiological exposure?

3. Age, exposure and available strengths of concrete samples

The strength class of a cementitious material is determined before any further specification and depends on the function. The required strength class for a lining is usually higher than the required strength for a buffer especially if unreinforced concrete is used. The strength is given for a characteristic cylindrical and cubical compressive strength for example C 35/45. Concrete recipes are mechanically tested after 28 days hardening and the average of the measured cylindrical or cubical compressive strengths should at least be larger than 35 MPa for cylindrical samples with a diameter of 150 mm or 45 MPa for cubical samples with an edge of 150 mm. The loading rate should be between 0.6 MPa/s ± 0.2 MPa/s according to the European standard 12390. The compressive strength is destructively measured with this standard. Table 3-1 shows that not all samples have achieved the required strength class; if a strength class has been assigned and if the measurement of the compressive strength is available.

Table 3-1: Measurements of compressive strength and strength class

Kind of samples	Strength class	Cements	Age [days]	N	Compressive strength [MPa]	Comment
Belgian samples	C80/95	Blend with CEM I				A compressive strength of 88 MPa was required
Czech samples	-	Blend with CEM I	28	-	47.6	Cubical samples with an edge of 150 mm. Also measured Young's modulus available.
Dutch samples	C35/45	CEM III/B	28	3	53.2 ± 1.3	Cubical samples with an edge of 150 mm
	C?/10[a]	CEM III/B	28	3	19.6 ± 1.7	
	C?/10[b]	CEM I	28	6	11.5 ± 3.7	
	C?/10[c]	CEM III/B	28	6	8.0 ± 0.8	
French samples	C60/75	CEM I	28		62.5 ± 2.5	Also measured Young's modulus, tensile strength and Poisson's ratio available.
	C40/50	CEM I	28		MAGIC	
German samples	-	Blend with CEM I	28		58	Also measured Young's modulus available.
Swiss samples	-	Blend with CEM I	90		79.2	Compressive strength after 28 days was not available. Young's modulus becomes available in MAGIC.
		Blend with CEM III/B	90		33.7	
		CEM I	90		29.7	
	-	CEM I	-			Young's modulus becomes available in MAGIC.
	-	Blend with CEM I	-			

N is number of samples, C?/10 means that the characteristic cylindrical compressive strength has not been defined yet.

The hardening of concrete still continues after 28 days and there are also measurements of the compressive strength available with more than 28 days hardening:

- Czech samples: 50.8 MPa, 52.3 MPa and 53.5 MPa for 60, 90 and 174 days, respectively;
- Dutch samples: 58.1±4.3 for C35/45 after 5 months and 15.1±2.0 for C?/10[a] after 4 months. These samples have been derived by sawing a larger cubical sample. Sawn samples appeared to have a smaller strength than only casted samples if the chemical exposure period was larger. After 3 years, the only casted samples had an average cubical compressive strength of:
  - 75.6±5.0 MPa (20°C, submerged in distilled water), 76.0±1.7 MPa (20°C, 98%) and 74.4±1.3 MPa (5°C, submerged in distilled water) for C35/45;
  - 27.2±1.1 MPa (20°C, submerged in distilled water), 29.5±1.1 MPa (20°C, 98%) and 25.1±0.9 MPa (5°C, submerged in distilled water) for C?/10[a];

  While the casted and samples sawn from larger cubical samples had a smaller compressive strength and a larger variation in strength after 3 years i.e. an average cubical strength of:
  - 52.1±7.7 MPa (5°C, 99%) for C35/45;
  - 18.7±6.0 MPa (5°C, 99%) for C?/10[a].
- French samples: 65 ± 2 MPa for C60/75 after 3 months.

The provided information about other mechanical characteristics of the studied types of concrete such as Young's modulus, tensile strength and Poisson's ratio is too small for this overviewing Chapter. The interested reader can find these properties in the contributions in Chapter 4 to 9.

Table 3-2 shows that there are two types of samples from URLs. These samples have been exposed to clay as well as air. Air has a content of CO_2 of 0.04% and gaseous carbonation of concrete occurs in the operational phase.

Table 3-2: Years of exposure of samples at start of MAGIC

Kind of samples	Strength class	Cements	Chemical exposure	Years of exposure
Belgian samples	C80/95	Blend with CEM I	Belgian Boom clay & ventilation air in URL*	13 and 18 years
Czech samples	-	Blend with CEM I	Air humidity of 95±5% and 15±2°C	2 years; samples to be exposed to air, bentonite and underground (Bukov) crystalline water in MAGIC
Dutch samples	C35/45	CEM III/B	Air at different relative humidity's at 20°C and 5°C	3 years (finished)
			Dutch Boom clay pore water at about 20°C	5 years
	C?/10[a]	CEM III/B	Air at different relative humidity's at 20°C and 5°C	3 years (finished)
			Dutch Boom clay pore water at about 20°C	5 years
	C?/10[b]	CEM I		
	C?/10[c]	CEM III/B		
French samples	C60/75	CEM I	French Oxfordian clay & ventilation air in URL* (air is 20°C and about 65% relative humidity)	Reifnforced concrete slab and shaft up to 17 years old.
	C40/50	CEM I	3% CO_2 at 50°C at a relative humidity that maximises carbonation. Also underground clay pore water representative for Bure.	To be started in MAGIC for reinforced concrete.
German samples	-	Blend with CEM I	Exposure to one side of concrete with underground saline (Konrad) solution	Percolation experiment to be started in MAGIC
Swiss samples	-	Blend with CEM I	Opalinus clay	14 years
		Blend with CEM III/B		
		CEM I		
	-	CEM I		9 years
	-	Blend with CEM I		

*Concrete samples from these experiments have also been mechanically loaded till host rock pressures.

Gaseous carbonation has been known to be dependent on the temperature and on the relative humidity of air to which concrete is exposed. The equilibrium water content within concrete as a function of the relative humidity in air and temperature has been characterised for the Dutch samples. The Genuchten parameter α needed to be made temperature dependent in order to obtain a good fit with the measurements i.e. a larger value at a higher temperature. Consequently, the equilibrium water content as a function of the relative humidity is lower at a higher temperature. Carbonation rims by gaseous carbonation in air appeared to be very small for the Dutch samples after three years of exposure to air at different relative humidity's at 5°C and 20°C. It was preliminarily assumed that carbonation had no impact on the concrete strength. The smaller equilibrium water content in pores was considered the primary cause of the higher measured compressive strength at lower relative humidity's. This cause has been validated for C35/45 concrete for only cast-in samples.

To air exposed samples that had been made by sawing from cast-in larger samples have smaller compressive strengths. It was concluded that sample preparation such as sawing can have an impact on the measured compressive strength. The relation with additional strength and suction force of pores

as found for samples with a strength class C35/45 could not be found for samples manufactured with the lower strength class C?/10[a]. This difference is tentatively attributed to the reliability in the measurement of the porosity by the evaporation of water. The porosity measured by evaporation of water was for the samples with a strength class C35/45 also equal to the total porosity while this similarity may not the case for these samples designed with a lower strength.

Carbonation by ingress of dissolved bicarbonate species takes place for all samples exposed to solutions but it may not have a detrimental effect on the mechanical strength of concrete but rather a detrimental effect to the reinforcement within concrete.

The ingress of dissolved magnesium does have an impact on the strength of concrete but this ingress may be negligible for the samples exposed to Belgian Boom Clay or Bukov underground water with the available knowledge since the pore waters are both fresh water types i.e. the dissolved magnesium content is below 300 mg/l in Table 1-1 (Neeft et al. 2019). Please note that these ranges in Table 1-1 have been determined for civil engineering with operational lifetime of structures lasting about one hundred years. On longer terms i.e. in the post-closure phase, an impact of the ingress of magnesium at the lowest concentration cannot yet be excluded. The magnesium content of the solutions in the Dutch and German programme is within the range of XA2 of Table 1-1 and the clay pore solutions in the French and Swiss programme in the range of XA1 of Table 1-1. Indurated clays are considered in the French and Swiss programme and the values of permeability within the clay can be smaller than hardened concrete by which the ingress of dissolved magnesium may not take place during the operational phase as explained in paragraph 1.2.

4. Belgian samples

Authors: Quoc Tri Phung, Janez Perko, Suresh, Seetharam, Kristel Mijnendonckx and Xianling Li (SCK CEN)

4.1 Mechanical safety function and performance target

In the Belgian concept of geological disposal of radioactive waste in a clay host rock (Figure 4-1), concrete tunnel liners play a crucial role in ensuring safety during and after (retrievability) the operational phase of the disposal system. Thus the expectation is that the liners offer mechanical stability at least for several hundreds of years. However, the fact that concrete is not in geochemical equilibrium with the surrounding geological environment resulting in a gradual evolution of its physical, chemical and mechanical properties, which may not be desirable from safety point of view. Furthermore, the above, that is, chemically induced degradation of concrete structures are equally applicable for near-surface disposal facilities, where concrete is the primary material of construction. Thus the study of long term chemo-mechanical behavior of concrete is an important undertaking and in the long term will offer extremely valuable input to the safety case for the Belgian geological disposal program. In fact, a single study will not suffice to reach a thorough understanding of all aspects of the coupling and hence there is a strong need to initiate research in multiscale experimental and numerical chemo-mechanics at this stage of the R&D program for waste disposal.

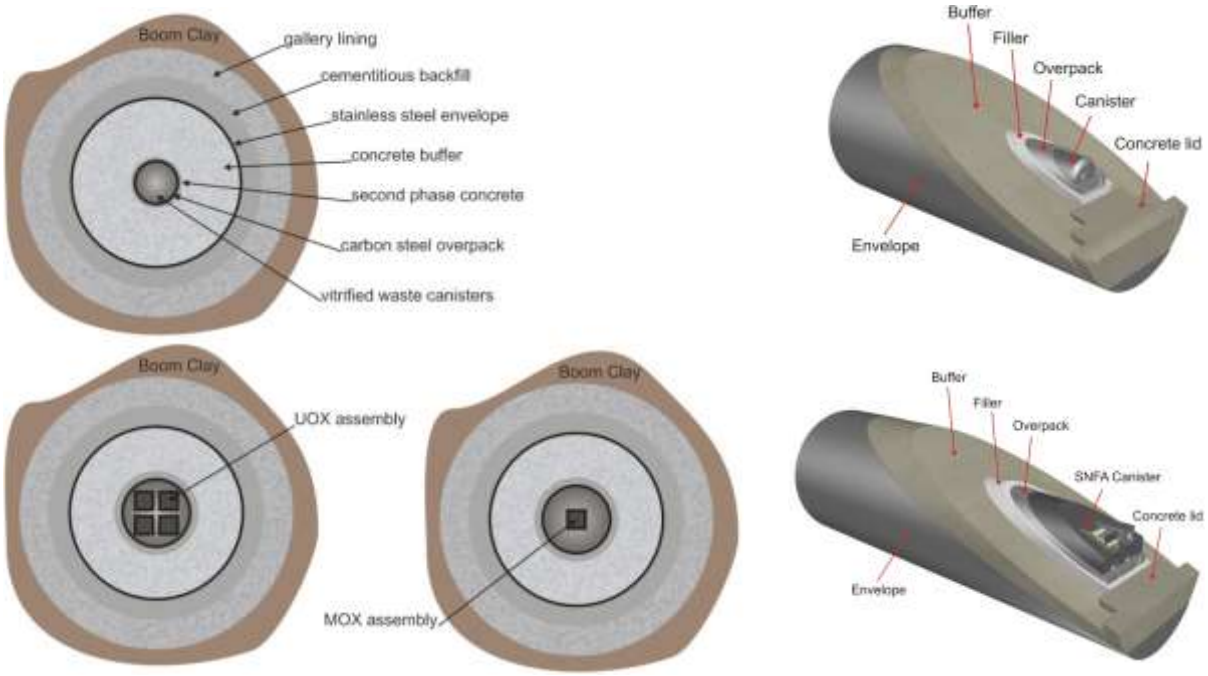

Figure 4-1: Concrete used for disposal gallery lining, buffer, and backfill in high level waste facility – Belgian Supercontainer concept

4.2 Size of samples, concrete recipe

The tests are performed on high strength concretes (wedge blocks) used as lining material in the Connecting Gallery of HADES URL. Age of interface concrete - Boom Clay host rock is about 13 years. The composition of concrete is shown in Table 1. The coarse aggrage was crushed quartzite gravel with grading 5-14 mm. The fine aggregate was quartzsize grit sand.

Table 4-1: Mix compositions of in-situ concrete: SP – Superplasticizer

For 1 m^3 concrete	Cement kg	Fly ash kg	Coarse agg. kg	Fine agg. kg	Admixture		Water l
					SP l	µ-silica kg	
Connecting gallery	335 (CEM I)	115	1252	540	4.5	90	135

4.3 Available characterisation of cementitious material

4.3.1 Mechanics

4.3.1.1 Compressive strength

The concrete was not reinforced and had to belong to the C80/95 class, according to the Eurocode 2. It had to have a compressive strength of 88 MPa (Chen et al., 2021).

4.3.1.2 Young's modulus

The mechanical behaviour of the concrete lining is assumed linearly elastic. The elasticity modulus of the concrete is calculated based on its mean compressive cylinder strength, and equal to 42 GPa.

4.3.1.3 Microstructure

Measurement of Water-Accessible Porosity

The volume of water-accessible pore space of the samples was calculated from the oven dry mass (m_o) after drying at 110 °C for 24 h, the water-saturated mass after immersion for 48 h and boiling for 5 h (m_{sat}) and the immersed apparent mass after suspending the sample on a wire in water (m_{app}). The following equation was used:

$$Water\ porosity\ (\%) = \frac{m_{sat} - m_o}{m_{sat} - m_{app}}\ x\ 100$$

Mercury Intrusion Porosimetry (MIP)

Prior to the MIP analysis, the samples were crushed with a hammer and chisel and freeze dried. Mercury injection porosimetry was performed at KU Leuven, Belgium, using an AutoPore IV 9500 mercury porosimeter. Mercury was injected up to a pressure of 200 MPa, and the pressure versus the injected volume of mercury was recorded.

Mercury is a non-wetting fluid and will not spontaneously flow into the pores by capillary action. It will only enter a pore when the resisting force is overcome. For a pore with a certain diameter, a certain pressure has to be exerted to overcome this resisting force. This relation between pressure and pore diameter is described by the Washburn equation. By registering the pressure versus the intruded volume, and by applying the Washburn equation, the pore size distribution can be calculated.

N_2 adsorption Measurements: Specific Surface Area and Pore Size Distribution

The specific surface area was measured by nitrogen adsorption at 77 K in a Gemini Surface Area Analyser (Micromeritics), using the Brunauer–Emmett–Teller theory. Prior to the measurement, a sample mass of around 3 g was degassed at 110 °C. Next, the pressure of N_2 was gradually increased, and the amount of adsorbed gas was measured as a function of the relative pressure, which allows for plotting the adsorption isotherm.

Pore size distributions have been determined, using both the Barrett, Joyner and Halenda (BJH) and the Dubinnin–Astakov theories, which allows a reliable determination of the pore size distribution from 1.5 nm up to 250 nm.

Analysis of the Microstructure and Porosity by SEM Imaging

Cubic samples of 1 cm^3 were sawed and subsequently embedded in an Epofix resin. The embedded samples were then polished with the Struers Tegramin-30 device in a step-by-step process in which the grit of the polishing plate was reduced to 1 µm. Diamond paste was used for lubricating the samples during polishing. The polished samples were imaged with a Phenom Tabletop scanning electron microscope at a magnification of 500× and a voltage of 15 kV.

Obtaining a Pore Size Distribution from the Combination of MIP, N_2-Adsorption and SEM Imaging

The SEM images were segmented in the Fiji software suite based on their grey level histogram to distinguish the pores from the rest of the material. The area of the individual pores was determined and processed to obtain a pore size distribution for each image. Due to the limited resolution of SEM, the calculated pore size distributions are only a part of the true pore size distribution of the sample. Therefore, the smaller pore size information can be obtained from MIP and N_2-adsoprtion techniques. The gel pores (nm size) are difficultly measured by MIP for normal applied pressure range. N_2-adsorption is able to provide pore structure information in a smaller range compared to MIP technique. Therefore, we applied a method to combine these 3 techniques proposed in (Phung et al., 2017) in order to obtain a comprehensive picture on pore structures of how the concretes affect the diffusion properties.

Microstuctures of Lining Concretes

The microstructural properties of lining and supercontainer concretes measured by N_2-adsoption are shown in Table 4-2. One can clearly observe a dense microstructure for the lining concrete sample with a low cumulative pore volume of 8.12 mm^3/g. The amount of micropores (<2 nm) is very limited. Figure 4-2 (top) shows the cumulative pore volume and pore size distribution obtained from adsorption branch using BJH method of lining and supercontainer concretes obtained by N_2-adsoption measurements. Figure 3 (bottom) also shows the cumulative porosity and pore size distribution measured by MIP. The MIP pore size distribution shows that most of the pores of the lining concretes distribute in the range 30 to 90 nm. A small pore fraction at around 10 µm is also observed, which could be attributed to the air voids or micro cracks presented in concretes.

Table 4-2: Microstructural properties of lining concretes characterized by N_2-adsoprtion

Sample	SSA_{BET} (m^2/g)	$SSA_{t\text{-}plot}$ (m^2/g)	$SSA_{\mu pore}$ (m^2/g)	Cumulative Pore Volume (mm^3/g)	Cumulative Micropore Volume (mm^3/g)
Lining concrete	1.9	1.5	0.4	8.1	0.2

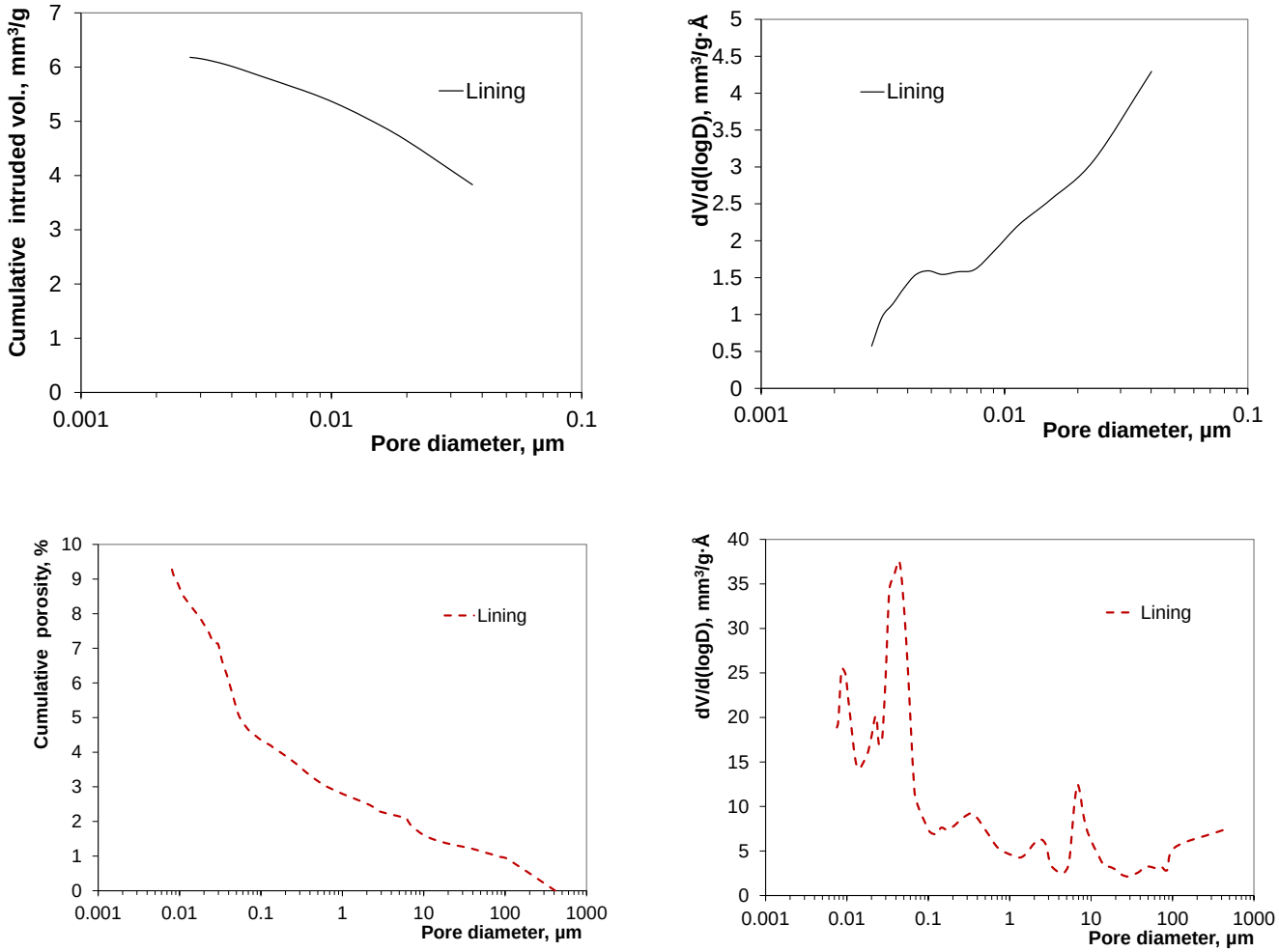

Figure 4-2: Cumulative pore volume and pore size distribution of lining concretes obtained by N_2-adsorption (top) and MIP (bottom).

In order to obtain more information at the micro scale, the SEM images were segmented and analyzed, as shown in Figure 4-3, with a SEM image of supercontainer concrete. The original SEM image was segmented to obtain a binary image containing pore and solid phases. The segmented image was then subjected to pore size measuring and counting in order to calculate the cumulative porosity and pore size distribution. Note that in order to obtain a representative manner, a set of around 10 SEM images was analyzed and the average microstructural properties were then calculated. As seen in Figure 4-3, most of the pores distribute around 10 µm, which is consistent with MIP measurement. However, the pore fraction in this case is much higher than the one determined by MIP.

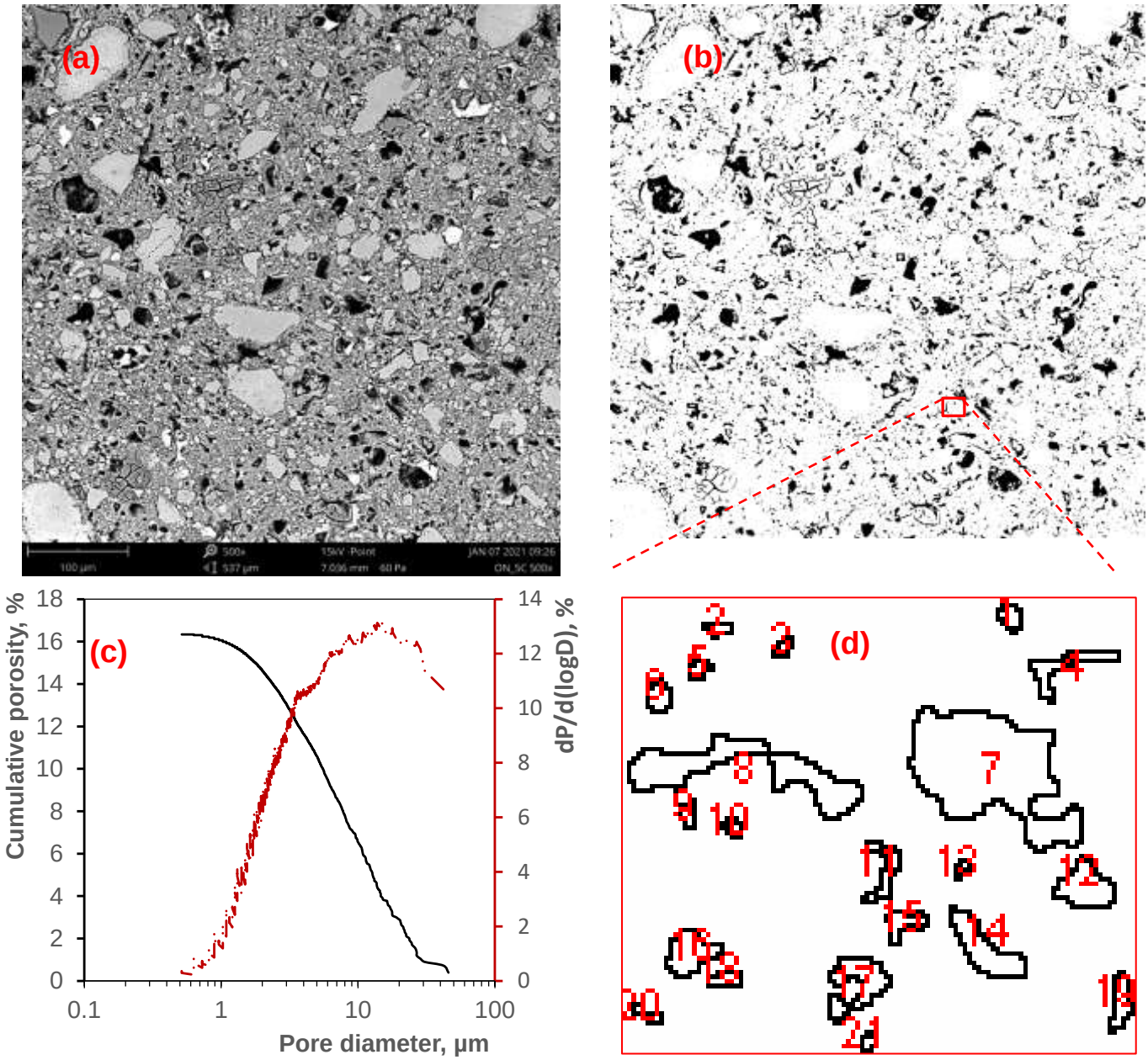

Figure 4-3: An example of SEM imaging analysis procedure to obtain the pore size distribution: (a) original SEM image, (b) binary segmented image (black = pore), (c) SEM cumulative porosity and pore size distribution and (d) an example of pore size measuring and counting, in which the different pores are numbered (1 to 21).

Applying a combination of MIP, N_2-adsorption and SEM measurements allows us to obtain a full range of pore size distribution from 2 nm to 50 µm, as shown in Figure 4-4. In this study, the pores with size in range 10 nm to 1 µm were characterized by MIP, while the smaller and larger pores were obtained by N2-adsorption and SEM, respectively. Note that the measurements were done on the specimens without coarse aggregates. Therefore, a normalization step (Jacops et al., 2021) is needed to estimate the pore size distribution of the samples with coarse aggregates by taking into account its volume fraction in the concretes. In this normalization step, we neglect the porosity of coarse aggregates and normalize by taking into account the volume fraction of the coarse aggregates which can be calculated from the mix composition. Figure 4-4 shows both pore size distribution for mortar (without coarse aggregate) and concrete levels. It can be seen that the coarse aggregates significantly contribute to the pore size

distribution and the cumulative porosity. The cumulative porosity is almost double for lining concretes if the coarse aggregate phase is not taken into account.

The cumulative porosity determined by combination of MIP, N_2-adsorption and SEM of lining (including aggregates) is 13% (Table 4-3). The measured water porosity also shows a consistant value of 11%. Though the water porosity is slightly lower than the cumulative porosity obtained by the combination of MIP, N_2-adsorption and SEM, it can still be considered that the accessible porosity estimated by these two methods are in line with each other as a slight difference could be within the uncertainty of measurements and combined (MIP, N_2-adsorption and SEM) approach.

Table 4-3: Summary of measured properties.

	Lining
Water porosity (%)	11
Cumulative porosity (%)	13

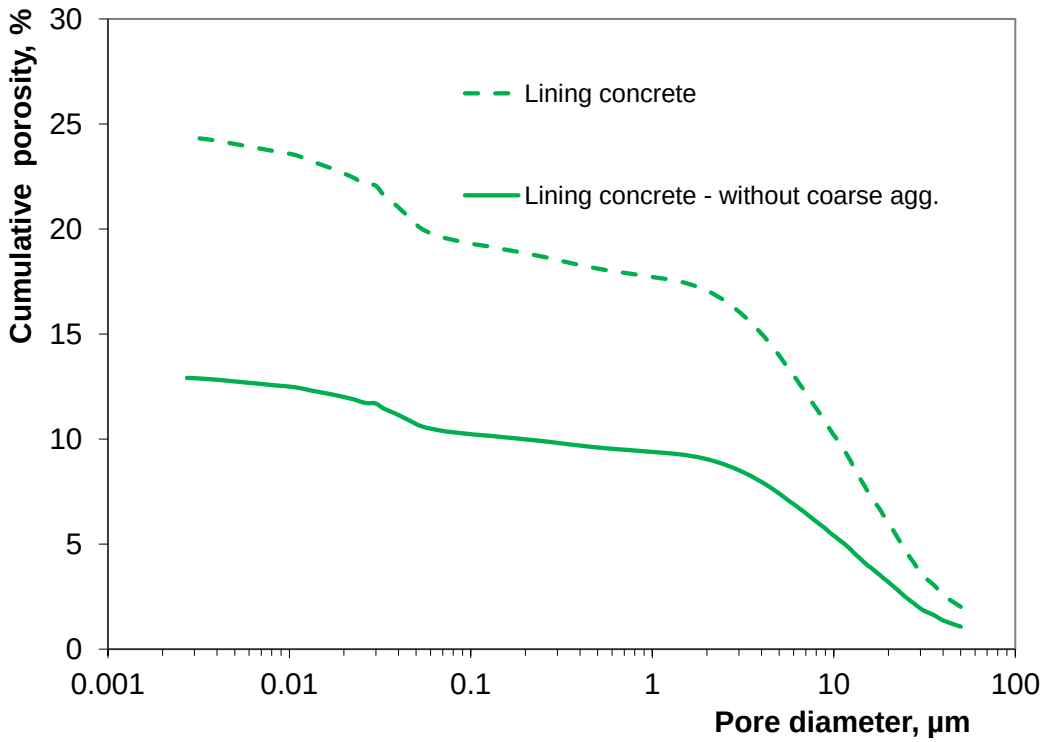

Figure 4-4: Pore size distribution for lining and supercontainer concrete, combined from N_2-asdsorption, MIP and SEM measurements.

4.3.2 Chemistry

4.3.2.1 Mineralogy

A multi-scale investigation methodology, based on clay materials, has been developed during the European FP7 CATCLAY project (Gaboreau, Robinet et al. 2016). The methodology integrates several bulk macroscopic characterization techniques and imaging methods to display quantitative data from macroscopic to nanoscopic scale. The association of several 2D/3D techniques (mineral cartography, autoradiography, X-ray µ-tomography, SEM, FIB-nT and TEM) allows reaching a quantitative and spatial distribution of the mineralogy and the pore network, from nanometer to micrometer represented by several geometric key parameters such as the pore size distribution and the associated mineral distributions. Detailed descriptions of mineralogical characterization can be found in previous work (Phung, Gaboreau et al. in press).

Two mineralogical maps were acquired in concrete: both in and outside of the interface region. These mineralogical maps calculated from the quantitative X-ray intensity maps of the major elements constituting the materials are shown in previous work (Phung, Gaboreau et al. in press). Figure 4-5 shows the ternary diagram of Si, Ca, and Al-Fe-Mg for concrete interface (orange) and bulk material (red). It is clear that the Ca/Si decreased, while the Al-Fe-Mg increased at the concrete interface. This gives an indication that Ca has been leached from the concrete interface because Si as well as Al, Fe, Mg concentration are quite stable. Further analysis to calculate the mass fraction of each phase, the chemical composition of each mineral and phase by integrating all the pixels constituting a phase are still on-going and will also be performed within MAGIC (see section 4.5.3).

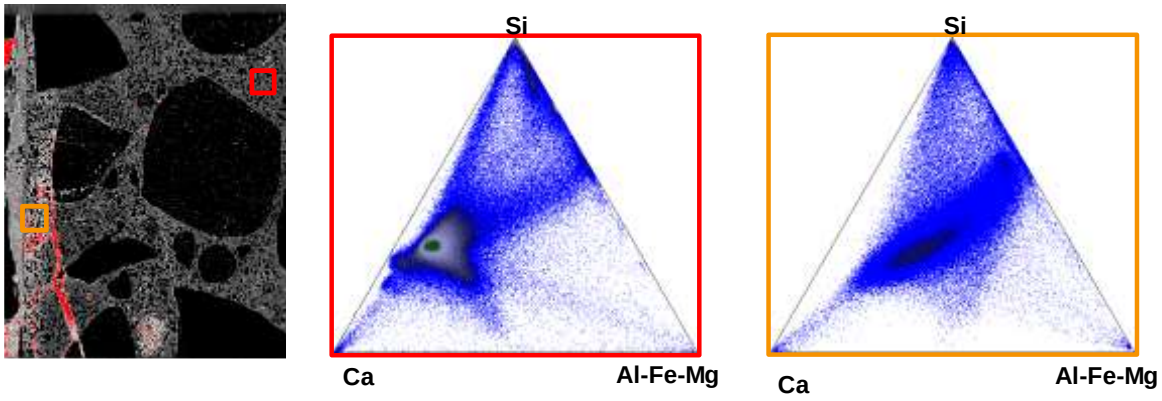

Figure 4-5: Chemical evolution of the concrete toward the interface – measured in 2 mm thickness from the interface

4.4 Description of experimental set-up

Within MAGIC, we aim at studying both existing interface and newly created interfaces. We perform experiment on both in-situ interface and newly made interface by acceleration in the laboratory. Boom Clay-concrete interfaces are sampled in the HADES underground research facility (Mol, Belgium). Samples are taken from the Connecting Gallery, in which low-permeability high-pH concrete wedge-blocks are in contact with Boom Clay for 18 years.

Details of drilling procedure are described below:

- We first drill a hole of 100 mm in diameter and 350 mm in depth in the concrete block (total thickness is 400 mm) cooling with water. This part is removed; the leftover is 50 mm of concrete at the outside of the lining, which is dried with compressed air. Note that we cannot drill the hole with the diameter larger than 100 mm to avoid reduction in mechanical strength of the gallery.
- In order to reinforce the concrete-clay interface and ensure that the interface remains intact as one piece during coring, we install two anchors (Figure 4-6 a & b) entering from concrete into the clay. Two holes of 18 mm in diameter are drilled through the 50 mm leftover concrete and entering 100 mm deep into the Boom Clay. The holes are drilled by dry drilling in order to avoid disturbing the contact between Boom Clay and concrete. A guiding system (Figure 4-6a) is used to keep the drilling bit parallel with the boreholes.
- Pouring the resin (Figure 4-6c) into the 18 mm diameter holes. Note that the holes are inclined (45o) to the horizontal direction with which allows the resin staying in the holes after pouring. The choice of an efficient resin is crucial to avoid leakage around the side of the sample. The resin should have low viscosity, good contact with clay and concrete, high strength, and low heat generation during polymerization. As suggested from previous study (Phung, 2015), Sika® Injection-451 was selected as the most optimal choice.
- After polymerization of the resin, we dry-drill with a 100 mm drilling bit (cooling with compressed air) through the 50 mm concrete leftover and into the Boom Clay for about 100 mm (Figure 4-6d).
- Finally, the concrete-clay interface sample is retrieved from drilling bit using a hydraulic press and kept in aluminium foil to prevent any drying and reaction with the air.

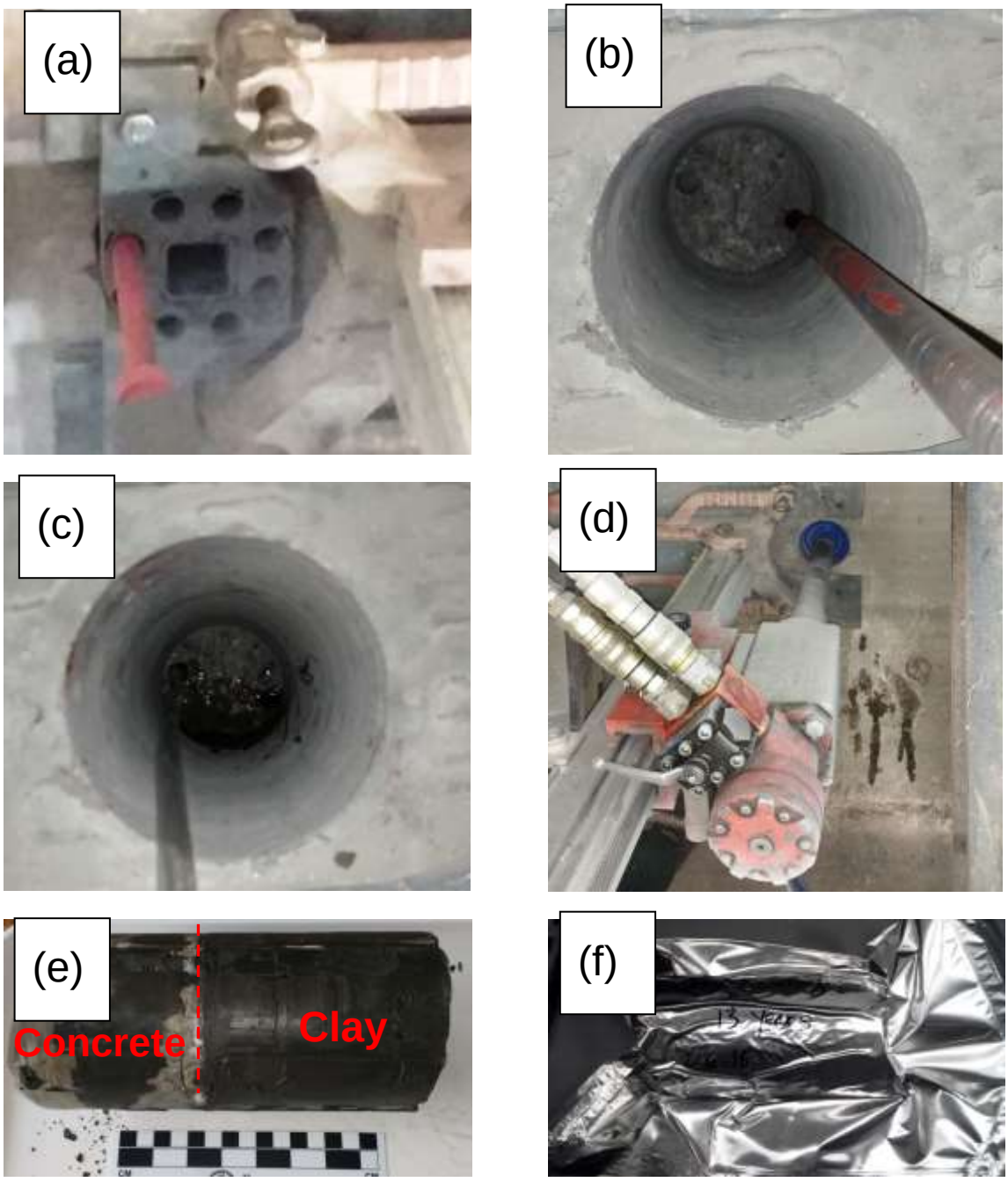

Figure 4-6: In-situ drilling procedure: (a) Drilling small hole using guiding system; (b) Two small holes for resin filling; (c) Resin filling into two small holes to make two anchors after polymerization; (d) Dry drilling concrete-clay interface after reinforcing by anchors; (e) Concrete-clay interface sample after retrieving from drilling bit; and (f) Sample packaged in aluminium foil.

For newly made concrete, we will perform both percolation and batch type's experiments.

Percolation tests:

In order to simulate the hydraulic pressure at the deep disposal, the Boom Clay solution with or without microorganisms will be percolated into a hardened mortars disc in a percolation cell by a syringe pump. We will simulate the partial CO_2 pressure at the HADES underground research facility (Mol, Belgium) by bubbling 0.4% CO_2 gas (in an argon background) into the clay pore water solution. The syringe pump also enables recording the flow rate and cumulative pore water injected into the system. A pressure

difference of 3-5 bar will be applied on the cell, which accelerates the interaction. A series of 3 experiments will be performed, which will be stopped as function of the interaction time (6, 12 and 18 months). For each interaction time, samples will be used for measuring the changes in transport properties (i.e. permeability, diffusivity, sorptivity) and changes in chemical and microstructural and mechanical properties due to combined carbonation and leaching under advective regime. Moreover, possible microbial biofilm formation on the surface of the cement will be investigated in detail. The outflow will also be sampled in closed bottles regularly to follow up the changes in chemical and biological compositions of the pore solution.

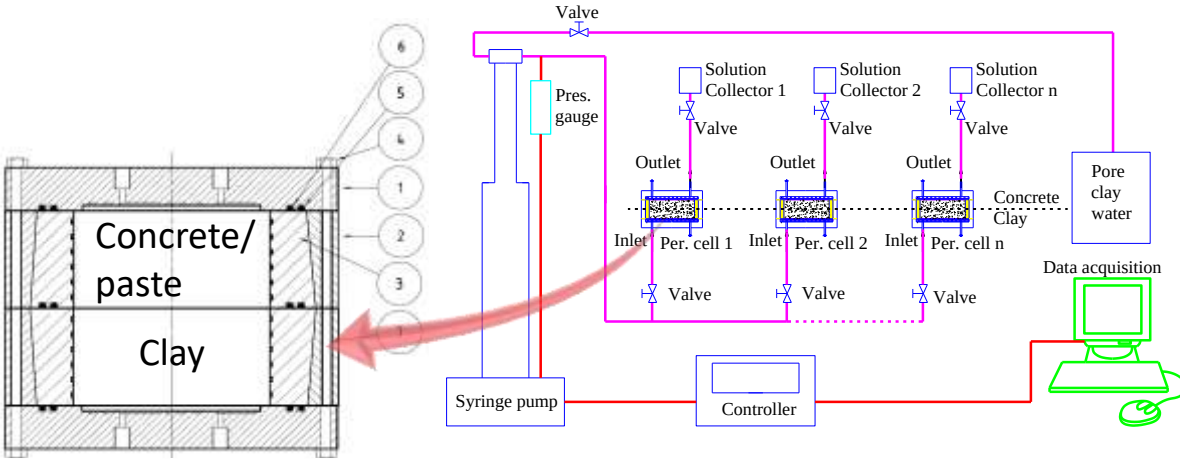

Figure 4-7: Schematic test setup for percolation experiment – the percolation cell (left) composes (1) steel lid, (2) steel body, (3) inner polycarbonate body, (4) bolt, (5) inner O-ring, (6) outer O-ring, and (7) threaded rod.

Batch test:

Batch type experiments will also performed in which a saturated mortars disc will be immersed into a Boom Clay slurry. Two cases are considered to assess the microbial effect to the degradation; the reference case without a presence of a microbial community and a case with microbial community. The absence of a microbial activity is to be achieved through sterilization. The experiments will be conducted in closed chambers, in which CO_2 will be bubbled to mimic the in-situ CO_2 concentration (0.4%). The chemical and biological compositions of the slurry will be followed regularly. The transport properties and microstructural, mechanical and biological evolution will be determined at the end of the experiments (6 and 12 months). These experiments are expected to induce more rapid cement degradation under diffusive regime due to the excess of water compared to in-situ conditions. Both leaching and carbonation are expected to be happen under such experimental setup. 2 types of sample sizes will be prepared: the large discs with 78mm in diameter and 45mm in thickness (for transport properties measurements) and small cylinder with 5mm diameter and 10mm thickness for microscopic uniaxial compression creep tests with micro-tomographic imaging and DVC analysis (for LaMcube see Chapter 7).

4.4.1 Part A: Microstructure and mineralogical characterization

Please refer to section 4.3.

4.4.2 Part B: Determination of transport properties

Water permeability

Prior to the percolation experiments, the permeability of mortars and clay are determined separately using a controlled constant flow method as described in (Phung et al., 2013).The method is based on

the application of a constant flow instead of a constant pressure in traditional methods, which overcomes the problem of measuring extremely low flow rate. A pressure gradient of around 5 to 10 bar is applied by controlling the pressure at both sides of a saturated sample embedded in a permeability cell (Figure 4-8). When the flow almost reaches steady state, the constant pressure mode is changed to the constant flow mode. The pressure is then measured until reaching the steady state in pressure, which is much more accurate than measuring flow rate. The pressure and water flow are controlled by precise Syringe pumps. A good contact between the samples (mortars, clay) and the permeability cell is obtained by using high strength and low viscosity resins. This method seems promising in terms of the required experimental time and the parameter control. It is also very flexible for further testing in which two permeability cells (one for clay and one for mortars) can be reassembled to have a percolation cell (Figure 4-7) for percolation experiments. With this method, we are able to determine the permeability coefficient of mortars/ clay in a relative short time compared to other methods (within 1 week for permeability of 10^{-13} m/s).

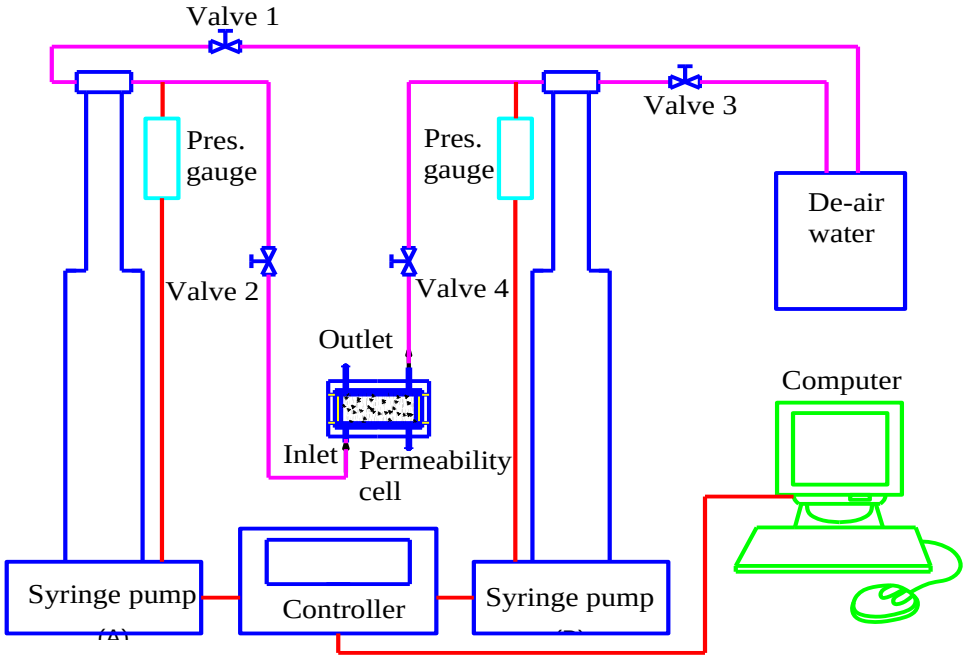

Figure 4-8: Schematic test setup for permeability determination

The composite permeability of clay and mortar samples can be calculated at any specific time during percolation experiments. At a certain interaction time, the percolation cell is decoupled (separate clay and mortar samples) for determination of the permeability of each material after having interacted for a known period of time.

Dissolved gas diffusivity

Similar to permeability, we determine the diffusion coefficients of mortars and clay before and after a certain time of interaction. We use a through-diffusion methodology which allows simultaneous determination of diffusivities of two dissolved gases (He and CH_4) in a single experiment as described in (Jacops et al., 2013; Phung, 2015; Phung et al., 2015). Note that thanks to its compatibility, the permeability/percolation cell can be easily disconnected and then reconnected to the diffusion setup.

Prior to the diffusion measurement, the sealing of the whole system is checked by applying a gas pressure of about 10 bar and following the pressure evaluation over time. Care must be taken to avoid testing gas contamination of each vessel (i.e. gas 1 present in vessel 2 and vice versa). A volume of 0.5 litre of degassed water is added to each vessel, whereafter they are pressurized by the respective gases to a similar pressure of about 10 bar to prevent advective transport. Gas samples are regularly (generally every 2 weeks) taken via external samplers until enough data points are collected to obtain diffusivity. The gas composition are analysed with a micro gas chromatograph. In order to interpret the

experimental data, a 1-D diffusive transport model has been used (Jacops et al., 2013), which takes into account the drop of gas pressure during sampling.

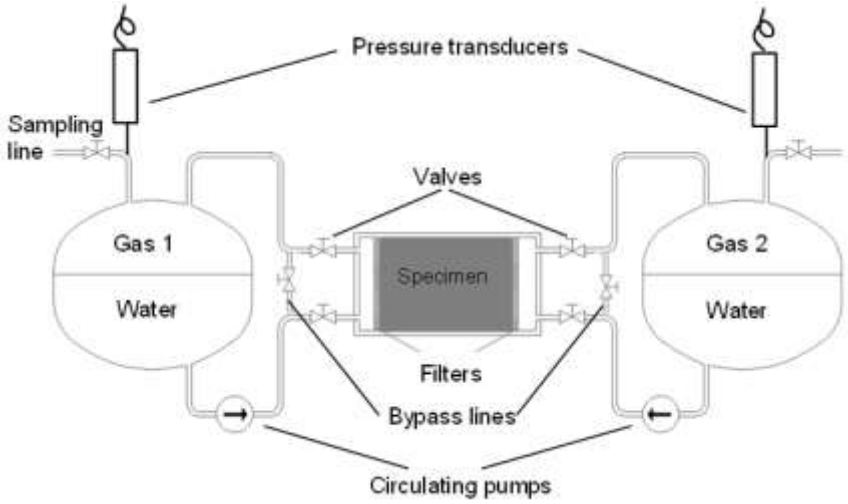

Figure 4-9: Schematic experimental setup to measure diffusivities of dissolved gases (Jacops et al., 2013; Phung, 2015; Phung et al., 2015)

Water sorptivity

Considering extremely slow concrete-clay interaction, the degraded depths, especially at the (high strength) concrete side, are expected to be limited. Our initial observations on few concrete samples taken from HADES underground research facility showed that the degraded depths were only few hundreds µm for 13 years of interaction, which are indeed not sufficient to perform permeability or diffusion measurements mentioned in previous sections. Therefore, we perform a water sorptivity test which is relevant to characterize the transport properties of an exposed surface of concrete or clay.

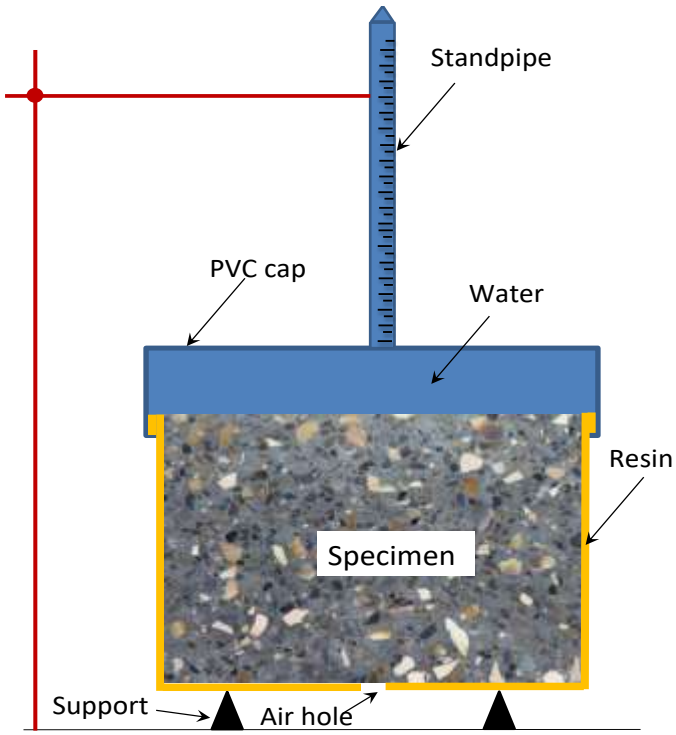

Figure 4-10 Schematic experimental setup to measure water sorptivity

As the sorptivity is strongly affected by the water saturation of the sample, conditioning the samples is very important. Normally, the equilibrium relative humidity (RH) of the sample should be around 60% (ASTM, 2004). However, it could take a few months to years to reach equilibrium at such RH depending on the size of sample. In this study, we dry the sample in an oven at 50°C. This gentle temperature is chosen to, on one hand, reduce the conditioning duration and, on the other hand, prevent cracking to occur due to heating and decomposition of water in C-S-H phase. Furthermore, the required duration to perform water sorptivity tests on dried samples will be much shorter than on partially saturated samples.

The schematic sorptivity setup is shown in Figure 4-10. In this setup, water is on top of the concrete surface, gravity also will play a role in the water penetration. However, water ingress into the sample is mainly driven by capillary forces as it is much larger than water gravity (water head is about 0.5 m). The size of the sample is similar to the one for permeability/diffusion tests. The entire surface of the dry sample is covered by a resin except for the interface and a small area at the bottom to allow air to escape during sorption. In this way, sorption only occurs one-dimensionally, at the interaction surface. The volume of water absorbed by the sample is determined by following the level of the standpipe.

The sorption coefficient is defined as shown in the following equation:

$$I = \frac{W}{A} = S\sqrt{t} + I_0$$

where I = cumulative water absorption on tested surface [mm³¬/mm²]; W = volume of water absorption [mm³]; A= tested surface [mm²]; t = time variable [min]; S = sorption coefficient [mm/min$^{1/2}$]; and I_0 = initial water absorption [mm³¬/mm²]. Water sorptivity is one of the independent transport indicators. However, the water sorptivity is strongly related to (unsaturated) permeability (and thereby diffusivity) and capillary pressure which depends on microstructure and water content of the sample (Kelham, 1988).

4.5 Characterisation of cementitious material to be performed in MAGIC

4.5.1 Mechanics

E-modulus, compressive strength, tensile strength, cohesion, friction angle, etc. - via micro-indentation and mechanical tests (classical uniaxial and bending tests) on both the ‘intact’ sample (reference sample) and ‘chemically degraded at different levels’ samples. Furthermore the triaxial compression tests will be performed on (~ 10) degraded samples in collaboration with LaMcube, CNRS in order to obtain the stress-strain curves, elastic properties and peak strengths, which will be used for calibration and validation of multi-scale models.

Furthermore, the microscopic uniaxial compression creep tests with micro-tomographic imaging and DVC analysis (collaborated with LaMcube see Chapter 7) will be performed on cylindrical samples with 5mm diameter and 10mm thickness.

4.5.2 Transport properties

Alteration in transport properties will be characterized via diffusion, permeability and water sorptivity experiments as explained in section 4.3.

4.5.3 Chemical and mineralogical properties

Carbonation, leaching induced mineralogical and microstructural changes will be characterized via multiple techniques (SEM/EDX, TGA, XRD, FTIR, MIP).

4.5.4 Microbical

We will monitor microbial communities in percolate solution, biofilm formation and analysis on cementitious material and identification of mineral phases precipitated by microbes – via flow cytometry, ATP, IC. STEM/HAADF, SEM/EDX, fluorescence microscopy, Field Emission Electron Microscope associated with Raman Spectroscopy (EEM/RS), and sequencing technologies. These analyses will be partially done by University of Granada, who will receive around 12 samples from SCK CEN for STEM/HAADF and EEM/RS. This sophisticated microscope allows to analyse the samples at nanoscale regarding the distribution of microorganisms in the surface of concrete, to characterize the mineral phases precipitated on the material surface by microbial activity (formation of biogenic Ca carbonates, etc.). These studies will be complemented by using Field Emission Electron Microscope associated with Raman Spectroscopy, which allow also to investigate the presence of biofilm on the concrete surface and to identify the mineral phases precipitated by microbes."

4.6 References

ASTM. (2004). ASTM C 1585-04: Standard Test Method for Measurement of Rate of Absorption of Water by Hydraulic-Cement Concretes. 6.

Chen, G., Dizier, A., Li, X., Verstricht, J., Sillen, X., & Levasseur, S. (2021). Numerical Prediction of the Large-Scale in Situ PRACLAY Heater Test in the Boom Clay. Rock Mechanics and Rock Engineering, 54(5), 2197-2218. https://doi.org/10.1007/s00603-021-02405-2

Jacops, E., Phung, Q.T., Frederickx, L., Levasseur, S. (2021) Diffusive transport of Dissolved gases in Potential Concretes for Nuclear Waste Disposal. Sustainability. 13(18), 10007.https://www.mdpi.com/2071-1050/13/18/10007

Jacops, E., Volckaert, G., Maes, N., Weetjens, E., & Govaerts, J. (2013). Determination of gas diffusion coefficients in saturated porous media: He and CH4 diffusion in Boom Clay. Applied Clay Science, 83–84(0), 217-223. https://doi.org/http://dx.doi.org/10.1016/j.clay.2013.08.047

Kelham, S. (1988). A water absorption test for concrete. Magazine of Concrete Research, 40(143), 106-110. https://doi.org/doi:10.1680/macr.1988.40.143.106

Phung, Q. T. (2015). Effects of Carbonation and Calcium Leaching on Microstructure and Transport Properties of Cement Pastes [PhD thesis, Ghent University]. Belgium.

Phung, Q. T., Maes, N., De Schutter, G., Jacques, D., & Ye, G. (2013). Determination of water permeability of cementitious materials using a controlled constant flow method. Construction and Building Materials, 47(0), 1488-1496. https://doi.org/http://dx.doi.org/10.1016/j.conbuildmat.2013.06.074

Phung, Q. T., Maes, N., & Jacques, D. (2017). Application of Multiple Techniques to Quantify Pore Structure of Degraded Cementitious Materials XIV DBMC 14th International Conference on Durability of Building Materials and Components, Ghent, Belgium.

Phung, Q. T., Maes, N., Jacques, D., Jacop, E., Grade, A., Schutter, G. D., & Ye, G. (2015). Determination of diffusivities of dissolved gases in saturated cement-based materials International Conference on Concrete Repair, Rehabilitation and Retrofitting IV, Leipzig, Germany.

5. Czech samples

Authors: Lucie Hausmannová (SURAO), Radek Vašíček (CTU), Petr Večerník (UJV), Veronika Hlaváčková and Kateřina Černá (TUL) and Tomáš Černoušek (CV Řež)

5.1 Mechanical safety function and performance target

In general, the concrete components in DGRs for spent nuclear fuel (SNF) constructed in crystalline rocks play a role primarily during the operational phase of the facility, which means that the mechanical safety functions of these concrete elements will be required to function for approximately 130 years. Hence, these components are included in the operational safety rather than the long-term safety stage of DGR development. Since such concrete elements will be situated mainly in the operational part of the DGR, which will be ventilated most of the time, they will be exposed to temperatures close to the initial ambient temperature conditions (15-25°C).

Concrete will be used in the Czech DGR for SNF in the construction of sealing plugs and as a general building material (i.e. for the floors, walls, supporting construction elements, shotcreting). Since the layout of these elements and the various requirements have not yet been specified in detail in the Czech DGR concept, the current aim is to demonstrate the fulfilment of those requirements which commonly apply to the use of construction concrete in underground structures. The preference will be for the use of low pH concrete, which only became available (made from Czech raw materials) in 2018, thanks, to a considerable degree, to the CEBAMA project (FP7 EURATOM).

The Czech research with respect to the MAGIC project is concerned with a concrete material with a reduced pH (LPC) which was designed as recently as in 2018-2019 and which is referred to as LPC_SURAO (Pernicová et. al, 2019). Since no information concerning its long-term behaviour, the aim of the Czech research part of the MAGIC project is to evaluate the mechanical behaviour of this material under simulated DGR conditions and to demonstrate its stability over time.

5.2 Size of the samples, concrete recipe

The test samples comprise specially-designed concrete with a reduced pH – LPC_SURAO.

The samples were prepared via a large-volume casting process which resulted in the production of 150 samples. Casting took place on 21 June 2019 and the samples were moved to the Bukov URF underground laboratory on the following day. The conditions at the URF are as follows: air humidity of 95±5% and temperature of 15±2°C, i.e. conditions that closely resemble those of the future Czech DGR during the operational phase. The samples comprised standard cubes with dimensions of 15 cm. The concrete recipe is shown in Table 5-1.

Table 5-1: LPC_SURAO recipe

Component	Type	kg m^{-3} of each component
Cement	CEM I 42.5 R	140
Microsilica	Elkem 970	179
Slag	CEMEX Czech Republic s.r.o (white powder)	32
Water	tap	200
Aggregate 1	sand 0- 4 mm	895
Aggregate 2	aggregate 4/8 mm	413
Additive 1 -plasticiser	Glenium ACE 300 liquid plasticiser	7
Additive 2 - defoamer	Aqitan P841 - powder	1.75

5.3 Characterisation of the cementitious material

The samples of the recently designed LPC_SURAO reduced pH concrete material were sufficient for both the initial characterisation and the long-term testing phases; the characterisation phase comprised the testing of samples after 28, 60 and 90 days. The samples were matured under laboratory conditions

according to standard procedures (Pernicová et al., 2019). After the samples intended for long-term testing had been transferred (one day following casting) to the Bukov URF underground laboratory, the first set of samples was tested after 174 days (Citek et al., 2020). The MAGIC project will continue with the further treatment and testing of the matured concrete samples.

5.3.1 Mechanics

The LPC_SURAO material was tested in the unloaded state. A series of mechanical tests was performed after 28, 60 and 90 days and included the evaluation of the compressive strength and the modulus of elasticity. These samples were stored under laboratory conditions.

The samples to be tested as part of the MAGIC project were cast together with the laboratory samples but they were stored under underground laboratory conditions; these “Bukov” samples were tested for compressive strength after 174 days.

5.3.1.1 Compressive strength

The compressive strength testing was performed according to EN 12390-3. Three concrete samples in the form of cubes with dimensions of 150 mm were subjected to investigation. After 24 hours of the maturing of the concrete in the mould, the samples were removed from the mould and stored in an aquatic environment (potable water at a temperature of 20°C ± 2°C). One day before the commencement of testing, the samples were stored in an air environment at 23°C ± 2°C.The test results are shown in Table 5-2.

Table 5-2: Compressive strength, modulus of elasticity and pH of LPC_SURAO (N.A. = not analysed)

Days	Compressive Strength [MPa]	Modulus of Elasticity [GPa]	pH
28 (lab)	47.60	28.30	11.01
60 (lab)	50.80	27.80	10.84
90 (lab)	52.30	28.30	10.73
174 (Bukov)	53.50	N.A.	10.98

5.3.1.2 Modulus of Elasticity

The principle of the test for the determination of the static modulus of elasticity under compression according to ISO 1920-10 comprises the exposure of samples to a tension of 0.5 MPa and to one third of the compressive strength of concrete. The relative strains at the corresponding tension levels are then recorded. The modulus of elasticity is calculated by dividing the difference between the basic tension and the upper load tension by the difference in the corresponding strains.

The results are shown in Table 5-2.

5.3.2 pH

The pH testing employed a leaching method using distilled water as the medium (Behnood et al., 2016). The samples were dried at pre-set times (28, 56 and 90 days) and then ground to an analytical fineness. Subsequently, an aqueous leach was prepared from the samples immersed in distilled water. The resulting solution comprised a 1:1 weight ratio (50 g of the sample with 50 ml of distilled water). Leaching was performed for 5 minutes under laboratory conditions (t = 22 ± 3°C, RH = 40%), following which the aqueous solutions (suspensions) of the samples were analysed using a pH meter. A magnetic stirrer was lowered into the samples, which were placed on a magnetic stirring device so as to avoid the settling of the solid particles of the suspension during the pH measurement process. A pH glass electrode, which had been calibrated by means of three-point calibration using buffers, was used to measure the pH. The pH measurement process was performed using an inoLAB Multi 9420 pH multimeter. The results are shown in Table 5-2.

5.4 Description of the experimental set-up

The research will focus on the behaviour of the LPC_SURAO low-pH cementitious material under the conditions anticipated during the operational phase of the repository (10-30°C, saturated and partially saturated; aerobic conditions); the testing programme will include the artificial ageing of the material in three differing environments (water, BCV bentonite, air) followed by the investigation of the various chemical and microbial effects under real underground conditions (the Bukov URF). Czech Ca-Mg BCV bentonite and the local underground water will compose key components of the experimental environment. The experiments will realistically simulate the contact of concrete structures and the bentonite backfill or buffer in the presence of underground water.

Both the bentonite and the underground water evince unique chemistries and comprise primary and long-term sources of bacteria that are transported in solution via the pore system of, and cracks in the concrete. Microbial characterisation of the bentonite source and underground water at URF Bukov from the borehole S25, has been performed (Steinova et al., 2019). This initial microbial characterisation is being performed for the concrete samples within MAGIC. The research will focus on the simultaneous impact of a multi-ionic attack and the impact of the microbial (= natural) environment versus the effect of the chemistry of the material on the mechanical and chemical properties of the low-pH concrete under fully saturated conditions. The samples that were prepared for the testing of the long-term behaviour of LPC_SURAO (Pernicova et al., 2019 and Citek et al., 2020) concrete will be used as the source of the low-pH material for the proposed experimental programme.

The initial characterisation stage will be followed by two ageing phases (approx. 12 and 24 months), both of which will be followed by sampling and the detailed characterisation of the material.

5.5 Characterisation of the cementitious material to be performed in MAGIC

The set of samples (15 cm cubes) of LPC_SURAO stored at the Bukov URF (by SURAO since 2018) will be used as the source of the low-pH material for the proposed experiments. The cubes will be drilled/ cut into a relatively large number of smaller samples (cylinders, discs etc. according to the sampling plan). Prior to the setting up of the experiment under in situ conditions, it is expected that all the samples will be disinfected using UV light so as to eliminate the potential laboratory contamination of the samples during the preparation stage. Following the sampling campaign, some of the samples/material will be subjected to specific preparation processes that correspond to the requirements of the respective tests and the subsequent follow-up procedures (fine cutting, polishing, crushing and milling).

Following the initial characterisation phase (late 2021), two main ageing phases will commence of 12 and 24 months, respectively, to be followed by the detailed multidisciplinary testing of the material (mechanical, chemical, biological, microstructure). Supplementary sampling campaigns (over shorter periods of 3-6 months) will be performed aimed at obtaining results/data from a limited number of samples for mechanical testing purposes; certain other support analysis will also be performed with respect to a limited number of samples.

5.5.1 Planned analysis

All the samples to be used in the experimental programme will be cut/drilled from the “standard” cubes stored on shelves in the underground complex of the Bukov URF. Following a number of preparatory stages, they will be returned to the Bukov URF and stored in boxes with various (chemical) environments. None of the samples will be mechanically loaded in either the initial or the subsequent stages. Short-term loading is planned only for the purposes of the mechanical tests. The testing will be performed on intact samples.

The study of the interaction of the cementitious material with the groundwater and bentonite suspension will include a detailed chemical analysis as well as the initial characterisation of the samples and the

environments (water, suspension). The parameters to be determined comprise the pH, the conductivity and the dominant cation and anion concentrations.

A list of the tests and the sample sizes is provided in

Table 5-3.

5.5.1.1 Compressive strength

The compressive strength will be investigated involving:

- The original samples (cubes of 15 cm) according to ČSN EN 12390-3; 3 samples in one set (initial, after 12 and 24 months)
- Small cylinders (diameter and height of 5 cm) according to ČSN EN 1926; the main differences compared to ČSN EN 12390-3 comprise the dimensions and shape (the d/h ratio) of the samples; initial characterisation and over 12 and 24 months
- The non-standard compressive punch test – (CGU, 1987; used in the CEBAMA project, reported in Vehmas et. al., 2020); this will allow for the investigation of a large number of samples in series and over time (8-10 samples per series; all the sampling campaigns).

Description of the compressive punch test:

- Samples in the form of discs (“pucks”) of 50 mm diameter and 8 mm thickness designed to maximise the area/volume ratios of the samples – aimed at the study of the role of interaction with the surrounding environment; the intention is to influence as much of the sample as possible via the various interactions;
- The sample is crushed with co-axial punches of 7.98 mm in diameter;
- Initial tests and other sampling campaigns (main campaigns of 12 and 24 months plus support campaigns of 3-6 months);
- The crushing force can be assessed; furthermore, the relationship with the compressive strength can be empirically determined (determination employing 50 mm cylinders or larger if needed)
- Suitable for the monitoring of the evolution of parameters over time (the influence of degradation procedures); the evolution of directly measured quantities (the force in kN) can be observed without the introduction of uncertainties due to the use of empirical relationships for conversion to the “pressure” (MPa);
- Employing the quantities measured by the test apparatus (press) it is possible to infer the deformation values of the samples (the direct measurement approach is problematic with concern to the 8 mm thick samples studied in this part of the project). The non-standard ‘apparent stiffness’ [kN/mm] can be estimated from the proportion of the force increment and the corresponding deformation from the linear part of the test record. It should be emphasised that this will provide only an indicative value; nevertheless, it will help in terms of determining the evolution of the behaviour of the material over time;
- max. load [kN] and apparent stiffness [kN/mm] values are used for comparison purposes due to the application of non-standard sample sizes and shapes (the discs); the recalculation into, and further use of the known compressive strength and modulus of elasticity values would not be reliable in this case.
- The output of the punch tests thus comprises the force at break [kN] and “apparent stiffness” [kN/mm] values.

Table 5-3: Overview of the planned analysis

CZ	Test type	Analysis performed	Sample type
Mechanical	Destructive	Uniaxial strength	cylinder d50*h50 mm (cubes 15 cm)
	Destructive punch test	Uniaxial punch strength, elasticity (indicative only)	plate d50*h8 mm

	Non-destructive	Elastic modulus (Impulse ultrasound method)	cylinder d50*h50 mm
*Transport + microstructure	Transport	Hydraulic conductivity	cylinder d42*h84 mm, cylinder d50*h50 mm
	Microstructure/pore space description - porosity measurement	Saturation method + mercury intrusion porosimetry	plate d50*h8 mm, coupon
Chemical	Characterisation of the materials	Instrumental analysis, XRD and SEM	
	Characterisation of the solid phases	Bulk chemical analysis, XRF	
	Characterisation of the surrounding environment (liquid phases - water, suspension)	Chem-phys. properties (pH, ORP, conductivity) and chemical composition analysis (AAS, CE, UV/VIS)	
	Characterisation of the interaction boundaries and the interacted/degraded solid phase	Chemical composition analysis (AAS, CE, UV/VIS, TOC) changes in the pH of the cement/concrete	
Microbiological	Extraction of DNA from swabs taken from the surface of the concrete - biofilm formation	NGS - 16S rDNA sequencing - microbial detection and determination (metagenomics) of the real-time PCR - microbial quantification (different markers for different microbial groups)	plate d50*h8 mm
	Extraction of DNA from the concrete matrix - microorganisms in the concrete		plate d50*h8 mm
	Extraction of DNA from the water/bentonite - microorganisms in the environment surrounding the concrete samples		Saturated bentonite/water
	Extraction of cells from the water/bentonite	Epi-fluorescent microscopy - microbial detection and quantification, estimation of living and dead cells	Saturated bentonite/water

5.5.1.2 Young's modulus

The ultrasonic pulse velocity method will be used for the determination of the dynamic modulus of elasticity by means of a PUNDIT PL200 ultrasonic device (Proceq, SA) according to ČSN 73 1371.

An alternative approach to the determination of the "stiffness", i.e. the "apparent stiffness" using the punch test is mentioned in the previous section of this report (see above).

5.5.1.3 Porosity

The determination of the porosity is important both in terms of its influence on the mechanical properties and for the evaluation of the transport properties of the tested materials. The literature describes several methods for the determination of the porosity of cementitious materials, e.g. the evaporable water content, re-saturation, solvent exchange, mercury porosity and nitrogen sorption approaches (Day and Marsh 1988). However, all these methods have their advantages and disadvantages, which are capable of affecting the pore structure of the cementitious material (Collier et al. 2016, Diamond 2000).

Porosity (in percent) is calculated as the ratio of the pore volume (V_P) and the total volume of the sample (V_S):

$$\varepsilon = \frac{V_P}{V_S} \cdot 100$$

Mercury porosimetry

The mercury porosimetry technique is based on the penetration of mercury into the pores as a function of the applied pressure. Mercury does not wet most substances and will only penetrate pores when

forced to do so under high pressure. The entry of mercury into pores requires the application of pressure in inverse proportion to the pore size. Thus, the larger pores are filled first, followed by the smaller pores which are filled at increasingly higher pressures. Mercury exhibits a high contact angle against most solids; reported contact angles vary but the most widely used values are > 90°, with 130° being the most common value. Mercury thus penetrates the pores only under the action of pressure. The average pore radius ranges from 10^{-8} - 10^{-4} m. The volume of mercury injected into the porous system is generally interpreted as the total volume of the pores in the measured sample.

Saturation and gravimetric method

Sample porosity values can also be obtained via the gravimetric and saturation method as inspired by the determination of rock porosity published by Melnyk and Skeet (1986). The laboratories of ÚJV have considerable experience of the use of this procedure on rock samples and other materials, including concretes. The saturated, surface dry weight (W_S) is calculated from the drying curve. The weight of the submerged sample (W_A) is obtained via the weighing of the sample immersed in the saturating medium. A further required value comprises the weight of the dry sample (W_D).

The pore volume (V_P) and the total sample volume (V_S) are calculated from the determined values according to the following equations:

$$V_S = (W_S - W_A)/\rho$$

$$V_P = (W_S - W_D)/\rho$$

where ρ is the density of the solution used for the saturation of the sample. The porosity ε is then calculated as follows:

$$\varepsilon = \frac{V_P}{V_S} = \frac{(W_S - W_D)}{(W_S - W_A)}$$

Note that the solution density is no longer required for the porosity calculations. Therefore, it is possible to use any appropriate liquid for saturation purposes and for the determination of the weight of the submerged sample.

Isopropanol is used as the saturating medium for the measurement of porosity via the saturation and gravimetric method due to the necessity to avoid the further interaction of the dried cementitious material.

5.5.1.4 Hydraulic conductivity

The permeability of samples (e.g. rock, concrete) is determined at both the CTU and ÚJV laboratories according to the technical specifications ČSN ISO/TS 17892-11:2004 and ČSN ISO 17892-11:2019, a method that employs a constant hydraulic head. ÚJV employs triaxial permeability testing equipment developed in-house; GDS ELDPC pumps are used for measurement purposes, whereas CTU uses a Hydromatic pressure volume controller and a testing cell with a uniform chamber pressure (bi-axial pressure cell). In both cases, the hydraulic head and the background pressure in the device chamber are adjusted according to the properties of the respective sample and the project requirements.

5.5.1.5 Mineralogy

The laboratory for the scanning electron microscopy (FIB-SEM) and X-Ray Diffraction (XRD) research is located at the Diagnostic Centre for Highly Sensitive Analytical Instruments (CVCAP). This laboratory is used for the study of non-irradiated (FIB-SEM) and irradiated samples (XRD).

XRD

Instrument: the Empyrean X-ray Difractometer III. – Malvern Panalytical (installed in November 2019) is a latest generation XRD device. It has an X-ray source, an automatic iCore module and automatic secondary dCore module and a PIXcel 3D surface detector, DataCollector software for the control of the device and data collection (PANViewer and XRD2DScan for working with 2D data - Software Stress, Stress Plus (layers) and Texture - compressor). The advantages of this configuration concern maximum data quality for transmission and automatic measurement using the iCore and dCore modules. Differing samples and measuring methods can be combined in one program: reflection, transmission, GI, reflectivity, tension, textures and SAXS. Measurements can be performed automatically on a single sample or when the sample exchanger is used or more samples placed on a 5-axis cradle, measurements can be taken automatically by all the above-mentioned programs for multiple samples.

Methods used for the matrix characterisation: Phase ID and Quantification (using the Rietveld analysis of XRD patterns), the determination of crystallinity – the quantification of the amorphous content using the internal-standard method, the structure determination and the monitoring of changes in the lattice parameters of the identified crystalline phases, Transmission XRD and Small-Angle X-ray Scattering (SAXS). The identification of the phases is performed with HighScore+ software (PANalytical, the Netherlands, version 4.8) including a PDF-4 database. The Profex 4.0.3 software package is used for the quantitative analysis of the samples with structural models taken from the American Mineralogist and COD databases. This program allows for the estimation of the weight fractions of the crystalline phases via the Rietveld refinement procedure.

FIB-SEM

Instrument: Scanning electron microscope (SEM), LYRA3 GMU, (TESCAN co.) with an auto-emission electron source (Field Emission Gun, FEG) for the chemical (EDS, WDS – Oxford Instruments) and crystallography (EBSD – Oxford Instruments) characterisation. A microscope for the analysis of metallic and non-metallic materials in the low or high vacuum mode with C, Au coated specimens.

Methods used for the matrix characterisation: SE/BSE/in-beam SE or BSE/STEM imaging, qualitative and quantitative electron microanalysis using EDS/WDS analysers, elemental mapping – the distribution of elements in the samples, the phase ID and the crystallographic orientation of phases using EBSD following the preparation of the samples with FIB.

5.5.1.6 Pore water chemistry

The pore water composition will be described via the dominant cation concentration (Na^+, K^+, Ca^{2+}, Sr^{2+}, Mg^{2+}, $Fe_{(tot)}$, $Al_{(tot)}$) and the dominant anion concentration (SO_4^{2-}, Cl^-, HCO_3^-/CO_3^{2-}, SiO_3^{2-}) via the application of various analytical techniques, e.g. AAS (atomic absorption spectrometry), ICP-MS (inductively coupled plasma mass spectrometry), ICP-OES (inductively coupled plasma optical emission spectrometry), CE (capillary electrophoresis), IC (ion chromatography), etc.

Measuring of the pH of leachates

The recommended procedure for the pH determination of low-pH leachates from concretes is described in the SKB R-12- 02 report: Development of an accurate pH measurement methodology for the pore fluids of low pH cementitious materials (Alonso et. al., 2012).

5.5.1.7 Microbiology

The 3-year-old samples from the Bukov URF will be cut into pieces and subjected to various ageing environments (humid air, underground water, saturated bentonite) under the in situ conditions of the URF. During the course of the experimentation (maximum 2 yrs), the microorganisms present in these environments are expected to gradually evolve and colonise the concrete samples. Our experimental approach will address all the applied conditions and we intend to extract the total bacterial DNA from the underground water, bentonite and concrete samples (Table 5-4). The concrete will be sampled in three ways – the composition of the outer surface biofilm will be determined using swabs. The concrete samples supposed to be subjected to UV light so as to eliminate the residual bacterial biofilm and will then be manually crushed and milled using a Retsch MM400 in sterile milling chambers. The concrete

powder will provide the material for the direct DNA extraction as well as for further processing aimed at determining the microbial composition of the bulk concrete.

The determination of the microbial activity will be based mainly on molecular genetics methods (16S-rRNA amplicon sequencing and quantitative PCR) for which the total DNA from all the samples will be extracted. The process applied for the extraction of DNA from environmental water and clay samples has been well documented (Bagnoud et al., 2016; Engel et al., 2019; Itävaara et al., 2008; Kašpar et al., 2021). Unfortunately, however, the extraction of DNA from low DNA concrete samples is not straightforward (Maresca et al., 2016). Traditional protocols for the extraction of DNA from cementitious materials are ineffective, most probably since the DNA molecule is subjected to irreversible denaturation in conditions where the pH exceeds a value of 12 (Ageno et al., 1969). Therefore, we will combine the genetics approach with cultivation experiments. We are very well aware of the fact that the majority of bacterial species in average soil samples are uncultivable (Blagodatskaya and Kuzyakov, 2013). However, concerning samples with extremely low microbial activities that result in a low-DNA yield following DNA extraction, DNA-based methods fail to provide reliable data due to the detection limits. In this case cultivation methods have the potential to help in the determination of at least the cultivable microbial species. The concrete powder will be subjected to cultivation in 2-3 differing media under oxic and anoxic conditions. Moreover, the microbial viability will be estimated via the visualisation of stained vital cells using a cell extraction protocol from the saturated bentonite (Hlavackova et al., in preparation).

Table 5-4: Overview of the planned analysis of the samples (performed -x, not performed – o)

Type of sample	microscopy	NGS	qPCR	cultures
underground water	o	x	x	o
saturated bentonite	x	x	x	o
concrete - out	o	x	o	o
concrete - in	o	x	o	x

Amplicon sequencing

16S-rRNA amplicon sequencing is currently the most common method applied for the determination of the microbial diversity of environmental samples. The method is based on the variability of the genomic sequence that encodes the small ribosomal subunit (16S rRNA) that allows for distinguishing between differing bacterial taxonomic levels. The specific region of the 16S rRNA gene is multiplied using specific primers for 16S rRNA (Table 5-5) in a polymerase chain reaction (PCR). Precise sequences are then read from the amplified regions and compared to publicly-available sequence databases. We use SILVA, a quality-controlled database of aligned ribosomal RNA (rRNA) gene sequences from the Bacteria, Archaea and Eukaryota domains (Quast et al., 2013). If the detected sequence is present and annotated in the database, the particular species can be assigned to the discovered sequence.

Table 5-5: Primers used for the 16S rRNA amplicon sequencing

Primer	Sequence	Reference
515F	TGCCAGCMGCNGCGG	*(Dowd et al., 2008)*
802R	TACNVGGGTATCTAATCC	*(Claesson et al., 2010)*

Quantitative PCR (qPCR)

This method allows for the quantification of specific DNA sequences via the continual detection of amplified DNA over every PCR cycle. It is facilitated by adding a specific or unspecific fluorescent DNA marker, e.g. SYBR Green where the intensity of the fluorescent signal is proportional to the amount of double stranded DNA after each PCR cycle. The Ct value (the number of cycles required for reaching

the threshold of the fluorescent signal by means of a detector) can be estimated from the growth of the fluorescent signal. Hence, the Ct value is inversely proportional to the initial DNA concentration. This method can be used for the estimation of the total microbial biomass using 16S rRNA primers or a particular group of microorganisms using primers that target specific genes (Table 5-6), e.g. for nitrate (NRB), iron (IRB) or sulphate (SRB) reducers (nitrous oxide reductase, dissimilatory sulphite reductase etc.).

Table 5-6: Primers used for the qPCR analysis of bacterial metabolic communities

Primer	Sequence 5'-3'	Specificity	Reference
16SqPCR-F	TCCTACGGGAGGCAGCAGT	bacteria	*(Nadkarni et al., 2002)*
16SqPCR-R	GGACTACCAGGGTATCTAATCCTGTT		
NosZ-F	CGYTGTTCMTCGACAGCCAG	Dissimilatory nitrous oxide reductase (NRB)	*(Geets et al., 2007)*
NosZ-1622R	CGSACCTTSTTGCCSTYGCG		
Geo494F	AGGAAGCACCGGCTAACTCC	16S – Geobacteraceae (IRB)	*(Holmes et al., 2002)*
Geo825R	TACCCGCRACACCTAGT		
RH1-dsr-F	GCCGTTACTGTGACCAGCC	Dissimilatory sulphite reductase (SRB)	*(Ben-Dov et al., 2007)*
RH3-dsr-R	GGTGGAGCCGTGCATGTT		

Our experiments have been designed to address various interstitial environments in the future DGR. Firstly, a concrete/humid air environment that simulates that of the end-plug of the DGR that will face the underground service establishments. Secondly, a concrete/underground water environment which will simulate the more reactive conditions of the ageing of the concrete via the action of underground water originating from nearby rock defects. And, finally, a concrete/bentonite environment that simulates the most reactive conditions involving the presence of a vast number of indigenous bentonite microorganisms that could cause the severe deterioration of the concrete plugs in the DGR. Since the use of this setup will not enable us to distinguish between the effects of chemically and microbially triggered ageing on the mechanical properties of the concrete, it is anticipated that we will include the study of a batch of sterilised bentonite samples saturated with sterile underground water. Concrete and bentonite samples will be separately sterilized by irradiation till doses of 40 to 100 kGy. Sterilized bentonite powder will be mixed with autoclaved underground water (same source as for the experiment). Sterilized concrete samples will be submerged into the bentonite suspension. Unfortunately, the results of the sterilisation of the bentonite will be subject to uncertainty since bentonite is also inhabited by sporulating microorganisms, and the spores are able to survive very harsh conditions, high temperatures and pressures, desiccation and irradiation (Nicholson et al., 2000; Potts, 1994).

5.6 References

Ageno, M., Dore, E., Frontali, C., 1969. The Alkaline Denaturation of DNA. Biophysical Journal 9, 1281–1311.

Alonso M. C., García Calvo J. L., Walker C., Naito M., Pettersson S., Puigdomenech I., Cuñado M. A., Vuorio M. Weber H., Ueda H., Fujisaki K. (2012): Development of an accurate pH measurement methodology for the pore fluids of low pH cementitious materials, SKB report R-12-02, SKB, Stockholm.

Bagnoud, A., Chourey, K., Hettich, R.L., De Bruijn, I., Andersson, A.F., Leupin, O.X., Schwyn, B., Bernier-Latmani, R., 2016. Reconstructing a hydrogen-driven microbial metabolic network in Opalinus Clay rock. Nature communications 7, 12770.

Behnood A., Van Tittelboom K., De Belie N. (2016): Methods for Measuring pH in Concrete: A Review – Construction and Building Materials, 105, pp. 176-188.

Ben-Dov, E., Brenner, A., Kushmaro, A., 2007. Quantification of sulfate-reducing bacteria in industrial wastewater, by real-time polymerase chain reaction (PCR) using dsrA and apsA genes. Microbial ecology 54, 439–451.

Blagodatskaya, E., Kuzyakov, Y., 2013. Active microorganisms in soil: Critical review of estimation criteria and approaches. Soil Biology and Biochemistry 67, 192–211.

Citek D., Dobias D., Hurtig K., Kratochvile L., Kolisko J. (2020): Zkoušky betonu – dlouhodobě uložené vzorky a zkoušky stříkaného betonu. – SURAO TZ480/2020, 21 p

Claesson, M.J., Wang, Q., O'sullivan, O., Greene-Diniz, R., Cole, J.R., Ross, R.P., O'toole, P.W., 2010. Comparison of two next-generation sequencing technologies for resolving highly complex microbiota composition using tandem variable 16S rRNA gene regions. Nucleic acids research 38, e200–e200.

Collier N. C., Sharp J. H., Milestone N. B., Hill J., Godfrey I. H. (2016): The influence of water removal techniques on the composition and microstructure of hardened cement pastes, Cement and Concrete Research 38, 737–744

Český geologický úřad (1987). Metodiky laboratorních zkoušek v mechanice zemin a hornin. Zavoral J. (ed.); Praha. In Czech.

ČSN 73 1371: Non-destructive testing of concrete - Ultrasonic pulse method for testing concrete, Czech Standards Institute, Prague 2011, 12 p.

ČSN EN 12390-3: Testing hardened concrete - Part 3: Compressive strength of test specimens. Czech Standards Institute. Prague 2009, 24 p.

ČSN EN ISO 17892-11:2019: Geotechnical investigation and testing — Laboratory testing of soil — Part 11: Determination of permeability, Czech Standards Institute. Prague 2019

ČSN ISO/TS 17892-11:2004: Geotechnical investigation and testing — Laboratory testing of soil — Part 11: Determination of permeability by constant and falling head. Czech Standards Institute. Prague 2004

Day R.L., Marsh B.K. (1988): Measurement of Porosity in Blended Cement Pastes, Cement and Concrete Research 18, 63–73

Diamond S. (2000): Mercury porosimetry: An inappropriate method for the measurement of pore size distributions in cement-based materials, Cement and Concrete Research 30, 1517-1525.

Dowd, S.E., Callaway, T.R., Wolcott, R.D., Sun, Y., McKeehan, T., Hagevoort, R.G., Edrington, T.S., 2008. Evaluation of the bacterial diversity in the feces of cattle using 16S rDNA bacterial tag-encoded FLX amplicon pyrosequencing (bTEFAP). BMC Microbiol 8, 125.

Engel, K., Coyotzi, S., Vachon, M.A., McKelvie, J.R., Neufeld, J.D., 2019. Validating DNA Extraction Protocols for Bentonite Clay. mSphere 4. https://doi.org/10.1128/mSphere.00334-19

Geets, J., de Cooman, M., Wittebolle, L., Heylen, K., Vanparys, B., De Vos, P., Verstraete, W., Boon, N., 2007. Real-time PCR assay for the simultaneous quantification of nitrifying and denitrifying bacteria in activated sludge. Appl Microbiol Biotechnol 75, 211–221.

Hausmannova L., Dohnalkova M., Citek D., Kolisko J. (2020), Low pH concrete in the Deep geological repository for radioactive waste, Tunel, pg. 54 – 59, availiable at: https://www.ita-aites.cz/files/tunel/2020/tunel_1-20.pdf

Hlaváčková, V., Černá, K., SHRESTHA, R., Bartak, D., Hofmanová, E., Kejzlar, P., ŠEVCŮ, A., in preparation. Affinity binding of bacteria on the bentonite light particles as a tool for detection of viable bacterial community in clay.

Holmes, D.E., Finneran, K.T., O'Neil, R.A., Lovley, D.R., 2002. Enrichment of Members of the Family Geobacteraceae Associated with Stimulation of Dissimilatory Metal Reduction in Uranium-Contaminated Aquifer Sediments. Appl. Environ. Microbiol. 68, 2300–2306.
Itävaara, M., Vehkomäki, M.-L., Nousiainen, A., 2008. Sulphate-Reducing Bacteria in Ground Water Samples from Olkiluoto – Analyzed by Quantitative PCR (Working Report No. 2008–82). Posiva Oy, Finland.
Kašpar, V., Šachlová, Š., Hofmanová, E., Komárková, B., Havlová, V., Apari, C., 2021. Geochemical, geotechnical, and microbiological changes in 3 Mg/Ca bentonite after thermal loading at 150 °C. Minerals 22.
Maresca, J.A., Moser, P., Schumacher, T., 2016. Analysis of bacterial communities in and on concrete. Mater Struct 50, 25. Melnyk, T. W. and Skeet, A. (1986): An improved technique for determination of rock porosity. Can. J. Earth Sci., 23, 1068 - 1074.
Nadkarni, M.A., Martin, F.E., Jacques, N.A., Hunter, N., 2002. Determination of bacterial load by real-time PCR using a broad-range (universal) probe and primers set. Microbiology 148, 257–266.
Nicholson, W.L., Munakata, N., Horneck, G., Melosh, H.J., Setlow, P., 2000. Resistance of Bacillus Endospores to Extreme Terrestrial and Extraterrestrial Environments. Microbiol Mol Biol Rev 64, 548–572.
Oyen, M.L., Cook, R.F. A practical guide for analysis of nanoindentation data. Journal of the Mechanical Behavior of Biomedical Materials, 2(4):396{407, 2009.
Pernicova R., Citek D., Dobias D., Mandlik T., Kratochvile L., Kolisko J. (2019): Development of low pH concrete – SÚRAO ZZ415/2019/Eng, 49 p.
Potts, M., 1994. Desiccation tolerance of prokaryotes. Microbiol Rev 58, 755–805.
Quast, C., Pruesse, E., Yilmaz, P., Gerken, J., Schweer, T., Yarza, P., Peplies, J., Glöckner, F.O., 2013. The SILVA ribosomal RNA gene database project: improved data processing and web-based tools. Nucleic Acids Res 41, D590–D596.
Steinová, J., Burkartová, K. (2019) Mikrobiální screening PVP Bukov a dolu Rožná, Technická zpráva číslo 382/2019.
Vehmas, T.; Montoya, V.; Alonso, M.C.; Vašíček, R.; Rastrick, E.; Gaboreau, S.; Večerník, P.; Leivo, M. et al. (2020). Characterization of Cebama low-pH reference concrete and assessment of its alteration with representative waters in radioactive waste repositories; Applied Geochemistry, 121 ISSN 0883-2927.

6. Dutch samples

Authors: Erika Neeft, Roos van Kleef, Ton de Bruin (COVRA) Guido Deissmann (FZJ) and Kristel Mijnendonckx (SCK CEN)

6.1 Mechanical safety function and performance target

The Dutch disposal programme is at an conceptual stage i.e. the host rock is not yet chosen in the Netherlands, rock salt and poorly indurated clays are both investigated. Also multinational disposal is considered in the Dutch programme (I&E, 2016). The cementitious materials described in this chapter, especially those studied solely for disposal, should therefore be regarded as preliminary choices that may change in the future. Cementitious materials are used for different purposes in the Dutch disposal concept for an underground facility in poorly indurated clay. Figure 6-1 shows that cementitious materials are used as void fill, buffer, backfill, pedestal and liner. The concept of the waste package with buffer and overpack is adapted from the Belgian disposal programme the so-called Supercontainer e.g. (NIROND, 2013). This waste package provides radiological shielding during handling but also prevents contact between the radionuclides in the waste and pore water at least when the waste emits heat. The cementitious materials have different roles:

- The void fill eliminates the void between the overpack and the concrete buffer and therefore facilitates the thermal dissipation of the heat. It also provides the beneficial conditions to limit the corrosion rate of the carbon steel overpack i.e. an alkaline reducing environment and no advection at the interfacing environment with the overpack. The thickness of the void fill is however too small to provide these beneficial conditions for the period in which the waste emits heat in significant amounts, the buffer is required for this post-closure role;
- The buffer provides the beneficial conditions to limit the corrosion rate of the carbon steel overpack for the period that the waste emits heat in amounts that the host rock is heated by the waste. The large thickness of the buffer also contributes to the radiological shielding in the operational phase;
- The backfill's role is similar to the void fill's role i.e. to eliminate the voids between the buffer and liner and therefore facilitate the thermal dissipation of heat;
- The pedestal facilitates the emplacement of the waste package containing the waste canister, overpack and buffer. The pedestal also allows the dissipation of heat in the operational phase of the underground facility;
- The liner is required against the convergence of poorly indurated clay in order to facilitate safe emplacement of the waste packages.

Samples of the cementitious materials with aggregates studied in MAGIC are for backfill and buffer-like materials. The buffer-like material is actually a waste package mortar used for processing of Low and Intermediate Level Waste (LILW) at COVRA's premises with the same performance target as the buffer except that it has a different size of aggregates than the buffer picturized in Figure 6-1.

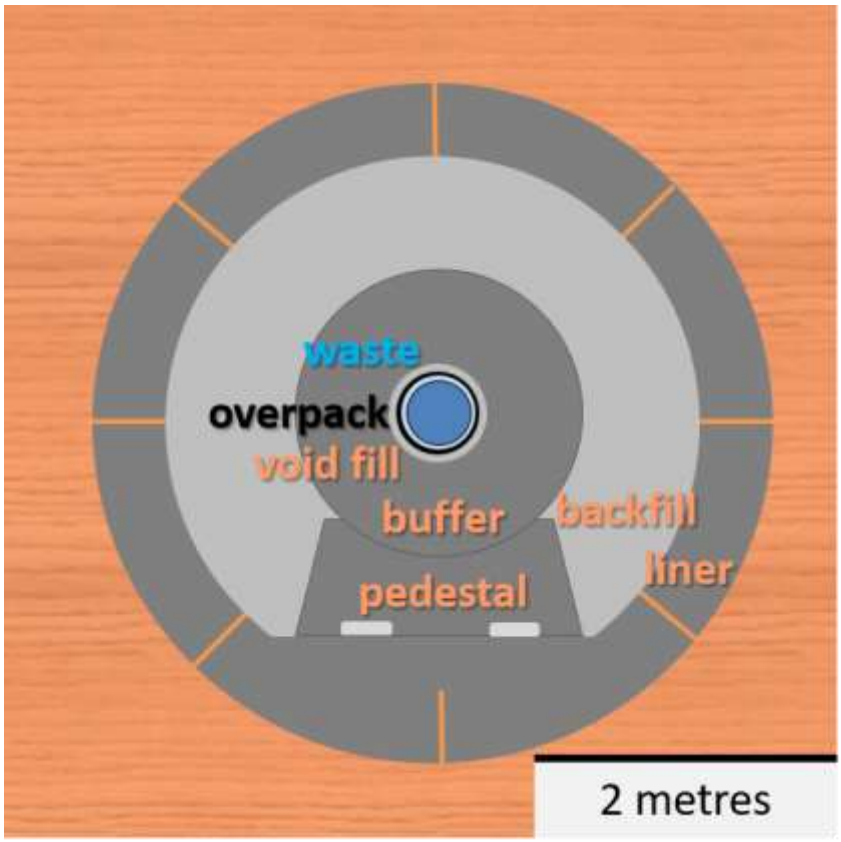

Figure 6-1: Cross section of a closed disposal cell considered in COVRA's research programme.

6.1.1 Buffer

The performance target of the buffer is that the characteristic compressive strength should be at least 45 MPa after 28 days of hardening. This target is to obtain well engineered concrete for ordinary handling with the chosen type of cement. The Dutch programme envisages to dispose waste about 100 years from now; waste is currently stored in surface facilities. Consequently, the thermal power of the heat-generating waste has significantly been reduced at time of disposal. A thermal output of 200 W is assumed at start of disposal for a canister containing vitrified waste (Verhoef et al., 2016). There will be a thermal gradient within the buffer during handling of heat generating waste. The thermal stresses associated with this thermal gradient induce compressive stresses for the buffer near the overpack and tensile stresses near the outer diameter of the buffer. The highest temperatures are expected in the operational phase since the air surrounding the concrete buffer has a smaller thermal conductivity than the backfill. The emission of heat from the buffer into air highly depends on the velocity of air and relative humidity of air. Any contact between the buffer and solid material has impact on the thermal gradient within the concrete buffer and its associated thermal stresses. Figure 6-2 shows the calculated isotherms after encapsulation of this heat generating waste in the concrete buffer after 100 days. For simplicity, the overpack and materials within are simulated with a single material being structural steel but the heat source has the same height as the vitrified waste form in the canister. Figure 6-2 clearly shows that the temperature within the buffer is significantly smaller when the floor on which the buffer rests is included in the calculation.

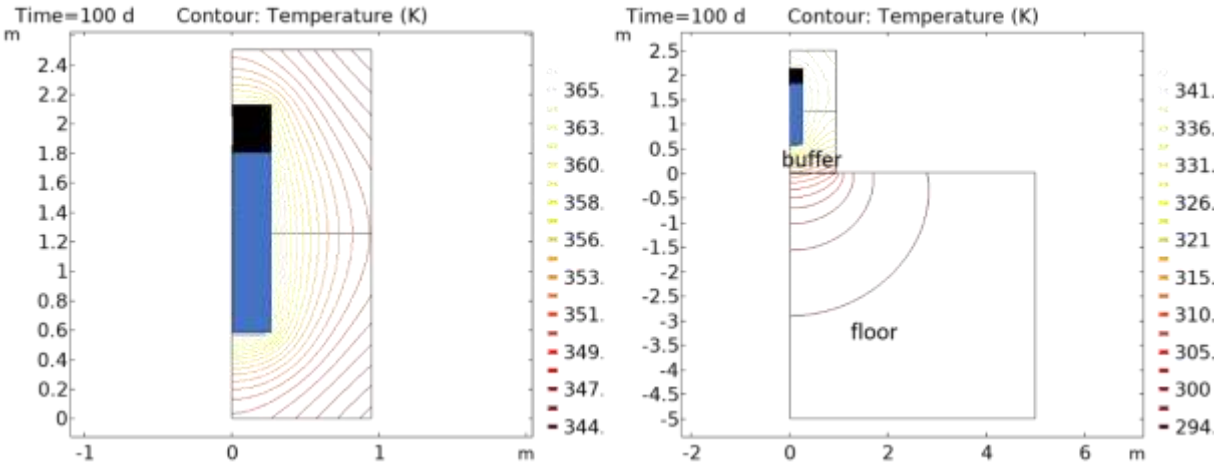

Figure 6-2: Calculated temperatures within the concrete buffer in the operational phase of the disposal process; heat source (blue): 200 W, heat transfer coefficient: 0.25 W m-2K-1, steel and concrete (buffer and floor) properties in Appendix.

Figure 6-3 shows the temperature and pressure at two interfaces as a function of time:

- Concrete interfacing the carbon steel overpack at the point of the midst of the height of the heat source;
- Concrete interfacing air at the point parallel to the midst of the height of the heat source.

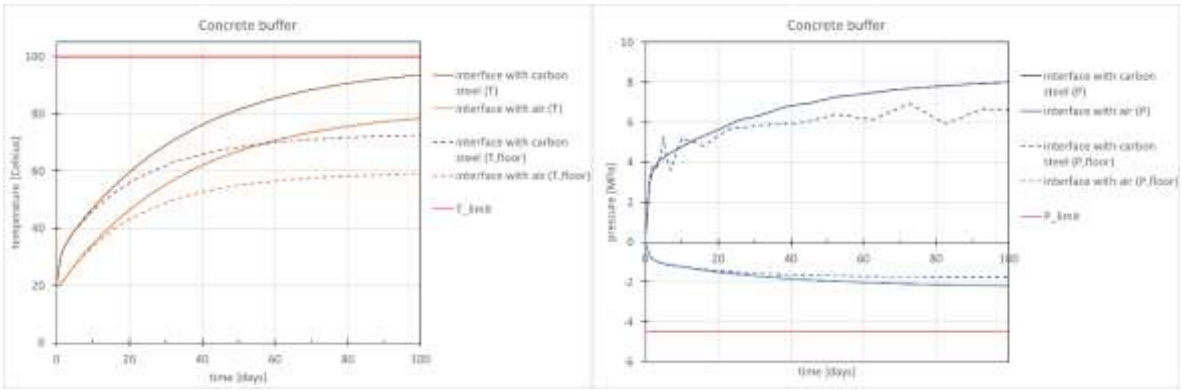

Figure 6-3: Calculated temperatures at two interfaces as a function of time and calculated pressures at these interfaces at the mid of the heat source without floor (solid) and with floor (dashed) lines.

There are several criteria that should not be exceeded. One of them is the temperature. The temperature should remain below 100°C in order to prevent boiling of the concrete pore water. This temperature limit is not expected to be exceeded, especially not when the floor is included in the calculation. Other limits are envisaged to prevent fracturing of the concrete buffer. The compressive stresses induced by the thermal gradient are the positive pressures in Figure 6-3. These positive pressures never exceed the compressive strength. Negative calculated pressures are tractive stresses and should not exceed the tensile strength. The tensile strength can be measured but it is also a fraction of the compressive strength. For example in the third framework programme, the tensile strength was assumed to be one tenth of the compressive strength (Harris et al., 1993) .The calculated negative pressure is significantly less than this fraction of the compressing strength but usually a safety factor of 3 is common in civil engineering i.e. the calculated pressure should be three times less than the tensile strength. Consequently, perhaps additional measures to accommodate tensile stresses, for example the use of reinforcement, may be necessary to provide further confidence that axial cracking of the concrete buffer by the induced thermal gradient does not take place.

The concrete buffer will be fabricated as an engineered impermeable concrete according to the European standard EN 12390-8. This standard is also used to assess the engineered impermeability for concrete plugs in geological disposal facilities in Finland (Vehmas et al., 2016) as well as waste package mortar fabricated at COVRA's premises (Verhoef et al., 2014).

6.1.2 Backfill

The performance target for fabrication for the backfill is that the characteristic compressive strength should at least be larger than the lithostatic pressure in the underground. For example, the compressive strength after 28 days of hardening should at least be 10 MPa for an underground facility at 500 metres depth. There is a thermal gradient through the backfill (and concrete buffer) by heat generating waste at the start of the post-closure phase. Figure 6-4 shows the calculated maximum in temperature (dotted line) and minimum in temperature (solid light blue line) of the backfill. It can be clearly deduced that this thermal gradient diminishes as a function of time; initially the temperature difference between backfill interfacing the concrete buffer and gallery is 11 degrees and after about 1000 years 1 degree.

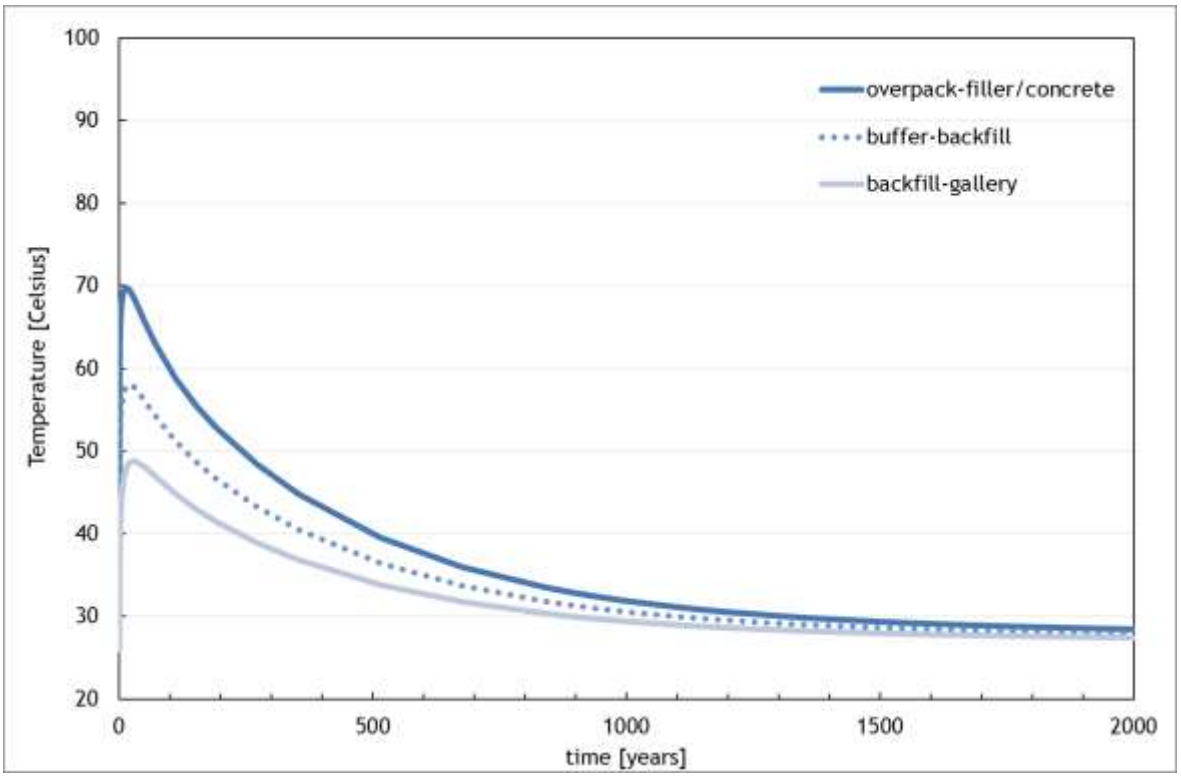

Figure 6-4: Temperature as a function of time at different interfaces for the geometry shown in Figure 6-1 in which the pedestal is assumed to have the same properties as the backfill for simplicity.

6.1.3 Expected chemo-mechanical evolution

The concrete will be altered chemically and this alteration can have an impact on the strength of concrete. Gaseous carbonation occurs in the operational phase of the disposal facility. In the post-closure phase, the chemical alteration mechanism is determined by the type of cement used and rate of ingress of some type of dissolved species. The poorly indurated clay that hosts the disposal facility is envisaged to be situated far below the fresh brackish water interface. As a first approximation, the same salinity as seawater is assumed. The type of cement used to fabricate all cementitious materials is sulphate resistant. Consequently, ingress of sulphate has a negligible impact on the strength of concrete.

6.1.3.1 Gaseous carbonation

The mechanical impact on gaseous carbonation seems to depend on the calcium content of the type of cement used. Concrete made with a blended cement has a more refined pore structure than concrete made with Portland cement (Jackson et al., 2017). The more refined pore structure is important for:

- The equilibrium water content as a function of relative humidity;
- Transport of species within concrete.

The saturation degree is higher for concrete made with blended cement than concrete made with Portland cement for the fabrication of ordinary concrete due to the more refined pore structure at same relative humidity of air and temperature (Neeft et al., 2009). Also in this contribution in paragraph 6.3.1.4, it can be deduced that the saturation degree as a function of the relative humidity is higher for concrete with a finer pore structure. A higher saturation degree limits ingress of CO_2. The more refined pore structure is also important for transport as the connecting pore throats are smaller. Consequently, the rate of ingress of CO_2 is expected to be smaller for concrete made with blended cement than with Portland cement. But the buffer capacity for carbonation is always smaller for concrete made with blended cement compared to concrete made with Portland cement since the CaO-content in blended cements is smaller than for Portland cement. At accelerated carbonation conditions that can be available in the laboratory but not during handling or disposal of waste, the carbonated cement paste made with Portland cement shows a higher modulus of elasticity compared to non-carbonated cement paste while such paste made with 90% blast furnace slag shows a lower modulus of elasticity compared to non-carbonated cement paste (Savija and Lukovíc, 2016). Especially concrete made with slag (and microsilica) underperform in the acceleration carbonation test compared to field conditions (Leemann et al., 2015).

6.1.3.2 Alteration by ingress of magnesium

Poorly indurated clay has a larger porosity than any cementitious material chosen in COVRA's disposal concept. Especially for the concrete used to construct the liner, exposure to synthetic clay pore water is representative for disposal. Any entrance of clay pore water to the backfill is through the joints between concrete segments in the liner. The rate of ingress of species that could alter the cement chemistry of the backfill is therefore expected to be slower than exposure of samples of backfill to synthetic clay pore water. But the investigated processes remain representative for disposal. This rate of ingress of species in clay pore water into the buffer is even slower since the buffer is surrounded by the backfill.

Table 6-1 shows the recipe for fabrication of the synthetic clay pore solution. The fabricated solution is envisaged to be representative for the clay pore water of poorly indurated clays considered in the Netherlands to host a disposal facility.

Table 6-1: Recipe for the synthetic pore solution to which buffer-like samples and samples of backfill have been exposed

Solids	Gram for 1 litre Dutch clay pore water
NaCl	24.475
$MgCl_2$	5.137
Na_2SO_4	4.107
$CaCl_2$	1.177
KCl	0.712
$NaHCO_3$	0.656
KBr	0.102
H_3BO_3	0.043
NaF	0.003846
KI	0.0010
$FeCl_3$	0.01114
$AlCl_3$	0.000346

Ingress of magnesium reacts with the cementitious minerals into brucite and magnesium silicate phases. Magnesium phases have been identified as non-bonding phases (Atkinson, Goult et al. 1985). The

strength of concrete is therefore envisaged to be mainly altered by ingress of magnesium and not by ingress of bicarbonate.

6.2 Size of samples, concrete recipe

Cubical samples with an edge of 15 cm, 10 cm and 5 cm have been fabricated mainly in 2016 and 6 of them in 2015. The buffer-like concrete is a waste package mortar manufactured for processing of waste at COVRA's premises. Special attention is paid to the water content of the aggregates in order to obtain a uniform processing quality of concrete. The minimum weight of batch of concrete is 300 kg. The samples for the backfill are fabricated at two different locations. The backfill is a foamed mortar.

One type of samples for the backfill is fabricated at a COVRA laboratory in batches with several tens of kilograms with a minimum on 22 kg and maximum of 44 kg. Another type of backfill samples is fabricated with professional designed equipment to manufacture the foamed mortar at IBR Consult BV in Haelen (Netherlands). Two batches have been made with a weight 139 kg and 132 kg.

The cementitious fluid is poured in moulds. The buffer-like concrete is also vibrated to remove air as much as possible. A plastic foil was added on top of the mould to prevent hydration cracks. After at least one day, hardened samples were removed from the moulds, weighted and put in a water bath for at least 27 days. Some cubical samples with an edge of 5 cm have been sawn from a cubical sample with an edge of 15 cm. The following tables show the concrete recipes for concrete casted in 2015 and 2016. Two types of cement have been used. CEM III/B 42.5 N LH/SR is a blended cement with 66-80 wt% blast furnace slag and 20-34 wt% Portland cement, this blended cement has a Low Hydration heat (LH) and is Sulphate Resistant (SR). The content of Portland cement in CEM I 52.5 N - SR3/NA is 95% to 100% and is sulphate resistant (SR), it contains a smaller tri calcium aluminate content of 3 wt%.

Table 6-2: Mortar recipe for 6 buffer-like samples casted in 30 June 2015[a] and 1 July 2015[b]

Component	Type	[a]kg m^{-3}	[b]kg m^{-3}
Cement	CEM III/B 42.5 N LH/SR [a]	385	421
Water		176	180
Superplasticiser	TM OFT-II B84/39 CON. 35% (BT-SPL)	5	6
Fine aggregate	Quartz sand: 0-4 mm	846	860
Coarse aggregate	Quartz gravel: 2-8 mm	865	848

Density was determined through EN 12350-6:1999: 2277 kg m^{-3} and 2315 kg m^{-3}. Water/cement are 0.46 and 0.43.

Table 6-3: Mortar recipe for backfill samples casted 9 May [a] 2016 and 17 May [b] 2016

Component	Type	[a]kg m^{-3}	Type	[b]kg m^{-3}
Cement	CEM III/B 42.5 N LH/SR [a]	391	CEM I 52.5 N - SR3/NA [b]	417
Water		154		165
Foaming agent	TM 80/23	< 1	TM 80/23	< 1
Fine aggregate	Sand : 0-2 mm	955	Sand : 0-2 mm	1018

Density was determined by the weight of one litre of cementitious fluid: 1500 kg m^{-3} for samples made with CEM III and 1600 kg m^{-3} for samples made with CEM I. Water/cement are 0.40[a,b].

The weight of the samples has also been measured after removal of the samples from the mould after casting for one day. The average density of 56 samples was 1566 ± 136 kg m^{-3} for the samples fabricated with CEM III i.e. a variation in density of 8.7%. The minimum in density was 1390 kg m^{-3} and the maximum in density was 1828 kg m^{-3}. The average density of 56 samples was 1721 ± 170 kg m^{-3} for the samples fabricated with CEM I i.e. a variation in density of 9.9%. The minimum in density was 1462 kg m^{-3} and the maximum in density was 1929 kg m^{-3}.

Table 6-4: Mortar recipe for buffer-like samples casted 13 July 2016

Component	Type	kg m^{-3}
Cement	CEM III/B 42.5 N LH/SR [a]	402
Water		184
Superplasticiser	TM OFT-II B84/39 CON. 35% (BT-SPL)	5
Fine aggregate	Quartz sand: 0-4 mm	827
Coarse aggregate	Quartz gravel: 2-8 mm	866

The average density was determined by the weight of 51 samples after casting for one day and volume of a cubical sample with an edge of 15 cm, 10 cm and 5 cm: 2284 ± 38 kg m^{-3} (μ±σ) i.e. a variation in density of 1.7% The minimum in density was 2188 kg m^{-3} and maximum in density was 2388 kg m^{-3}. Water/cement = 0.46.

Table 6-5: Mortar recipe for backfill samples casted 6, 8 and 9 September 2016

Component	Type	kg m^{-3}
Cement	CEM III/B 42.5 N LH/SR [a]	411
Water		144
Foaming agent	TM 80/23	4
Superplasticiser	TM OFT-II B84/39 CON. 35% (BT-SPL)	5
Fine aggregate	Sand : 0-2 mm	1131

The average density was determined by the weight of 60 samples after casting for one day and volume of a cubical sample with an edge of 15 cm, 10 cm and 5 cm: 1695 ± 35 kg m^{-3} (μ±σ) i.e. a variation in density of 2.1%. The minimum in density was 1634 kg m^{-3} and maximum in density was 1816 kg m^{-3}.Water/cement = 0.35.

6.3 Available characterisation of cementitious materials

6.3.1 Mechanics

6.3.1.1 Compressive strength

The compressive strength has been measured according to EN-12390-3 after 28 days for all the types of cementitious material. These samples have been exposed to Dutch tap water for at least 27 days.

The compressive strength has also been measured after several years of exposure with two different environments for certified buffer-like and backfill material:

- At different relative humidity's at 20°C and 5°C;
- In synthetic clay pore water at around 20°C.

Certified buffer-like material (CEM III)

The recipe for the buffer-like material is described in Table 6-4. Table 6-6 shows that the measured compressive strength of the buffer-like samples is for each sample larger than 45 N/mm^2 - 4 N/mm^2 i.e. 41 N/mm^2 after 28 days. Table 6-6 also shows that the average out of 3 samples is larger than 45 N/mm^2 + 4 N/mm^2 i.e. 49 N/mm^2. Concrete that is manufactured with this quality is so-called certified concrete i.e. the quality of the fabricated concrete is assured.

Table 6-6: Compressive strength and weight of buffer-like materials measured on 9 August 2016 of samples casted on 13 July 2016.

Sample	Cubical edge of sample [cm]	Weight [grams]	Weight increase	Compressive strength [N mm^{-2}]
COV150_9	15	7749.7	0.61%	54.6
COV150_10	15	7744.5	0.72%	53.0
COV150_11	15	7738.2	0.67%	52.0
COV100_17	10	2293.7	0.73%	56.4
COV100_18	10	2281.1	0.65%	55.8
COV100_19	10	2342.8	0.68%	57.5
COV50_49	5	279.516	1.26%	49.5
COV50_50	5	283.178	1.09%	52.3
COV50_51	5	284.551	1.02%	51.8

The weight measured one day after casting is also compared to the weight measured before the measurement of the compressive strength. All samples have a minor increase in weight but the size of the samples matters. The increase in weight is attributed to the uptake of water during the submersion in tap water.

The compressive strength has also been measured from cubical samples with an edge of 5 cm that have been sawn from cubical samples with an edge of 15 cm in order to test whether sawing would have an impact on the measured strength of concrete. The sawn samples have been submerged in tap water for 4.5 months. Figure 6-7 shows that a reduction in strength has not been measured. It was therefore assumed that sawing of samples has no impact on the strength of concrete.

Table 6-7: Compressive strength and weight of sawn buffer-like samples measured on 18 January 2017

Sample	Cubical edge of sample [cm]	Weight [grams]	Compressive strength [N mm^{-2}]
8_COV50_73	5	299.458	59.0
8_COV50_74	5	307.335	53.4
8_COV50_75	5	299.276	61.9

Concrete samples that have been submerged in tap water for 6 months and sawn samples that had been submerged for 4.5 months were exposed to different relative humidity's at 20°C and 5°C. There was more storage volume available for samples exposed to 20°C than 5°C. Consequently, more different relative humidity's have been used for 20°C than for 5°C. The different relative humidity's were made with saturated salt solutions. Figure 6-5 shows the experimental set-up and Table 6-8show the different salts and other materials used to control the relative humidity of air inside the boxes. The plastic boxes (Araven, 1.5 litre) in which the cylinders and samples have been put are made from polypropylene.

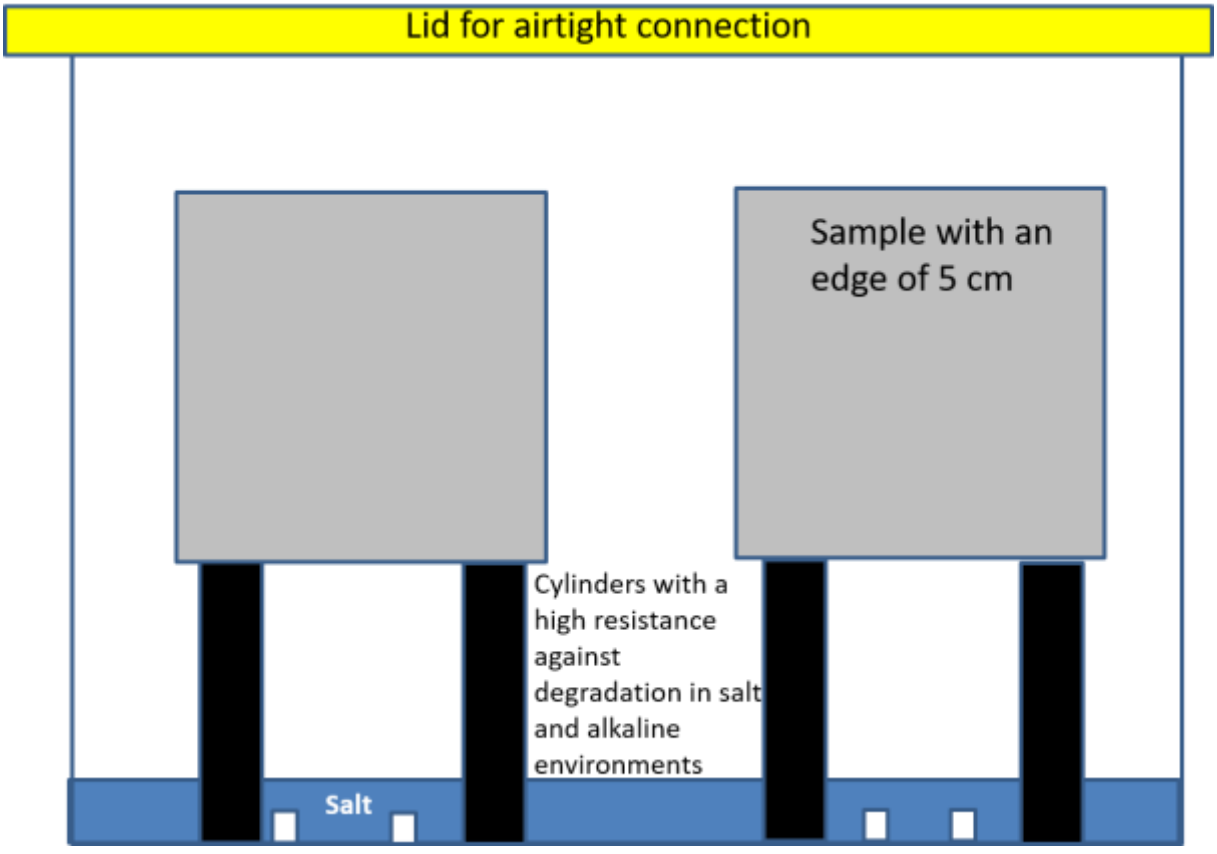

Figure 6-5: Cross section of the experimental set-up for exposure of certified concrete samples to a relative humidity.

Table 6-8: Relative humidity's to which samples have been exposed.

Used materials to control the air in the polypropylene box	Relative humidity at 5ºC	Relative humidity at 20ºC	Source
Submerged in demineralized water	> 100	> 100	
Wet cotton	≈100	≈100	COVRA

$NaOH•H_2O$		6 ± 2	Wexler, 15-32
$KOH•2H_2O$	14 ± 2	10 ± 2	Wexler, 15-32
$LiCl•H_2O$		11.31 ± 0.31	IUPAC, 15-33
$MgCl_2•6H_2O$	33.60 ± 0.28	33.07 ± 0.18	IUPAC, 15-33
K_2CO_3	43.2 ± 0.5	43.1 ± 0.3	ASTM, 15-33
$Mg(NO_3)_2•6H_2O$	58.86 ± 0.43	54.38 ± 0.23	IUPAC, 15-33
NaCl	75.65 ± 0.27	75.47 ± 0.14	IUPAC, 15-33
KCl	87.67 ± 0.45	85.11 ± 0.29	IUPAC, 15-33
K_2SO_4	98.5 ± 0.9	97.6 ± 0.9	ASTM, 15-33

The thermal exposure at 20°C was performed by putting rows of plastic boxes next to one another in a specifically designed temperature controlled closet. Rows of plastic boxes were put next to another in ordinary refrigerator. The temperature in this refrigerator was measured with thermometer (mercury device) in order to be sure that the plastic boxes were exposed to a temperature of 5°C. Sequentially, the weight of the samples has been measured in a laboratory at room temperature. Not always was the salt solution saturated when this measurement in weight was performed. Salt was then added again to the water in order to achieve the requested relative humidity. The plastic boxes were put back again either in the temperature controlled closet or refrigerator.

There can be some precipitation of salt on the surfaces of the cylinder for the part that is not submerged in the salt solution. This precipitation progressively increases in height and can reach the samples. The cylinders were washed to prevent the surface of the samples being contaminated with salt. A constant weight was achieved after about 1000 days of exposure to a relative humidity. Figure 6-6 and Figure 6-7 show the compressive strengths of the cubical samples with an edge of 5 cm as a function of the relative humidity at a temperature of 20°C and 5°C. Closed symbols are results from the only casted samples. Open symbols are results from the casted and sawn samples.

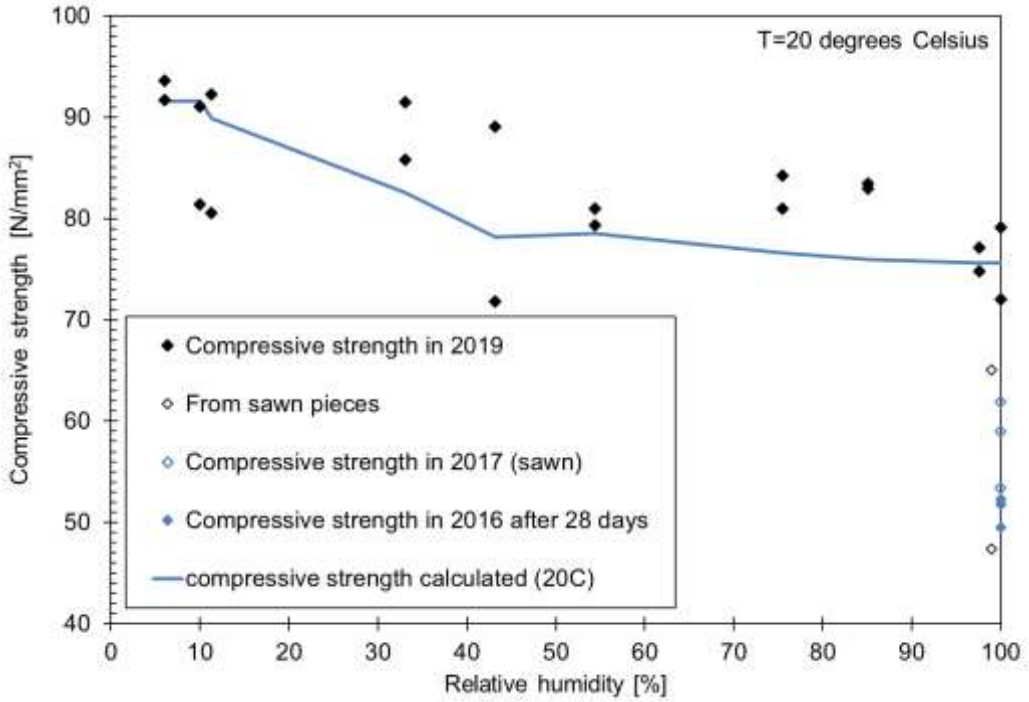

Figure 6-6: Compressive strength of buffer-like material as a function of the relative humidity at 20°C

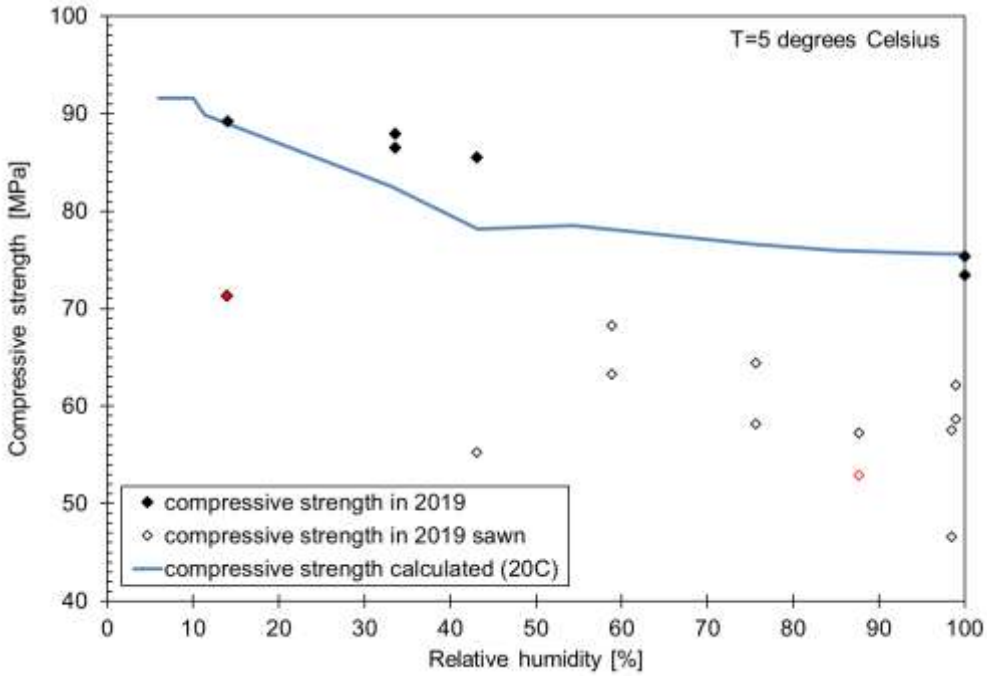

Figure 6-7: Compressive strength of buffer liker material as a function of the relative humidity at 5℃; samples on which salt has been observed on the surface are marked red.

Figure 6-6 clearly shows that the compressive strength increases with decreasing relative humidity. This increase is attributed to the suction pressure of the pores. Pores without water have a capillary pressure, empty pores with a smaller radius have a larger compressive pressure than empty pores with a larger radius. The capillary pressure is a function of the relative humidity as well as a function of the radius of the pore by the Young-Laplace's equation:

$$p_{cap} = \frac{RT}{M_{H_2O} g} \ln \frac{RH}{100} = \frac{\sigma_{g-l}(T)\cos\theta}{r}$$

where R is Boltzmann constant, T is temperature, M_{H2O} is the molar mass of water, g is the gravitational speed at Earth of 9.81 m s^{-2}, σg-l is the surface tension across the pore water gas interface which is 72.74×10^{-3} N/m at 20ºC and 74.94×10^{-3} N/m at 5ºC[1] (Lemmon, 2015), Θ is the contact angle between the water-gas interface and the solid material which is approximately 0 degrees for water-air-concrete. The blue line in Figure 6-6 is determined by the solid part of the sample and the suction pressure of the pores:

$$f = f_{solid} + \sum_{i=1}^{N} p_{cap,i} \times V_i$$

where f_{solid} is the compressive strength without capillary pressure i.e. the compressive strength measured at 100% relative humidity, $p_{cap,i}$ is the capillary pressure of the pores and V_i is the volume of pores that are empty at a specific relative humidity. These volumes are shown in Figure 6-12 for buffer-like material and in Figure 6-15 for the backfill samples.

Some cubical samples with an edge of 5 cm have been made by sawing a cubical sample of 15 cm. Many of these sawn samples have been exposed to a different relative humidity at 5°C. Although it was initially assumed that sawing has no impact on the strength of concrete since the sawn samples in 2017 did not show a reduction in compressive strength, this assumption seems not to hold when sawn samples are measured after a couple of years. Figure 6-7 clearly shows that the sawn samples have a

[1] The value at 5ºC is determined by the average of the surface tension at 4ºC of 75.08 mN/m and 74.80 mN/m at 6ºC.

smaller concrete strength. The compressive strength also increases with a lower relative humidity similarly as measured for the series at 20°C for the only casted samples (solid symbols).

The buffer-like cementitious materials have also been exposed to a synthetic pore solution at around room temperature. Table 6-9 shows that a reduction in compressive strength attributed to the ingress of dissolved magnesium (or other dissolved species) cannot be measured yet after exposure to the synthetic clay pore solution since 6 December 2016 i.e. after more than 4 years.

Table 6-9: Compressive strength of buffer-like samples with an edge of 5 cm exposed at around 20 °C.

Sample	Preparation	Weight [grams]	Compressive strength [N mm^{-2}]	Date of measurement	Exposure medium
COV50_40	Casted	294.808	72.05	5 August 2019	Demineralized water
COV50_41	Casted	292.703	79.16	5 August 2019	
8_COV50_71	Casted and sawn	303.516	47.4	5 August 2019	Air from wet cotton ~100% relative humidity
8_COV50_72	Casted and sawn	299.465	65.1	5 August 2019	
7_COV50_58	Casted and sawn	298.387	54.2	8 January 2021	Synthetic clay pore water
7_COV50_59	Casted and sawn	300.111	63.1	8 January 2021	

Certified backfill material (CEM III)

The recipe for backfill samples is described in Table 6-4. Table 6-10 shows that the measured compressive strength of the backfill samples is for each sample larger than 10 N/mm^2 - 4 N/mm^2 i.e. 6 N/mm^2 after 28 days hardening. Table 6-10 also shows that the average out of 3 samples is larger than 10 N/mm^2 + 4 N/mm^2 i.e. 14 N/mm^2. Concrete that is manufactured with this quality is so-called certified concrete i.e. the quality of the fabricated concrete is assured. The compressive strength was also measured after 14 days hardening in order to monitor the strength of the concrete.

Table 6-10: Compressive strength and weight of certified backfill samples.

Sample	Cubical edge of sample [cm]	Weight [grams]	Weight increase	Compressive strength [N mm^{-2}]	Date in 2016	Days after hardening
HS_1_150	15	5758.7	2.54%	18.5	16 Sep	14
HS_7_150	15	5813.7	4.20%	18.6	3 Oct	27/28
HS_8_150	15	5762.5	3.83%	18.7	3 Oct	27/28
HS_9_150	15	5905.2	2.32%	21.6	3 Oct	27/28
HS_21_100	10	1786.2	2.83%	19.7	16 Sep	14
HS_27_100	10	1759.8	2.37%	23.7	3 Oct	27/28
HS_28_100	10	1844.4	1.56%	26.1	3 Oct	27/28
HS_29_100	10	1778.6	3.42%	21.4	3 Oct	27/28
HS_68_50	5	221.731	4.57%	19.0	3 Oct	27/28
HS_69_50	5	221.465	4.73%	19.8	3 Oct	27/28
HS_70_50	5	221.523	4.71%	20.1	3 Oct	27/28

The weight measured one day after casting is also compared to the weight measured before the measurement of the compressive strength. All samples have a larger increase in weight than the buffer-like samples. Also for these backfill samples, the increase in weight is attributed to the uptake of water during the submersion in tap water but a distinction in size of samples cannot be so clearly be made as for the buffer-like samples.

The compressive strength has also been measured from sawn cubical samples with an edge of 5 cm in order to test whether sawing could have an impact on the measured strength of concrete. The sawn samples have been submerged in tap water for 4 months. A comparison between Table 6-10 and Table 6-11 shows that the sawn samples have a smaller compressive strength but the concrete still satisfies the certification requirement. It was therefore decided to continue with sawn samples.

Table 6-11: Compressive strength and weight of sawn backfill samples measured on 18 January 2017.

Sample	Cubical edge of sample [cm]	Weight [grams]	Compressive strength [N mm^{-2}]
6_HS_87_50	5	200.025	13.1
6_HS_88_50	5	195.552	15.0
6_HS_89_50	5	201.41	17.1

As the samples can be characterised as certified concrete and the variation in density of 2.1% is sufficiently small, these samples can also be used to investigate the impact of the relative humidity on the strength of concrete as for the buffer-like samples. Figure 6-8 and Figure 6-9 show the compressive strengths of the cubical backfill samples with an edge of 5 cm as a function of the relative humidity at a temperature of 20°C and 5°C. Closed symbols are results from backfill samples that are only casted. Open symbols are results from casted and sawn backfill samples.

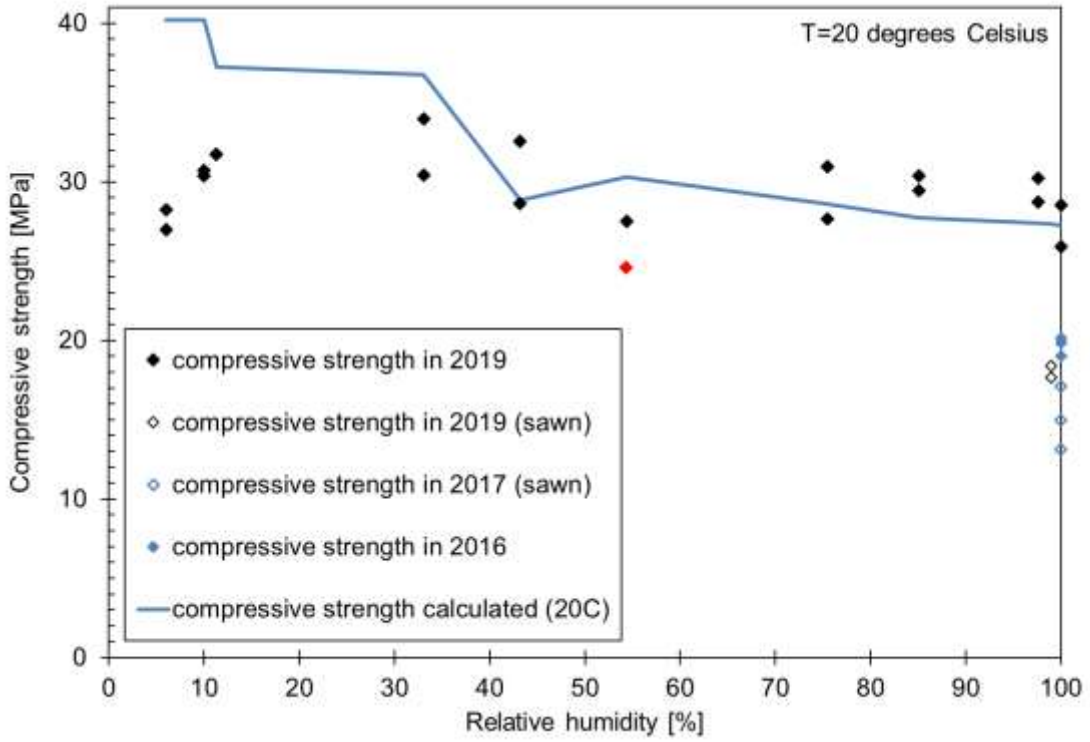

Figure 6-8: Compressive strength of backfill samples as a function of the relative humidity at 20□C. Samples on which salt has been observed on the surface are marked red.

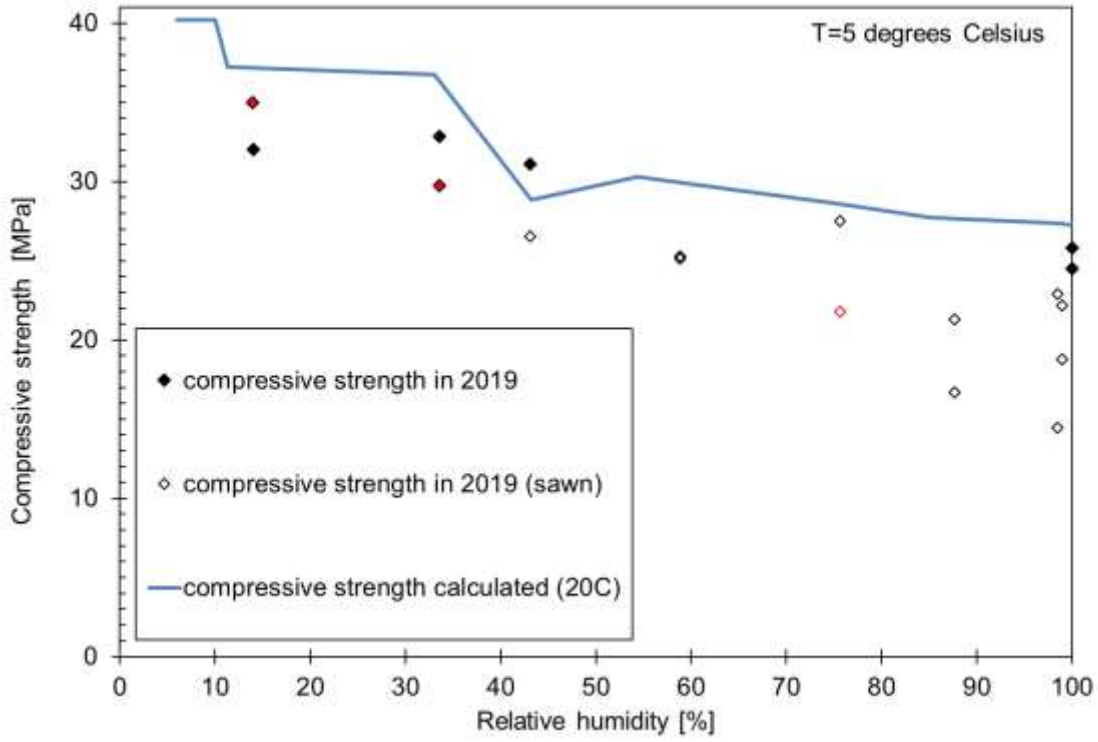

Figure 6-9: Compressive strength of backfill samples as a function of the relative humidity at 5□C. Samples on which salt has been observed on the surface are marked red.

Figure 6-9 clearly shows that the sawn samples have a smaller concrete strength. For the only casted samples (solid symbols), the increase in compressive strength for the backfill samples with a decreasing relative humidity in Figure 6-8 is not as clear as for buffer-like materials measured at 20°C in Figure 6-6. The distribution in size of pores could also not be so clearly determined with the equilibrium content of water (see Figure 6-15) as with buffer-like material (see Figure 6-12).

Results for backfill samples to exposure of the synthetic pore solution (see Table 6-1) are also available. Unlike the buffer-like material, Table 6-12 clearly shows a reduction in strength of the backfill after exposure to this solution after more than 4 years. The ingress of dissolved species such as magnesium into the backfill sample also takes place at a higher rate due to its larger porosity and large size in pores compared to buffer-like material.

Table 6-12: Compressive strength of backfill samples with an edge of 5 cm exposed at around 20 ℃.

Sample	Preparation	Weight [grams]	Compressive strength [N mm^{-2}]	Date of measurement	Exposure medium
HS_59_50	Casted	229.164	25.9	22 July 2019	Demineralized water
HS_60_50	Casted	229.573	28.5	22 July 2019	
6_HS_91_50	Casted and sawn	204.171	18.4	22 July 2019	Air from wet cotton ~100% relative humidity
6_HS_92_50	Casted and sawn	202.157	17.7	22 July 2019	
5_HS_79_50	Casted and sawn	212.195	13.2	8 January 2021	Synthetic clay pore water
5_HS_80_50	Casted and sawn	216.208	13.0	8 January 2021	

Not-certified backfill material (CEM I and CEM III)

The recipes for these backfill samples are presented in Table 6-3. After 28 days hardening, the measured compressive strength of backfill samples is for each sample larger than 10 N/mm^2 - 4 N/mm^2 i.e. 6 N/mm^2. Table 6-13 also shows that the average out of 3 samples is smaller than 10 N/mm^2 + 4 N/mm^2 i.e. 14 N/mm^2. Three cubical samples with an edge of 15 cm have also been measured at another

company to check COVRA's results. The measured compressive strength is similar. Consequently, the reason that the fabricated samples do not satisfy the required strength in concrete is not due to COVRA's press or working methodology. The compressive strength has also been measured a week later i.e. 36 days of hardening but the outcome remains the same: the samples do not satisfy the set requirements in strength.

Table 6-13: Compressive strength and weight of backfill CEM III samples casted on 9 May 2016.

Sample	Cubical edge of sample [cm]	Weight [grams]	Weight increase	Compressive strength [N mm^{-2}]	Date in 2016	Measured at
H-S150_3	15			9.0	7 June	KOAC
H-S150_4	15			7.5	7 June	KOAC
H-S150_5	15			7.7	7 June	KOAC
H-S150_9	15	5121.8	1.80%	8.4	6 June	COVRA
H-S150_10	15	4906.4	2.14%	6.7	6 June	COVRA
H-S150_11	15	5243.4	1.86%	8.4	6 June	COVRA
H-S100_17	10	1710.63	2.62%	8.2	6 June	COVRA
H-S100_18	10	1761.88	2.15%	10.5	6 June	COVRA
H-S100_19	10	1681.74	2.64%	8.7	6 June	COVRA
H-S50_41	5	186.28	6.09%	6.5*	6 June	COVRA
H-S50_42	5	185.78	6.16%	6.7*	6 June	COVRA
H-S50_43	5	186.68	5.11%	6.8*	6 June	COVRA
H-S50_49	5	184.8	5.67%	6.6*	14 June	COVRA
H-S50_50	5	184.38	6.05%	5.5*	14 June	COVRA
H-S50_51	5	183.29	5.51%	6.7*	14 June	COVRA

*Measurement was outside the range for calibration of the press

For the samples fabricated with CEM I, a different image than for CEM III arises from the compressive strength measurements. These measurements in Table 6-14 follow the requirements in strength for cubical samples with an edge of 15 cm and 10 cm, but not for the samples with an cubical edge of 5 cm. A week later, the measurement in compressive strength was repeated for other cubical samples with an edge of 5 cm. The required strength is obtained for these measurements. The weight of these samples is also significantly larger than the samples from which the compressive strength was measured a week earlier. It is therefore assumed that the large variation in density of the samples contributed to the large variation in measured strength. This variation in density of 9.9% is envisaged to be too large to observe trends in a range of samples that have been exposed to different relative humidity's.

Table 6-14: Compressive strength and weight of backfill CEM I samples casted on 17 May 2016.

Sample	Cubical edge of sample [cm]	Weight [grams]	Weight increase*	Compressive strength [N mm^{-2}]	Date in 2016
P-S150_9	15	6235.4	1.64%	15.6	14 June
P-S150_10	15	5419.8	1.81%	10.4	14 June
P-S150_11	15	5244.9	1.87%	8.4	14 June
P-S100_17	10	1868.4	1.91%	16.8	14 June
P-S100_18	10	1892.89	1.84%	19.1	14 June
P-S100_19	10	1923.71	1.84%	19.9	14 June
P-S50_46	5	197.782	4.03%	7.5	14 June
P-S50_47	5	200.508	4.07%	8.5	14 June
P-S50_48	5	195.901	4.17%	8.2	14 June
P-S50_49	5	193.48	4.15%	7.9	14 June
P-S50_50	5	190.93	4.45%	8.1	14 June
P-S50_51	5	192.02	4.07%	8.2	14 June
P-S50_23	5	238.854	2.73%	24.9	21 June
P-S50_24	5	243.582	2.09%	26.4	21 June
P-S50_25	5	247.035	2.81%	27.3	21 June

*casted samples were removed from their moulds almost after one week instead of one day as for the other samples.

6.3.1.2 Young's modulus

There are empirical relationships available between the compressive strength and Young's modulus. In NEN 6720 from 1995 (read in (Betonpocket, 2009)) this empirical relationship was for a characteristic cubical compressive strength between 15 and 65 N mm^{-2}: 22250 + 250×f'_{ck} (in N mm^{-2}) For example, concrete with a characteristic compressive strength of 45 Nmm^{-2} would have a Young's modulus of 33.5 GPa. This empirical relationship has been later revised into $22\times(f_{cm}\div10)^{0.3}$ where f_{cm} is the average cylindrical compressive strength (Betonpocket, 2019).

6.3.1.3 Porosity

Buffer-like material

The porosity has been gravimetrically determined. The range in relative humidities for the series at 20°C was from 6% till more than 98%. The smallest relative humidity was obtained with a saturated NaOH solution. So far, we have not been familiar with the use of a saturated NaOH solution to obtain a relative humidity. No increase in weight has been observed for the only casted samples exposed to the highest relative humidity. It is therefore assumed that the samples were fully saturated at the start of the exposure to a relative humidity. A relative humidity of 6% is so small that any water in a pore with a radius larger than 0.19 nm would be evaporated. It is therefore assumed that there is no water in the pores in these samples at such a small relative humidity. Figure 6-10 shows the loss of water per cubical volume of a buffer-like sample assuming a density of water of 1000 kg m^{-3}. Closed symbols are results from buffer-like samples that have been permanently exposed to the relative humidity i.e. there was always salt observed in the liquid. Open symbols may not always been exposed to a relative humidity i.e. the salt was completely dissolved by which it is assumed that the salt solution has become unsaturated. A porosity of 13% can be deduced from the difference between the highest and smallest loss in water.

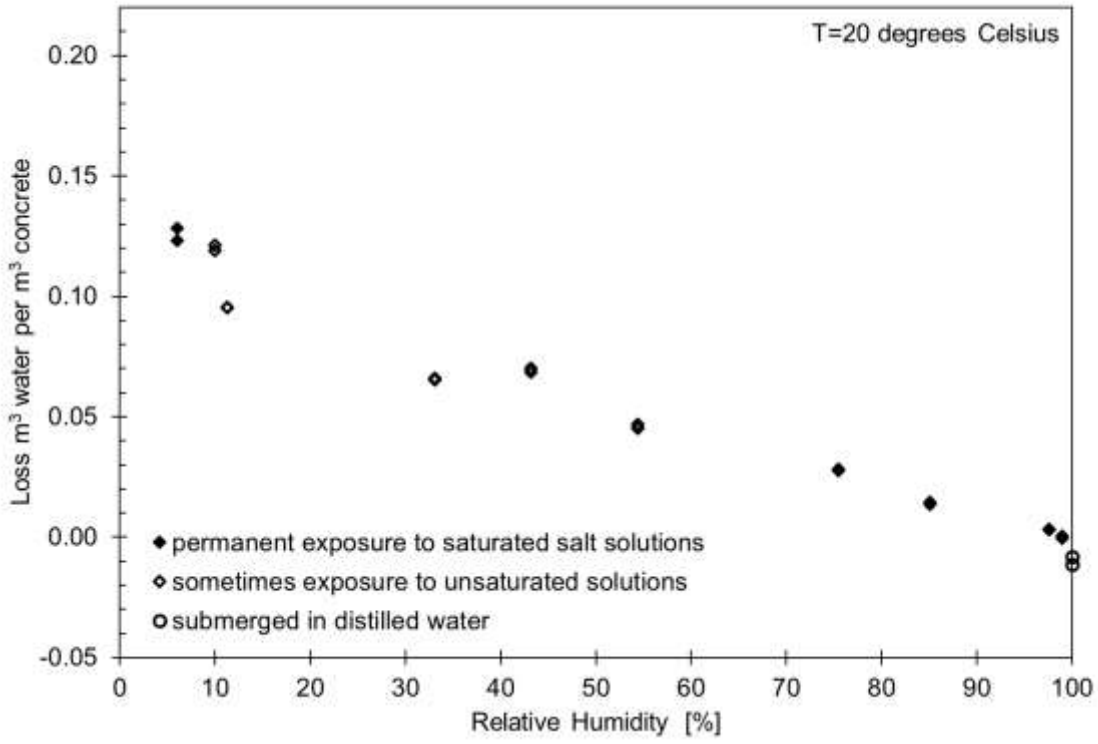

Figure 6-10: Total loss of water after achieving a constant in weight as a function of the relative humidity at 20℃ for buffer-like material.

The same exercise has been performed for the samples exposed at 5°C except that the smallest possible relative humidity was not used because it was not familiar to us that saturated NaOH solutions can be used to obtain such a small relative humidity. Figure 6-11 shows the loss of water per cubical volume of a buffer-like sample assuming a density of water of 1000 kg m^{-3}. The determination of the porosity with the series at 5°C can be underestimated with the lack of a result obtained with a saturated NaOH solution. Closed symbols are results from buffer-like samples that have been permanently exposed to the relative humidity i.e. there was always salt observed in the liquid. Open symbols may not always been exposed to a relative humidity i.e. it was observed before the measurement in weight the salt was completely dissolved by which it is assumed that the salt solution has become unsaturated. After the measurement in weight, salt has been added to obtain again saturated salt solution.

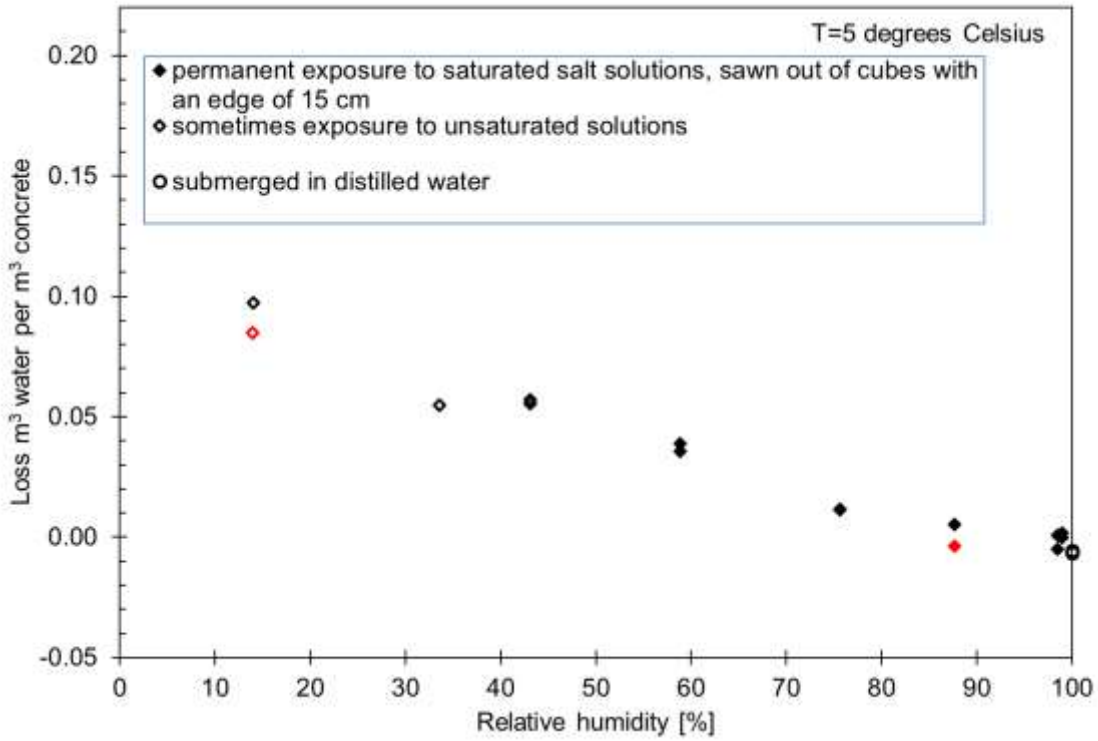

Figure 6-11: Total loss of water after achieving a constant in weight as a function of the relative humidity at 5℃ for buffer-like material.

The distribution in size of pores can be determined from the equilibrium water content as a function of the relative humidity. Figure 6-12 shows that although the number of different relative humidities is smaller for the series performed at 5°C than at 20°C, the same predominance in the size of the pores can be observed.

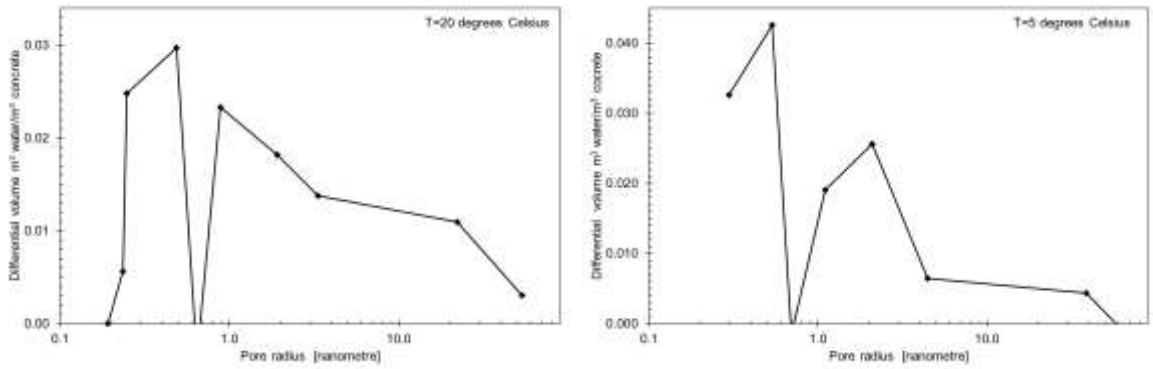

Figure 6-12: Distribution in size of pores determined at 20℃ and 5℃ for buffer-like material.

Backfill material

Also backfill samples fabricated with CEM III and superplasticiser were exposed to a range of relative humidity's at 20°C and 5°C. Figure 6-13 and Figure 6-14 show the loss of water per cubical volume for backfill samples assuming a density of water of 1000 kg m^{-3} at the two different temperatures.

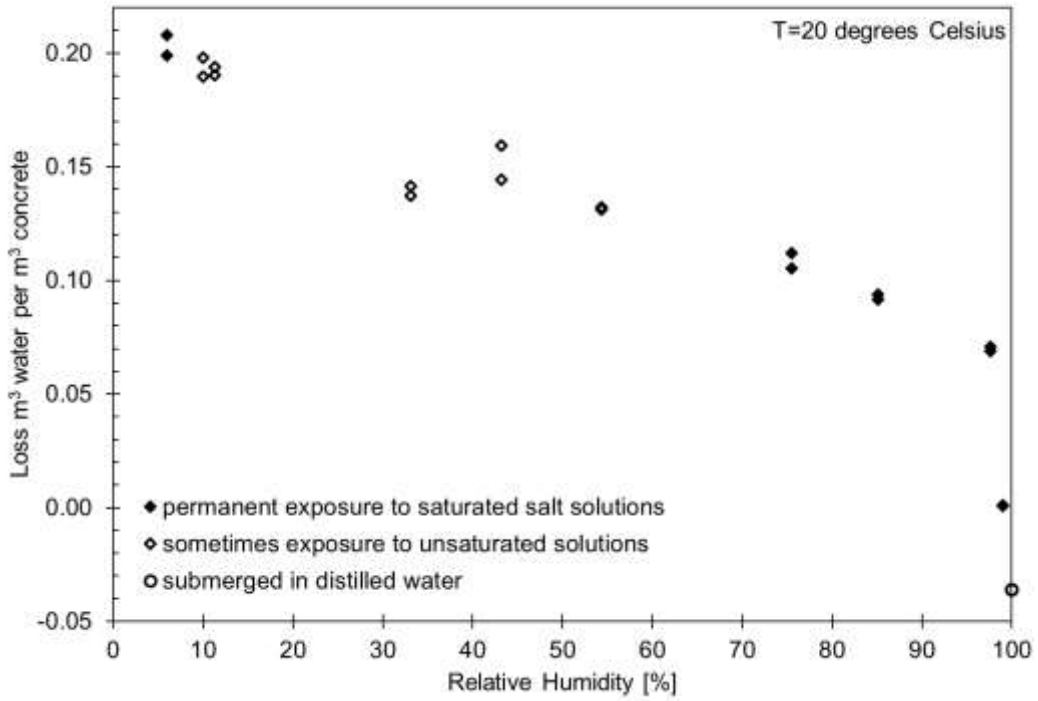

Figure 6-13: Total loss of water after achieving a constant in weight as a function of the relative humidity at 20℃ for the backfill.

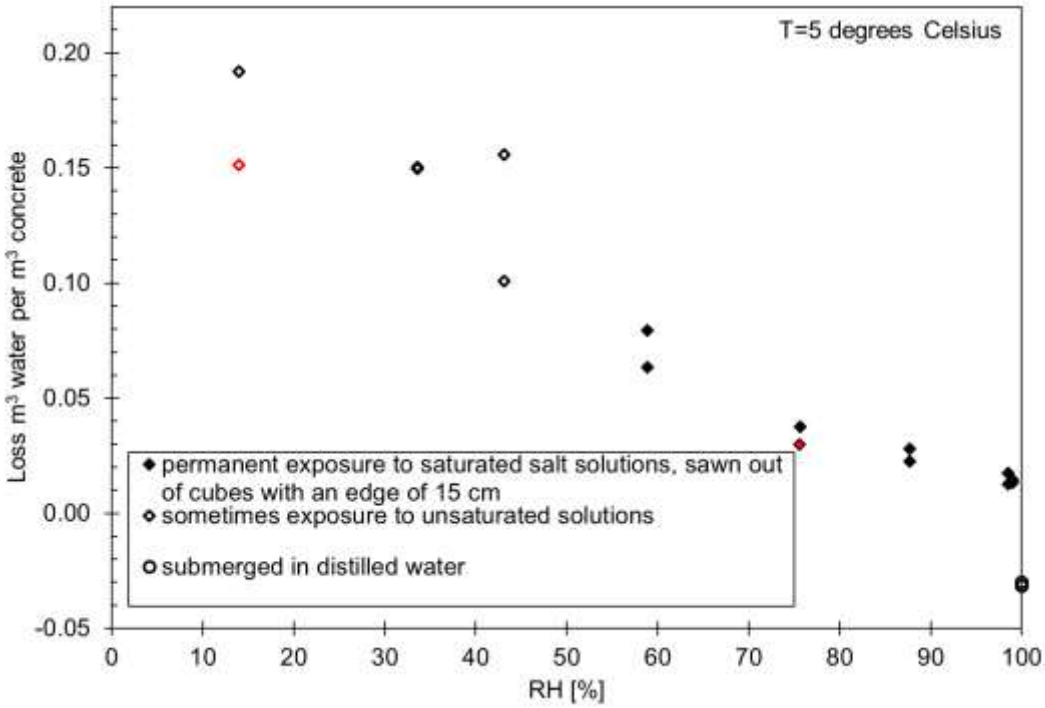

Figure 6-14: Total loss of water after achieving a constant in weight as a function of the relative humidity at 5℃ for the backfill.

Closed symbols are results from backfill samples that have been permanently exposed to the relative humidity i.e. there was always salt observed in the liquid. Open symbols may not always been exposed to a relative humidity i.e. the salt was completely dissolved by which it is assumed that the salt solution has become unsaturated. A porosity of 21% can be deduced from the difference between the highest and smallest loss in water at 20°C.

The difference in loss in weight between a relative humidity of almost 100% and submerged samples at both temperatures is for the backfill samples more significant than for buffer-like material. This is here excluded in the (diffusional) porosity. Like for the buffer-like material, also the distribution in size of pores can be determined from the equilibrium water content as a function of the relative humidity. Figure 6-15 shows a difference in the predominance in size of the pores between 5°C and 20°C.

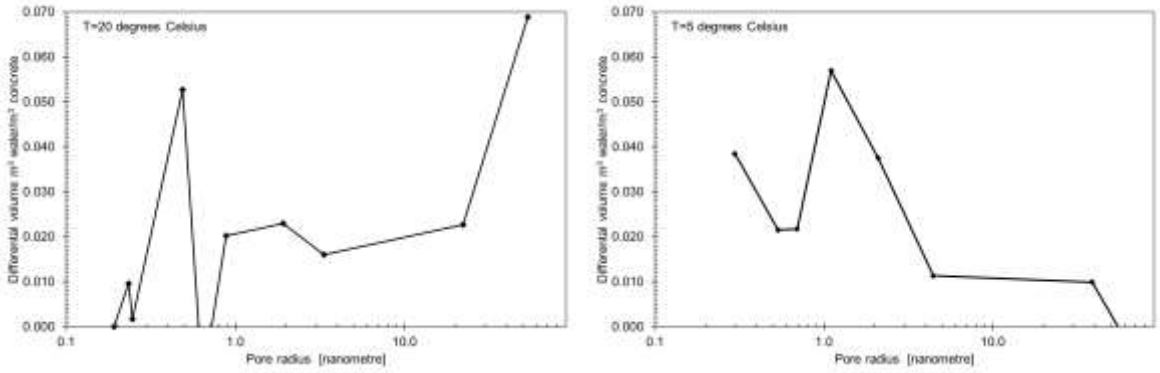

Figure 6-15: Distribution in size of pores determined at 20℃ and 5℃ for backfill.

6.3.1.4 Genuchten parameters and saturation degree

The equilibrium content of water as a function of the relative humidity can also be fitted into so-called Genuchten parameters to obtain a moisture storage function (van Genuchten, 1980). A fit by the eye, especially for the experimental results that have been obtained from samples that have been exposed to air made with permanently saturated solutions, was used to obtain these parameters. Figure 6-16 shows these fits and Table 6-15 the parameters to obtain these fits.

Table 6-15: Genuchten parameters determined with a best fit by the eye

Type of concrete	Porosity [vol%]	n	α (20°C) [m^{-1}]	α (5°C) [m^{-1}]
Buffer-like material	13	2	2×10^{-4}	1.5×10^{-4}
Backfill	21	1.7	8×10^{-4}	2×10^{-4} (3×10^{-4})

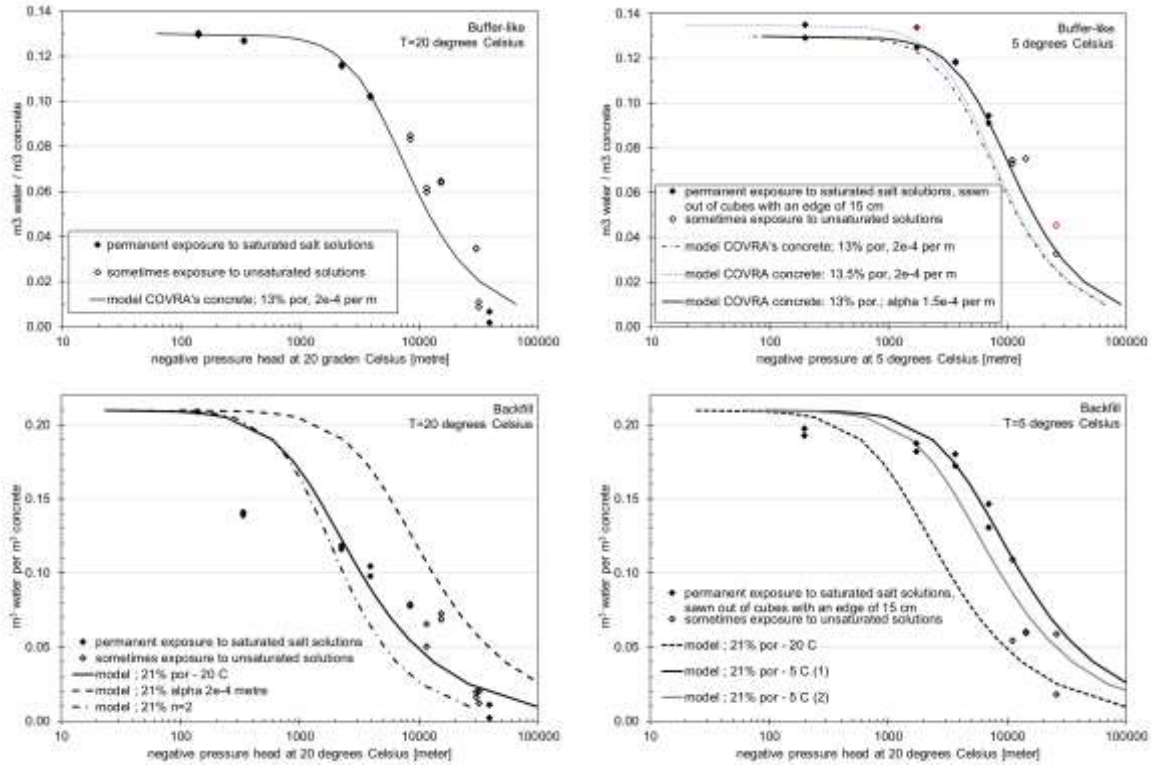

Figure 6-16: Determination of the Genuchten parameters for the buffer-like material and backfill assuming a residual water content of zero.

The porosity and the Genuchten parameter n have been taken to be independent of temperature. The so-called alpha-parameter is a kind of suction force. Suction forces are temperature dependent and for the buffer-like material it clear that a smaller α is needed in order to obtain a better fit with the data. This moisture storage function can also be expressed as a function of the saturation degree. Figure 6-17 shows that the saturation degree for the backfill mortar is clearly smaller than for the buffer-like material. The reason for this difference is attributed to the large size in pores for the backfill compared to the buffer-like material.

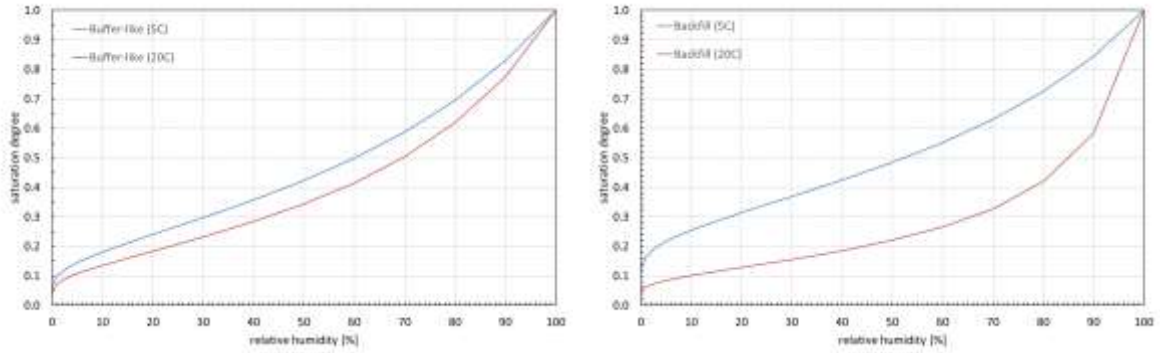

Figure 6-17: Saturation degree with the Genuchten parameters.

6.3.2 Chemistry

6.3.2.1 Mineralogy

There is literature available about the mineralogy of cement paste made with the two types of cement used for the fabrication of the samples i.e. CEM I and CEM III. The measured portlandite was 32 wt% for cement paste fabricated with CEM I and 10 wt% for cement paste fabricated with CEM III. Crystalline CSH phases have not been detected and Rietveld analysis was needed (Kempl and Copuroglu, 2015).

An educated guess for the other minerals can also be made with information from literature and oxide content of cement (Neall, 1994). Table 6-16 shows the compositions of oxides as reported by the cement industry (CCM, 2016) (HCM, 2020) and

Table 6-17 shows the 'guessed' mineralogical composition.

Table 6-16: Average oxide compositions of the two types of cement in wt%.

Cement type	CaO	SiO_2	Al_2O_3	MgO	Fe_2O_3	SO_3	Na_2O	K_2O
CEM I 52.5 N SR3 LA	63.5	21.3	3.5	2.0	4.3	2.6	0.10	0.63
CEM III/B 42.5 N LH/SR LA	48	29	9.9	6.0	1.3	2.4	0.29	0.61

Table 6-17: Mineralogical composition from average oxide compositions.

Mineral	Chemical formula	Molar weight [gram/mol]	Mineralogical composition in wt%	
			CEM I	CEM III/B
Portlandite	$Ca(OH)_2$	74.1	18	5
CSH-gel	C1.8SH1.8	193	55	0
Low Ca-CSH gel	C1.1SH1.1	154	0	56
Hydrotalcite	$Mg_4Al_2O_7•10H_2O$	443	4	13
Hydrogarnet	$(CaO)_3Al_2O_3•3H_2O$	378	5	16
Fe-hydrogarnet	$(CaO)_3Fe_2O_3•3H_2O$	436	9	3
Ettringite	$Ca_6Al_2(SO_3)_4(OH)_{12}•26H_2O$	1254	8	7
Pyrite	FeS_2	120	0	0.20

The calculated portlandite from the average oxide compositions is smaller than measured by (Kempl and Copuroglu, 2015) in order to accommodate the silicon content in the CSH gels. Ettringite is controlled by the added amount of gypsum, hydrotalcite is controlled by the available magnesium (Neall, 1994) and the left-over for iron and aluminium control the amount of hydrogarnets. These phases have been calculated e.g. (Höglund, 2014) and (Neall, 1994). A CSH-gel and a low Ca-CSH gel have been used earlier (Neall, 1994) and in the following table the CSH gels: C1.8SH and C1.1SH (Höglund, 2014) are used. The concentration of minerals with the cement and water content used for the fabrication of the samples is shown in Table 6-18.

Table 6-18: Assumed concentrations of minerals in the samples after 28 days.

Type of sample	Buffer-like	Backfill (certified)	Backfill (CEM III)	Backfill (CEM I)
Cement + water content [kg m^{-3}]	586	555	545	582
Minerals [mol m^{-3}]				
Portlandite	360.9	341.8	335.6	1417.7
CSH-gel	11.3	10.7	10.5	1648.0
Low Ca-CSH gel	2142.4	2029.0	1992.5	0.0
Hydrotalcite	166.1	157.3	154.5	57.7
Hydrogarnet	250.4	237.1	232.8	93.0
Fe-hydrogarnet	36.4	34.4	33.8	125.3
Ettringite	33.4	31.7	31.1	37.7
Pyrite	9.6	9.1	8.9	0.0

6.3.2.2 Pore water chemistry in cement paste

The pH of the concrete pore water depends on the presence of portlandite ($Ca(OH)_2$) i.e. a pH > 12.5 is possible if this cement mineral is present. This presence is measured using X-ray diffraction in CEM I as well as CEM III/B (Kempl and Copuroglu, 2015) although the calcium to silicium ratio in CEM III/B is smaller than 3. Table 6-19 shows the measured pore water chemistries from cement pastes by which the pore solutions were gained by a high-pressure apparatus and the main element concentrations were

measured using ICP-OES (Kempl and Copuroglu, 2015). The pore solutions obtained with a high-pressure apparatus seem to approximate best the pore water chemistries (Atkins et al., 1991) and therefore other techniques to obtain pore solutions such as crushing hardened cement paste and let the crushed paste come into contact with water are not included.

Table 6-19: Measured pore water chemistries for mortar or paste fabricated with CEM I and CEM III from (Kempl and Copuroglu, 2015)

Parameter	Unit	CEM-I	CEM-III/B
		Measured	Measured
Temperature	ºC	RT	RT
pH	-log(H^+)	13.1	13.0
Na^+	mmol/kg	99.0	70.9
K^+	mmol/kg	68.1	39.8
Ca^{2+}	mmol/kg	2.1	2.8
Mg^{2+}	mmol/kg	0.02	0.02
SO_4^{2-}	mmol/kg	0.5	1.7

6.3.2.3 Gaseous carbonation as a function of the relative humidity and porosity

The cubical samples have been split after the measurement of the compressive strength. Each fractured surface was sprayed with a phenolphthalein solution according to EN-14630. The aim was to take a photograph within 30 seconds but within 60 seconds was always achieved. The colourless rims in Figure 6-18 and Figure 6-19 are the so-called carbonated zones i.e. the pH of the concrete pore water is smaller than 8.2.

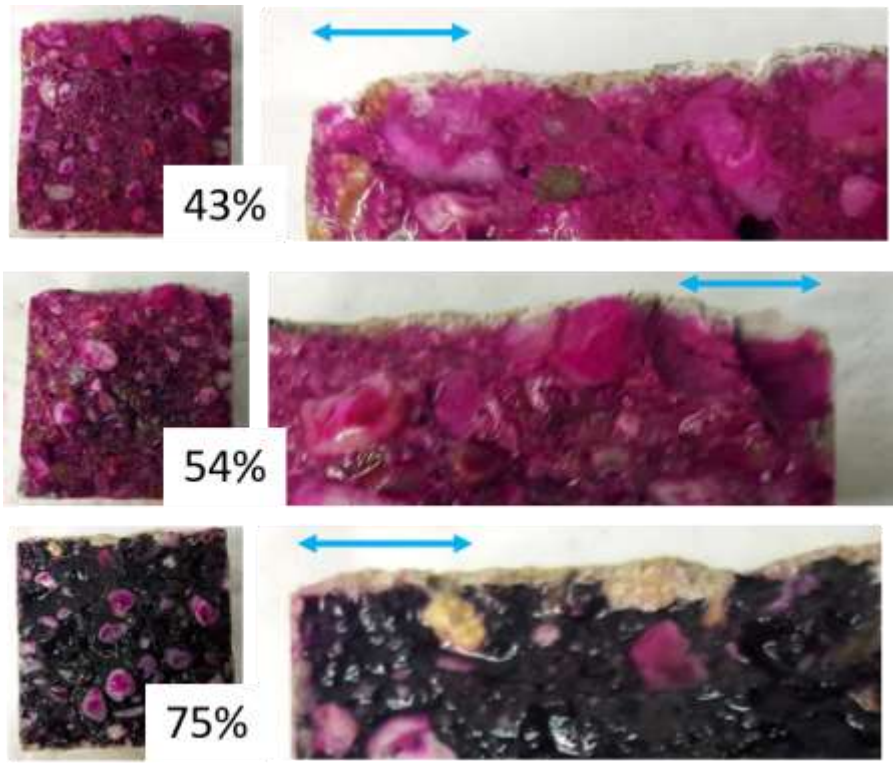

Figure 6-18: Carbonation rims at 20℃ for buffer-like material after 1000 days exposure to a relative humidity of cubical samples with an edge of 5 cm, blue arrow is 1 cm.

The plastic boxes have been made from propylene. Propylene has a relative high permeability for CO2 (Huldy, 1967) and carbonation of the cubical samples during exposure to a relative humidity could not be prevented. The alteration rate for the concrete buffer by gaseous carbonation is extremely slow due to its fabricated engineered impermeability as well as the initial saturation of the sample. Only one clear

rim of only casted buffer-like samples can be observed while the backfill samples show larger rims surrounding the whole sample. It is further investigated whether around every sample of buffer-like material only one clear rim can be seen, including sawn samples. Also the determination of quantitative impact of the initial saturation of the samples to gaseous carbonation is in progress. These investigations are part of COVRA's contribution to the Work Package 2 ACED (Task 3) in the EURAD project. The higher alteration rate for the backfill samples is due to its higher porosity and larger size in pores. The carbonation rims for both types of mortar are so small that it is preliminary assumed that gaseous carbonation had a negligible impact on the strength of concrete as measured as a function of the relative humidity. More detailed analysis of the reaction fronts is needed to confirm this assumption

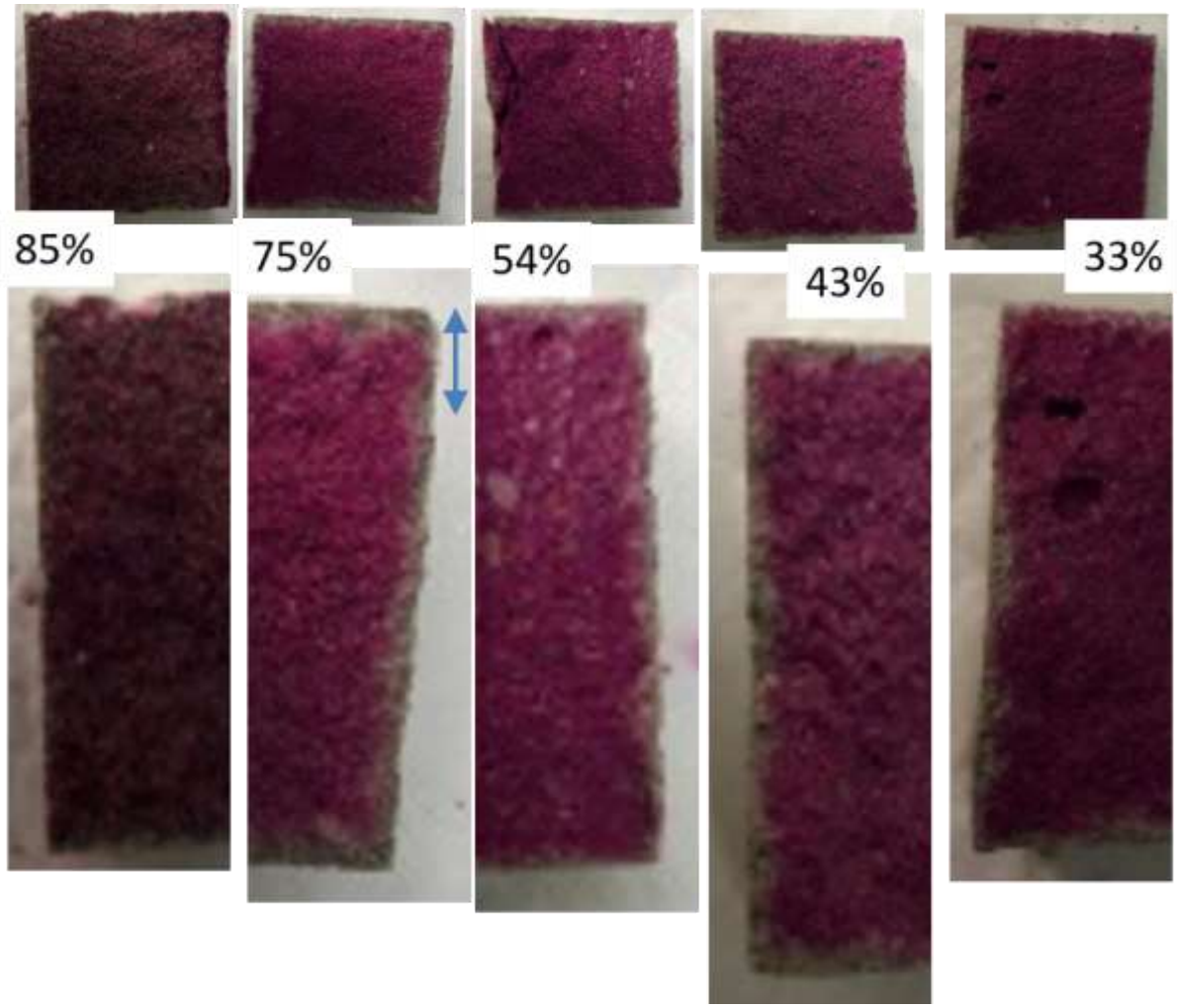

Figure 6-19: Carbonation rims at 20℃ for (certified) backfill after 1000 days exposure to a relative humidity of cubical samples with an edge of 5 cm, blue arrow is 1 cm.

6.3.2.4 Gaseous oxidation as a function of the relative humidity and porosity

Concrete made with a cement blended with blast furnace slag contains initially pyrite in trace amounts. The certified buffer-like material and backfill samples are made with such a blended cement. Propylene has also a relative high permeability for O2 (Huldy, 1967) and oxidation of the cubical samples during exposure to a relative humidity could not be prevented. Fractured surfaces of oxidized concrete are light-grey. These surfaces are dark blue when oxidation was too limited. Figure 6-20, Figure 6-21 and Figure 6-22 clearly show that the extent of oxidation depends on the relative humidity to which the samples have been exposed i.e. exposure to a lower relative humidity results in a larger extent of oxidation.

Figure 6-20: Oxidation at 20℃ for buffer-like material after 1000 days exposure to a relative humidity of cubical samples with an edge of 5 cm.

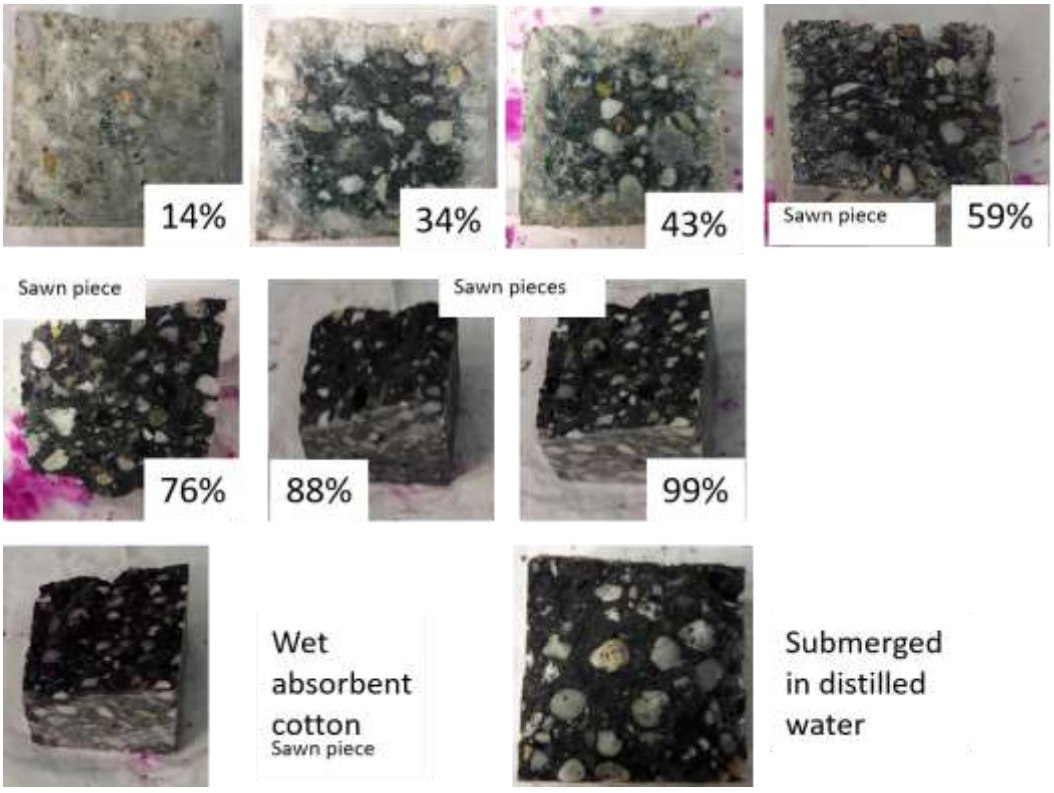

Figure 6-21: Oxidation at 5℃ for buffer-like material after 1000 days exposure to a relative humidity of cubical samples with an edge of 5 cm.

Figure 6-22: Oxidation at 20℃ for backfill after 1000 days exposure to a relative humidity of cubical samples with an edge of 5 cm.

The extent of oxidation is also temperature-dependent i.e. the extent of oxidation of the samples for the buffer-like material exposed at 20°C (Figure 6-20) is larger than these samples exposed at 5°C (Figure 6-21). The extent of oxidation also depends on the porosity i.e. the extent of oxidation of the backfill samples exposed at 20°C (Figure 6-22) is larger than for the buffer-like material exposed at 20°C (Figure 6-20). This set of data is well for model validation and this validation is in progress. A similar model as modelling gaseous carbonation is used except that with the carbonation reaction with cementitious minerals also water is produced while no water is produced in the oxidation reaction with pyrite.

6.3.2.5 Wet oxidation

The previous paragraph showed that gaseous oxidation of samples submerged in distilled water for 1000 days is not visible. This lack of oxidation is also observed after a longer period. Samples fabricated with CEM III exposed to the solution as saline as seawater have also been fractured. These fractured surfaces have been photographed. Figure 6-23 shows that no oxidation can be observed for buffer-like material and for the backfill sample some light spots can be observed at the corners.

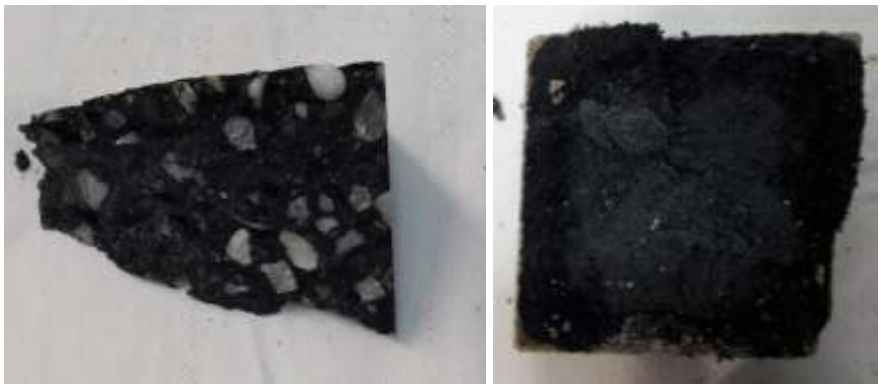

Figure 6-23: Fractured surfaces of a cubical samples with an edge of 5 cm, buffer-like material (left), backfill sample (right). Samples exposed for 4.5 years to a synthetic clay pore water solution.

6.4 Description of experimental set-up

Samples in MAGIC will be continued to be exposed to the synthetic clay pore solution shown in Table 1 1. These samples are currently exposed to this solution in large boxes (Mladenovic et al., 2019) and only cubical samples with an edge of 5 cm will continue this exposure in 1.5 litre plastic boxes.

6.5 Characterisation of cementitious material to be performed in MAGIC

The chemo-mechanical evolution of concrete can be influenced by microbial activity, e.g. by increased precipitation of secondary mineral phases and consequent alteration and dissolution of cement minerals. The presence of cracks increases the possibility of microbial activity in the concrete system, in which the size of the pores determines if microbial life could occur. In case that microbial life is present, the self-sealing of concrete by precipitation of minerals such as calcite can then be enhanced. In concretes with pores of a diameter that is larger than about 0.2 µm, e.g. some type of porous mortars, the microbial activity is not restricted by pore space. The three types of backfill samples may have microbial activity within the bulk of the sample and can thus induce a change in the chemo-mechanical bulk properties. Concrete was made with OPC cement (CEM I) as well as OPC blended with slag (CEM III). The CEM I backfill samples lack redox sensitive species and are therefore slightly oxidizing after manufacturing. The CEM III backfill samples contain pyrite and is therefore reducing when exposed to the synthetic pore solutions. Concrete with an oxidizing and reducing signature is included in order to test the influence of aerobic and anaerobic microbial activity. Fractured surfaces of cracked samples have been put into close contact in order to study self-healing of concrete.

6.5.1.1 Compressive strength

The compressive strength will be measured of all cubical samples with an edge of 15 cm and 10 cm at the beginning of MAGIC. This strength will also be measured for some cubical samples with an edge 5 cm and this strength will also be measured by irradiated samples if needed. The necessity for irradiation will be determined by a microbial analysis of the pore solution with samples. The strength of non-cracked as well as cracked samples with and without microbial activity will be measured near the end of MAGIC.

6.5.1.2 Porosity

The microstructure of polished sawn sections of the cubical samples will be investigated with Scanning Electron Microscopy (SEM).

6.5.2 Chemistry

6.5.2.1 Mineralogy

Sections near the outer surfaces of the samples will be pulverized under air controlled conditions and the mineralogy will be measured using X-ray diffraction (XRD) combined with Rietveld analysis. Also Thermal Gravimetric Analysis Differential Scanning Calorimetry (TGA-DSC) will be used to identify minerals. Analysis of the certified backfill and buffer-like materials become available in the beginning of MAGIC.

6.5.2.2 pH

The carbonated rims of fractured surfaces are measured by spraying with a phenolphthalein solution. It is expected that only rims with backfill samples fabricated with CEM I can be observed since the fractured surfaces are light grey and not dark blue as expected for CEM III. These rims will be measured in the beginning and near the end of MAGIC.

6.5.2.3 Elemental analysis

The distribution of elements as a function of space will be observed from polished surfaces of samples with Energy Dispersive Spectroscopy (EDS). This analysis is combined with SEM. Also X-ray

fluorescence spectrometry (XRF) will be used. Solutions of dissolved pulverised sections of the cubical samples from which aggregates are removed will be analysed with Inductively Coupled Plasma Optical Emission Spectrometry (ICP-OES). This analysis is used to study the ingress of species as well as the egress of species.

6.5.3 Microbiology

A microbial analysis on the exposing solution will be performed in the beginning of MAGIC. To this end, a combination of flow cytometry, intracellular ATP measurements and cultivation will be performed to estimate the total number of cells, microbial activity and viability, respectively. If the samples harbour a microbial community, irradiation at the BR2 facility at SCK CEN will be carried out to obtain sterile controls. Microbes will be added to the solutions if the solution initially appears to be sterile.

The same techniques will be used to investigate the present microbial community near the end of MAGIC. Furthermore, sequencing technologies will be used to identify the present microbial communities. Moreover, SEM/EDX & fluorescence microscopy will be used to visualize and analyse putative biofilms on the samples.

6.6 References

AREVA. (2007) Specification for standard vitrified waste residue (CSD-v) with high actinide content produced at la Hague In AREVA, Ed, p. 23, (Confidential document not published openly).

Atkins, M., Beckley, N., Carson, S., Cowie, J., Glasser, F.P., Kindness, A., Macphee, D., Pointer, C., Rahman, A., Jappy, J.G., Evans, P.A., McHugh, G., Natingley, N.J., and Wilding, C. (1991) Medium-active waste form characterization: the performance of cementbased systems Task 3 Characterization of radioactive waste forms A series of final reports (1985-1989) No 1. 164 p.

Atkinson, A., Goult, D.J., and Hearne, J.A. (1985) An assessment of the long-term durability of concrete in radioactive waste repositories. Mat. Res. Soc. Symp. Proc., 50.

Betonpocket. (2009) Betonpocket 2010. Dutch companies with the HeidelbergCement Group.

Betonpocket. (2019) Betonpocket 2020. Betonhuis.

CCM. (2016) CEM I 52.5 N SR3 LA. Cibelcor, Belgian company.

CUR. (1995) Werken met schuimbeton, Eigenschappen en toepassingen. In C.C.U.R.e.R. (CUR), Ed, p. 104.

Greneche, D., Quiniou, B., Boucher, L., Delpech, M., Gonzalez, E., Alvarez, F., Cunado, M.A., Serrano, G., Cormnezana, J.L., Kuckshinrichs, W., Odoj, R., von Lensa, W., Wallenius, J., Westlén, D., Zimmerman, C. and Marivoet, J. 2007 RED-IMPACT Impact of Partitioning, Transmutation and Waste Reduction Technologies on the Final Nuclear Waste Disposal - Synthesis report, Schriften des Forschungszentrums Jülich - Reihe Energie & Umwelt / Energy & Environment Band - Band / Volume 15 http://www.fz-juelich.de/zb/juwel.

Harris, A.W., Atkinson, A., and Claisse, P.A. (1993) Transport of gases through concrete barriers. Task 3 Characterization of radioactive waste forms - A series of final reports, Luxembourg.

HCM. (2020) Technische Fiche CEM III/B 42.5 LH/SR. Hollandse Cement Maatschappij (Dutch company)

Höglund, L.O. (2014) The impact of concrete degradation on the BMA barrier functions. In SKB report R-13-40, p. 485.

Huldy, H.J. (1967) Gasdoorlatendheid van kunststoffen en rubbers. Plastica, 20(8), 348-357.

I&E. (2016) The national programme for the management of radioactive waste and spent fuel. Ministry of Infrastructure and Environment, Dutch programme.

Jackson, M.D., Mulcahy, S.R., Chen, H., Li, Y., Li, Q., Cappelletti, P., and Wenk, H.-R. (2017) Philipsite and Al-tobermite mineral cements produced through low-temperature water-rock reactions in Roman marine concrete. American Mineralogist, 102(7), 1435-1450.

Kempl, J., and Copuroglu, O. (2015) The interaction of pH, pore solution composition and solid phase composition of carbonated blast furnace slag cement paste activated with aqueous sodium monofluorophosphate. 15th Euroseminar on Microscopy Applied to Building Materials, p. 287-296, Delft, the Netherlands.

Leemann, A., Nygaard, P., Kaufmann, J., and Loser, R. (2015) Relation between carbonation resistance, mix design and exposure of mortar and concrete. Cement and Concrete Composites, 62, 33-43.

Lemmon, E.W. (2015) Vapor pressure and other saturation properties of water. CRC Handbook of Chemistry and Physics, p. 6-5. CRC Press Taylor and Francis Group.

Mazurek, M., Joe Person, F., Volckaert, G., and Bock, H. (2003) Features, Events and Processes Evaluation Catalogue for Argillaceous Media. NEA OECD No. 4437, p. 376.

Mladenovic, A., Neeft, E., Deissmann, G., Dähn, R., Geng, G., Koskowski, G., and Markku, L. (2019) ILW: Report describing the selected experiments and the existing/expected experimental results. Final version as of 24.12.2019 of deliverable D2.11 of the HORIZON 2020 project EURAD. EC Grant agreement no: 847593., p. 51, ejp-eurad.eu.

Neall, F. (1994) Modelling of the near-field chemistry of the SMA repository at the Wellenberg site: application of the extended cement degradation model, NAGRA Technical report 94-03, p. 45, Wettingen, Switzerland, www.nagra.ch.

Neeft, E.A.C., Visser, J.K.H., Peelen, W.H.A., Bigaj-van Vliet, A.J., and Larbi, J.A. (2009) Measurements and simulations of the distribution of moisture in concrete. In TNO-034-DTM-2009-02726, Ed, p. 81.

NIROND. (2013) ONDRAF/NIRAS Research, Development and Demonstration (RD&D) Plan State-of-the-art report as of December 2012. NIROND-TR-2013-E.
Savija, B., and Lukovíc, M. (2016) Carbonation of cement paste: Understanding, challenges, and opportunities. Construction and Building materials, 117, 285-301.
Steel, A. (1986) Product data sheet from AK Steel for 316/316L Stainless steel.
van Genuchten, M.T. (1980) A closed form equation for predicting the hydraulic conductivity of unsaturated soils. Soil. Sci. Soc. Am. J., 44, 892-989.
Vehmas, T., Schnidler, A., Löija, M., Leivo, M., and Holt, E. (2016) Reference mix design and castings for low-pH concrete for nuclear waste repositories. First Annual Workshop of the HORIZON 2020 CEBAMA Project, KIT-SR 7734. KIT Scientific Publishing, Barcelona (Spain).
Verhoef, E.V., de Bruin, A.M.G., Wiegers, R.B., Neeft, E.A.C., and Deissmann, G. (2014) Cementittious materials in OPERA disposal concept. OPERA-PG-COV020, www.covra.nl
Verhoef, E.V., Neeft, E.A.C., Deissmann, G., Filby, A., Wiegers, R.B., and Kers, D.A. (2016) Waste families in OPERA.OPERA-PG-COV023, www.covra.nl
Verweij, J.M., and Nelskamp, S. (2016) Definition of the present boundary conditions for the near-field model_1, OPERA-PU-TNO421_1 p. 37, www.covra.nl.
Weetjens, E. (2009) Update of the near field temperature evolution calculations for disposal of UNE-55, MOX-50 and vitrified HLW is a supercontainer based geological repository SCK CEN External Report, ER-86, p. 14.

7. French samples

Authors: Olivier Helson, Xavier Bourbon, Jad Zghondi (ANDRA), Thierry Vidal and Alain Sellier (LMDC/INSA Toulouse-UPS), Jianfu Shao and Thomas Rougelot (LaMcube/CNRS).

7.1 Mechanical safety function and performance target

For the Cigéo deep geological disposal site, the reinforced concrete structures plays a safety and functional role throughout the operating and reversibility phase. The current design of galleries and disposal cells expects and ensures an operating life of 100 to 150 years. To achieve these long lifetimes, most concrete structures will be made with high performance materials, with a strength class of C60/75 according to the European standard NF EN 206/CN [1]. The minimum characteristic strength on cylinders is therefore 60 MPa and the minimum characteristic strength on cubes is 75 MPa. However, the strength class of concrete varies according to the component: C40/50 for civil engineering, C60/75 for tunnels and disposal containers and C80/95 locally for some parts of the structure.

The role of the disposal cells is to ensure safety and security all along the operating period, especially to prevent damages to the disposal containers and to allow the possible withdrawal of the containers during the operating phase. Later on the lining long time rupture and the drift filling should not permit an extension of the excavation-damaged zone (EDZ). That is why the concrete lining design should integrate mechanical and durability specifications. During the lifetime of the lining, it is necessary to assess the impact of the steel corrosion on the mechanical behaviour of these reinforced concretes under loading. Coupled process (corrosion/mechanical evolution) have to be studied considering the additional effect of an external load and a chemical degradation (leaching, carbonation and sulphate attack).

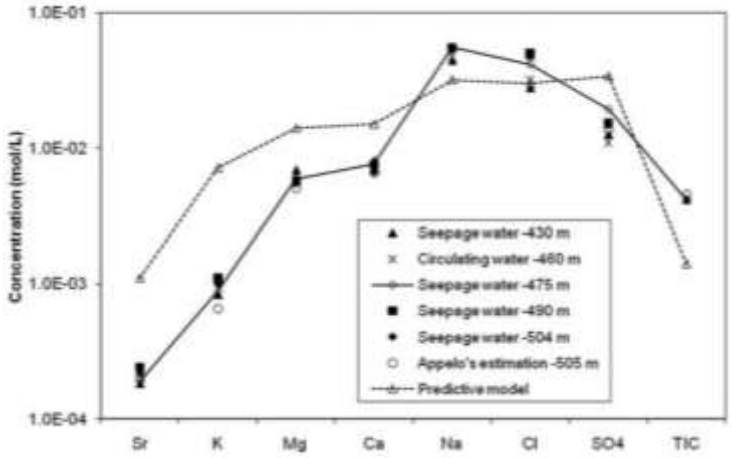

Figure 7-1: Measured compositions at a depth of -430, -460, -475, -504 m in the Callovo-Oxfordian Clay in Bure and estimation based on the experimental results of the water circulation experiment at -505 m [2].

Pore water characteristics of the Callovo-Oxfordian clay rock (COx) are available. The data come from in situ measurements at five different depths between -430 and -505 m with 3 experimental set-ups (Figure 7-1). The groundwater contains high levels of sulphates and chloride ions, which leads to an exposure class XA3 according to the European standard NF EN 206/CN [1]. Andra will provide a protocol for the synthesis of the poral water from the COx in chemical conditions close to those of underground research laboratory in Meuse/Haute-Marne at a depth of -490 m [3]. This will provide the partners with water representative of in situ conditions for the curing concrete in the laboratory.

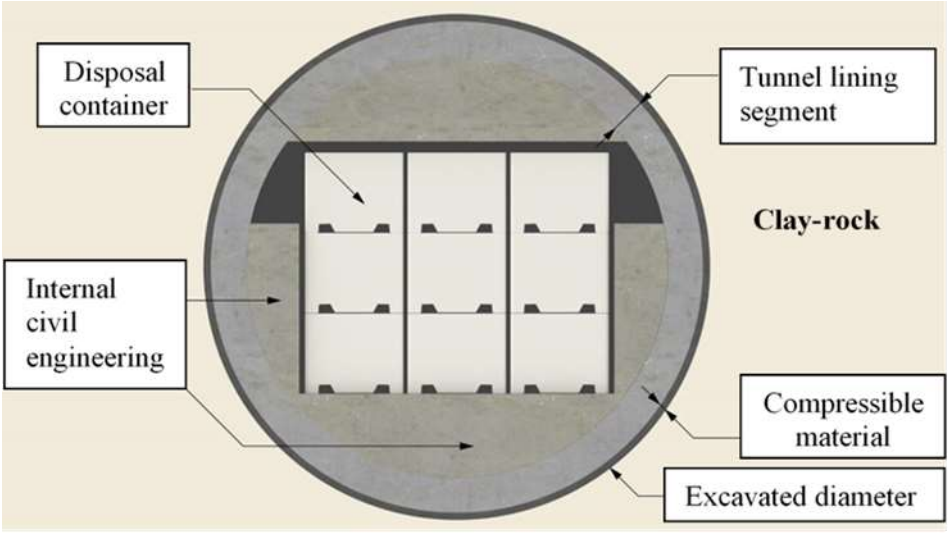

Figure 7-2: Schematic section of a long-lived intermediate-level waste disposal cell.

The exothermic behaviour of some radioactive waste exposes some structural concrete of the disposal cells with a maximum temperature of 50 °C.

7.2 Size of samples, concrete recipe

LMDC and LaMcube studies will focus on OPC (CEM I) concrete. The study concretes will be made by LMDC and some 15 cm cubic samples will be sent to the LaMcube for coring and then mechanical characterization tests. According to the European standard, the reference case will be a high performance concrete of class C60/75 (Table 7-1). However, for experimental reasons (mainly time required to perform chemical degradations), the studies will be carried out mainly on a concrete of class C40/50 obtained by changing the proportions of the recipe in Table 7-1.

Table 7-1: Reference concrete recipe

Component	Type	kg.m^{-3} for each component
Cement	CEM I 52,5 R CE PM ES CP2 NF	400
Water	-	171
Aggregate 1	Limestone sand washed with 10% fines Size of aggregate 0/4 (mm)	858
Aggregate 2	Washed limestone gravel Size of aggregate 5/12.5 (mm)	945
Additive 1	Superplasticizer	10

The LaMcube proposal:

For compressive tests, the LaMcube will use cylindrical cored samples with a diameter of 37 mm and a height of 72 mm. This size is suitable for the triaxial cell device that will be used for triaxial tests. Three-point bending tests are also planned on rectangular prisms of 70×70×280 mm dimension (according to the NF P 18-427 [4]). The sample size is intentionally reduced compared to French concrete standards (ex: NF EN 12390-5 June 2019 [5], NF EN 12390-3 June 2019 [6]), so that the impact of chemical degradation is large enough to be measured. The number of tests to be performed is presented in the Table 7-2.

Action 5 is carried out in collaboration with SCK-CEN (see Chapter 4). LaMcube will perform tri-axial tests on leached and carbonated samples (immersion in Boom clay and CO_2 bubbling) from SCK-CEN, both with and without microbial community. The objective is to follow the evolution of stress-strain curves, elastic properties and peak strength under these exposure conditions.

Table 7-2: Summary of the number of tests per action for the LaMcube: C40/50 concrete

Actions	Number of samples
Action 1: Uniaxial and triaxial compression tests on carbonated samples	15 samples (uniaxial and two confining pressures, 3 states of carbonation – about 0%, 50% and 100%, additional samples for several cases for representativity)
Action 2: Uniaxial and triaxial compression creep tests on carbonated samples	9 creep tests (uniaxial and two confining pressures, maximum 3 states of carbonation)
Action 3: Uniaxial and triaxial compression tests on initially damaged and carbonated samples	6 tests (uniaxial and one confining pressure, maximum 3 states of carbonation)
Action 4: Three point bending tests on carbonated samples	10 tests (5 carbonation states, 2 samples for each state)
Action 5: Triaxial compression tests on microbial degraded samples (SCK-CEN)	10 tests on SCK-CEN samples see Chapter 4

In former experiments dedicated to atmospheric carbonation of concrete [7], the selected CO2 content was 50% and experiments conducted at 80°C and 51% RH in order to have an optimal carbonation rate. Based on these results, carbonation tests will be carried out at a temperature up to 50 °C to accelerate the carbonation process. In addition, a pre-conditioning phase is necessary to obtain a controlled water saturation of the materials.

The LMDC proposal:

LMDC will collaborate with LaMcube and Andra to perform tests on specimens taken from Andra underground research laboratory (URL) and new specimens design and cast by the LMDC (Table 7-3).

The size of the samples from the URL will depend on the collection method. In the case of coring, we can expect a sample of around 10 cm in diameter knowing that the thickness of the targeted structures is about 50 cm. The LMDC will measure the residual mechanical performances of rebars anchorages in concrete. Pull-out tests include the challenge of grabbing the bars. This can be done by drilling into and tapping the bar, then inserting a threaded rod [8].

Due to the lack of witness specimens and possible difficulties to obtain numerous exploitable drilled cores in Andra's URL, LMDC will design and cast samples to characterize the steel-concrete bond behaviour in case of corrosion through pull-out tests. The exact size of the prisms will be designed after a preliminary test phase according to RILEM recommendations (decimeter scale). If necessary, the size of the samples will be adjusted in order to prevent concrete from breaking up. The two objectives are to study the effects of bond degradation, mechanical damage or damage due to material defects (ie the top bar effect), on corrosion initiation and propagation and the corrosion effects on steel-concrete bond.

The experimental program consists of casting concrete samples, prisms and prisms sawn from walls (1 meter high and same width as that of the prism) with steel reinforcement inside which will be submitted to bending tests leading to crack reaching the reinforcement location and further conditions inducing steel corrosion. The crack opening will be maintained using a wedge during the corrosion conditions. Two flexural crack widths will be studied to provoke two levels of steel-concrete bond damage around the crack tip. The crack will allow initiating the reinforcement corrosion at its tip.

The residual steel-concrete bond behaviour before and after steel corrosion will be assessed thanks to pull-out tests carried out on samples obtained from the sawing of prisms in two halves.

Table 7-3: Summary of the number of tests by action for LMDC: C40/50 concrete

Actions	
Action 1: Mechanical performance of corroded reinforced concrete from the	Number of samples : to be defined

underground laboratory					
Action 2: Pull out tests on corroded samples with initial bond mechanical damage or material defects at steel-concrete interface, submitted to wet/dry cycles.	Objectives	Number and type of samples	number of pull-out tests without corrosion	number of pull-out tests after the 1st phase of corrosion condition	number of pull-out tests after the 2nd phase of corrosion condition
	Validation of samples testing configuration and assessment of reference constitutive law for bond without corrosion	3 pull-out samples	*3*		
		3 prisms to provide 6 pull-out samples	*6*		
	Study of the effects of two levels of mechanical damage on steel corrosion evolution and steel-concrete bond	18 prisms cracked using bending test, with 2 different values of crack width	*12*	*12*	*12*
	Study of the effects of material defects at steel-concrete interface (top bar effect) on steel corrosion evolution and on bond	9 walls sawn to provide 9 prisms cracked using bending test	*6*	*6*	*6*
Action 3: The chemical influence on concrete of magnesium	Number of samples : to be defined				

The pull-out tests campaign will allow to analyse the following effects:

- The effects of mechanical damage on steel-concrete bond induced by a previous flexural loading of the prism;
- The effects of a defect at steel-concrete interface on bond; this defect, called top bar effect, results from plastic settlement of the concrete on a bar located in the upper part of a wall;
- The effects of the steel-concrete damage due to mechanical loading or top bar effect on steel corrosion initiation and propagation and the effects of the resulting corrosion in each case on steel-concrete bond;
- A total of 33 specimens of reinforced concrete will be cast:
    - 3 pull-out test samples will be tested to assess the reference constitutive law of steel-concrete bond without corrosion.
    - 3 prisms with reinforcement inside will be sawn each in two halves. Pull-out tests will be carried out on each half of these prisms. The results will be compared with that of the 3 previous pull-out test samples to validate the testing solution.
    - Once the test configuration validated, 18 prisms will be cast and then cracked using bending test to create a flexural crack. Two values of crack width will be studied with 9 prisms with each crack width. The nine prisms for each crack width will be stored in three conditions: 3 without corrosion, 3 stored during the single 1st phase of corrosion condition (accelerated atmospheric carbonation), 3 during the 1st and then the 2nd phase of corrosion condition (wet/dry cycles in situ water). After each condition type, 3 prisms will be sawn in two halves and 6 pull-out tests will be carried out.
    - 9 walls will be cast with a reinforcement located in the upper part to create some defects at the steel-concrete interface (top bar effect due to the plastic settlement of the concrete). 9 prisms of same geometry that the others will be sawn from walls. These prisms will be submitted to the same bending test (the lower crack width value and thus lower bond mechanical damage) and the same corrosion conditions as the other prisms. As explained previously, the bond behaviour will be assessed on pull-out samples sawn from prisms. All the samples and testing conditions are presented in table 3. Some supplementary samples of same geometry will be casted and submitted to the same corrosion conditions to record the evolution of corrosion through the measurement of the corrosion current.

The pull-out test will follow RILEM recommendations [9] with concrete sample crossed by a single centred reinforcement. The pull-out sample usually has sides 10 times the diameter of the reinforcement to prevent concrete from spalling.

The test specimens will be subjected to a 1st phase of accelerated carbonation condition (3% CO2 and 57% RH) and a 2nd phase of wetting (site water containing chlorides) and drying cycles to accelerate the carbonation process and thus possibly the corrosion of the steel bars. The exposure protocol for the concrete specimens is given in Table 4.

Table 7-4: Time and exposure conditions of the materials

Concrete maturation	Phase 1	Phase 2	
Water curing	carbonation (3% CO_2 and 57% HR)	wetting and drying cycles	
		Immersed in the COx synthetic solution (pH balance by monitoring the partial pressure of CO_2)	laboratory atmosphere : atm. pO_2 and hygrometry
~ 90 days	~ several weeks	~ one month	~ few days

Concerning wetting and drying cycles, the experimental conditions aim to have sufficient water and oxygen to ensure corrosion. The coupled effect of carbonation and leaching through cracks resulting from mechanical loading is possible. The impact of leaching should have a limited impact on the mechanical behaviour in pull-out tests, due to the non-renewal of the solution at the bottom of the crack (non-dynamic leaching system). Therefore, the study will focus on the mechanical degradation of the concrete caused by steel corrosion. The aim of the study is to achieve conditions representing the long-term behaviour of reinforced concrete as much as possible and to maximise the corrosion process by carbonation and chloride attack. To assess the coupled impact of carbonation and leaching, post-mortem chemical analyses will assess the progression of chemical degradation at different heights of the steel bar.

Stress corrosion is the subject of another project. These particular corrosion conditions are therefore not included in MAGIC but will be the subject of a state-of-the-art review.

7.3 Available characterisation of cementitious material

The C60/75 concrete studied in MAGIC is already well characterised in its sound state. The main physical and mechanical properties of concrete are presented in the Table 7-5 with the corresponding standards used.

Table 7-5: Mechanical and physical properties of the CEM I concrete [10].

Characteristics	CEM I concrete	Standard
Compressive strength at 28 days	62,5 MPa	NF P 18-406
Compressive strength at 3 months	65 MPa	NF P 18-406
Slump (T_0 + 1 h)	23 cm	NF P 18-451
Tensile strength by splitting test at 3 months	5.3 MPa	NF P 18-408
Young's Modulus at 3 months	40.9 GPa	RILEM
Poisson's ratio at 3 months	0.15	RILEM
Porosity	13%	AFREM
Gaz permeability	6.3×10^{-17} m²	AFREM
Water permeability	9.5×10^{-20} m²	
Bulk density	2465 kg/m^3	AFREM

[NB: RILEM is the International Union of Laboratories and Experts in Construction Materials, Systems and Structures and AFREM is the French Association for Research and Testing of Materials and Construction]

7.3.1 Mechanics

The available mechanical properties of the CEM I concrete are the compressive strength, splitting traction, the Young's modulus, and the Poisson's ratio (Table 5). The available pore structure properties of concrete are the water accessible porosity and the pore distribution obtained by mercury intrusion porosimetry (MIP).

7.3.1.1 Compressive strength

Unloaded and intact concrete

The available compression test results are in accordance with the French standard NF EN 12390-3 [6]. Before the test, the cylindrical concrete specimen follows a surfacing operation. The test consists of applying the load at a constant rate (0.6 ± 0.2 MPa/s) until the specimen fails.

The Figure 7-3 shows the evolution of the compressive strength as a function of water curing time (16h, 24h, 48h, 72h, 7 days, 28 days and 90 days) for C60/75 concrete. The comparison between the evolutions of the compressive strengths of CEM I concrete and CEM V concrete shows slower kinetics using CEM V (cement composed of clinker, fly ash and blast furnace slag). After 90 days of curing, the compressive strength of both concretes are greater than 60 MPa.

Degraded concrete

There is many researches on leaching degradation, many using accelerated ageing tests with ammonium nitrate. This type of solution allows a quick access to the ultimate neutralized state of the concrete, but remains representative of the consequences of an ultimate degradation with water. These experiments provide input data for modelling the coupling of chemical degradation with compressive and flexural creep, up to the structural scale [12].

The impact of carbonation on the mechanical behaviour of concrete has not been the subject of specific studies conducted by Andra. In fact, the formation of calcite induced by the carbonation process and the resulting clogging of porosity can have a positive effect on the mechanical properties.

The LaMcube conducted numerical simulations to represent the development of stresses and strains generated by corrosion within a cement paste. This modelling work involves experimental measurements that consist in measuring deformations generated by corrosion and the evolution of mechanical stresses in case of prevented displacement. This research work will be published soon.

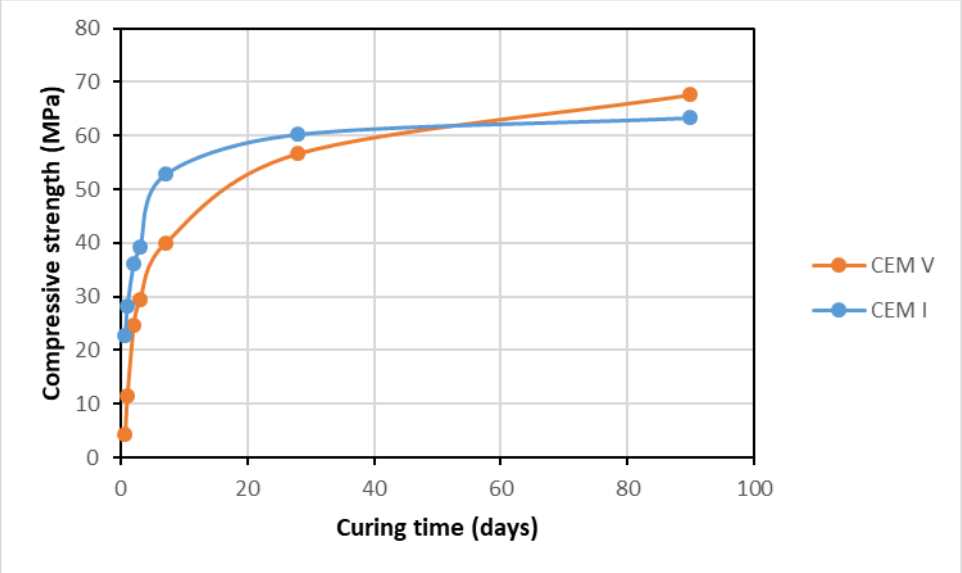

Figure 7-3: Evolution of compressive strengths as function of time for CEM I and CEM V concretes [11].

7.3.1.2 Young's modulus

The measurements of the elastic modulus followed the RILEM [13]. The modulus of elasticity in compression is determined on concrete cylinders 118 mm in diameter and 336 mm in height (figure 4). In practice, the measuring instruments used to measure deformations can be extensometers or gauges. The test comprises 10 continuous increasing and decreasing loading cycles ranging between 0.5 MPa and one third of the reference compressive strength.

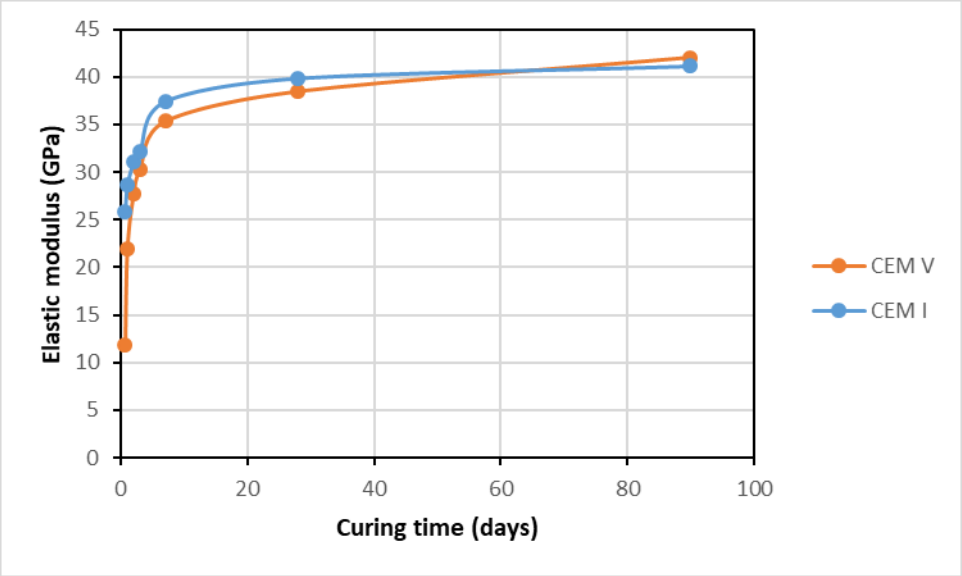

Figure 7-4: Evolution of elastic modulus as function of time for CEM I and CEM V concretes [11].

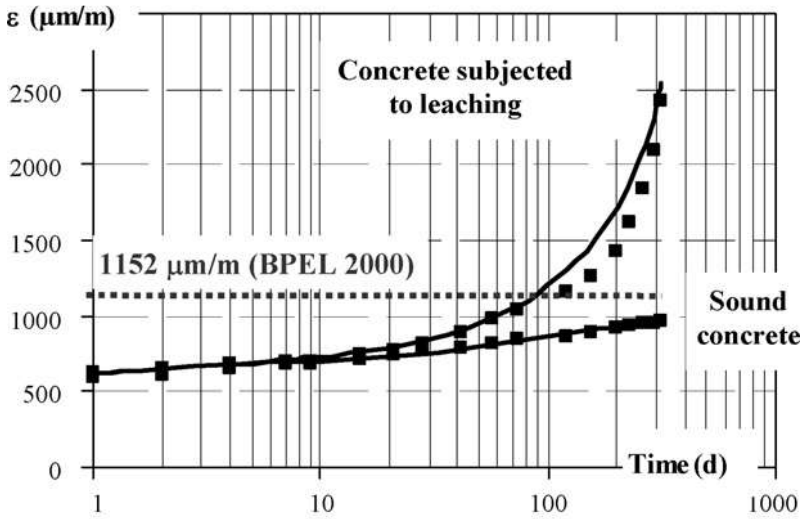

Figure 7-5: Comparison of creep curves between sound concretes and leached ones [12].

The Figure 7-4 shows the evolution of the elastic modulus as a function of time for C60/75 concretes at the same curing times as the compression tests. The evolution of hydration as a function of time leads to an increase in elastic modulus values and the kinetics are slower for concretes composed of CEM V. After 90 days of curing, the moduli of elasticity values of both concretes are greater than 40 GPa.

For the creep tests coupled with leaching, an increase in creep kinetics occurred which is correctly reproduced by the chemical-mechanical model [12].

7.3.1.3 Porosity

For hardened concrete, the most widely used method is porosity accessible to water. A first measurement protocol has been recommended in France by the AFPC-AFREM [14] and since 2010, the standard in force is the NF P 18-459 [15].

The porosity accessible to water was determined according to the following procedure:

- The samples are saturated under vacuum for a period of 48 hours and then dried in an oven at 105°C until the mass is stabilized;
- The ratio between the volume of water having saturated the porosity and the apparent volume gives the porosity accessible to water: $\eta = (m_{air} - m_{dry}) / (m_{air} - m_w)$, with m_{air} the mass of the sample saturated in water and dried on the surface, m_{dry} the mass of the dry sample and mw the mass of the sample obtained by hydrostatic weighing.

Table 7-6: Summary of characterization tests with porosity accessible to water values and dispersion of results (Andra data compilation).

Strength class of concrete	Binder	Mean porosity	Standard deviation
C60/75	CEM I	12,5 %	± 0,8 %
	CEM V	14,4 %	± 0,7 %

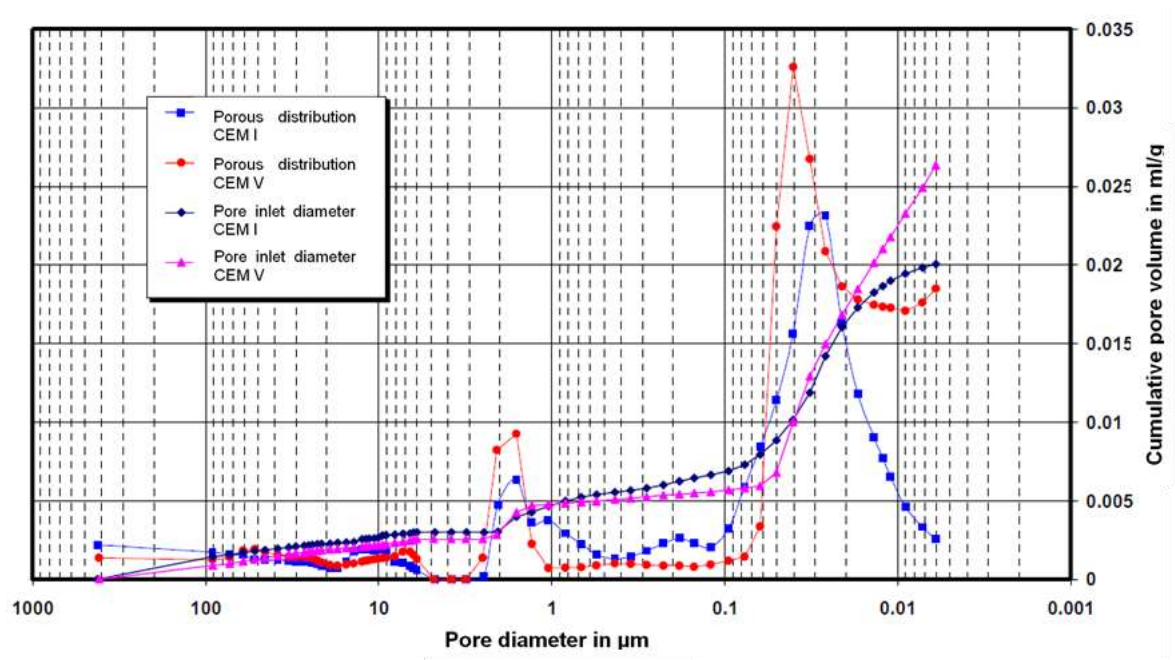

Figure 7-6: Result of mercury porosity distribution and pore inlet diameter distribution [16].

The porosity measured by MIP is more than two time lower than water porosity (5% with CEM I and 6.3% with CEM V). Below a radius of 0.06 µm, the inlet diameter curve of CEM V increases significantly and that of CEM V is stabilizing (Figure 7-6). The evolution for CEM I concrete indicates that it has few pores with a diameter less than 0.07 µm.

7.3.2 Chemistry

The available chemical properties of the CEM I concrete are the mineralogical composition, thermo-gravimetric analysis, X-ray diffractometry and pore water composition.

7.3.2.1 Mineralogy

Unloaded and intact concrete

CEM I concrete can be described as a combination of portlandite, C-S-H (C/S 1.6), ettringite, calcium monosulphoaluminate, hydrotalcite and ferrous hydrogarnet (C3FH6). The limestone aggregates consist mainly of calcite with some quartz.

Table 7-7: Mineralogical Composition of Concrete [17]

Phase (Volume Fraction)	BHP CEM I
Calcite	0.627
Portlandite	0.050
C-S-H 1.6	0.120
Monocarboaluminate	0.020
Ettringite	0.031
Hydrotalcite	0.003
Hydrogarnet-Fe	0.018
Pyrite	_
Porosity	0.13

Degraded concrete

Thermo-gravimetric analysis (TGA) is available for CEM I concrete and used to characterise the carbonation state of the material.

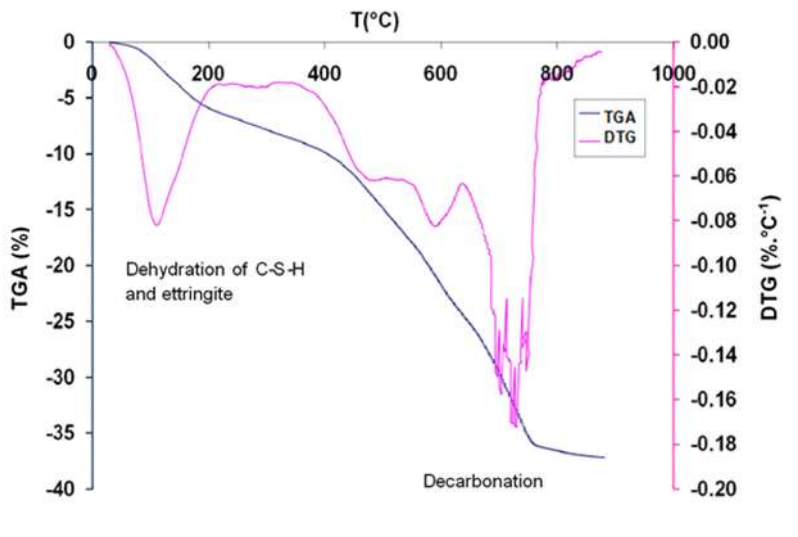

Figure 7-7: TGA and DTG curves obtained on carbonated CEM I concrete [10]

In the Figure 7-7, the first peak identified around 100°C corresponds to the dehydration of C-S-H and ettringite but also to the departure of free water. The two peaks observed between 600°C and 800°C are due to the decomposition of calcium carbonates. The absence of a peak at 400°C shows that almost no Portlandithe remains in the material after the test. In addition, the results indicate that aggregate residues remain in the tested crushed concrete.

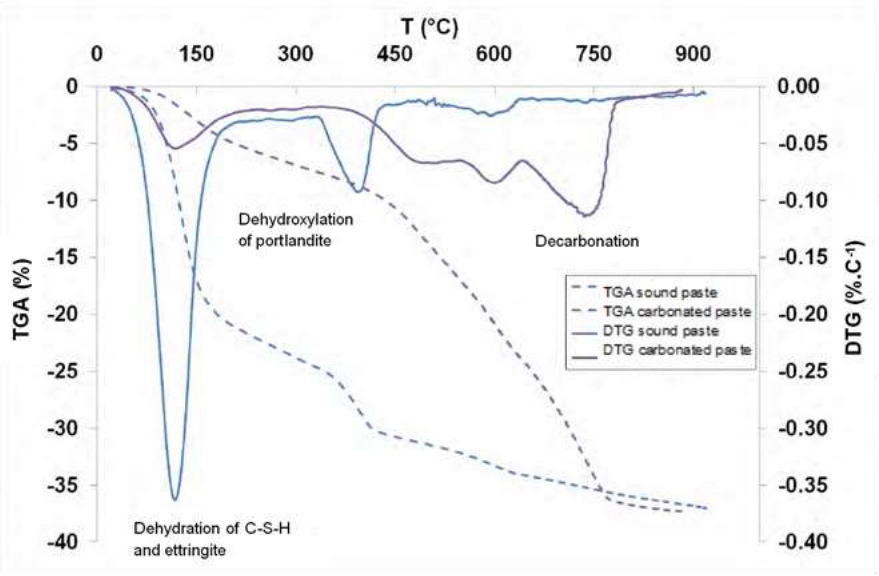

Figure 7-8: ATG and DTG curves obtained on sound and carbonated cement paste [9]

The results of X-ray diffractometry (XRD) analyses indicate the almost exclusive presence of calcium carbonates which are vaterite and calcite (Figure 7-9). This result is consistent with the two peaks located between 600 and 800°C on the DTG curves.

We also note on the diffractogram the absence of other hydrated phases as well as anhydrous phases (C2S, C3S) with the exception of C4AF, which is much more difficult to hydrate.

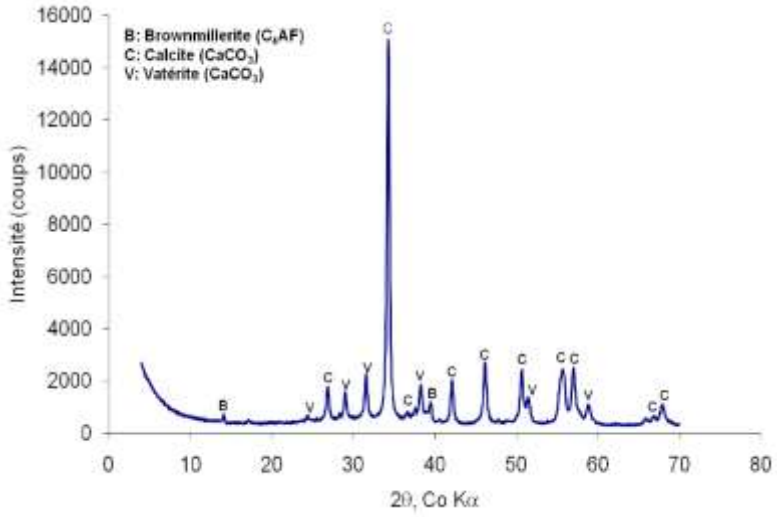

Figure 7-9: *Diffractogram of carbonated cement paste [9]*

7.3.2.2 Pore water chemistry

The composition of the interstitial pore solution constituted by free water varies with the curing time of the material. Interstitial solution extractions were performed on concrete stored at 20°C and 100% relative humidity. Before extraction of the pore solution, the 11×22 cm cylindrical specimens are cut into 3 cm slices, and then crushed. A rough sorting is carried out in order to collect the maximum of paste and to avoid the aggregates. The extracted solutions are filtered at 0.45 µm and then a pH measurement is performed as soon as possible after extraction.

The pH meter is calibrated before each test between 10 and 12 at room temperature (22°C) making a test with a buffer at pH 11 before each measurement. The solution is then acidified with HNO_3 (pH

between 3 and 6 according to the formulations) to keep it until its analysis. The contents of Na^+, K^+, Ca^{2+} and SO_4^{2-} are measured by chromatography and the silica content is measured by ICP (Inductively coupled plasma). The results are presented in the Table 7-8.

Table 7-8: Chemistry of concrete pore solution studied [18]

Concentrations [mmol/L]	Na^+	K^+	Ca^{2+}	SO_4^{2-}	pH
Curing time 1 year	92,9	77,1	0,02	1,1	13,1

7.3.3 Microbiology (if available)

In the LMDC-LaMcube-Andra proposal, no experiments are planned on this topic in MAGIC. However, Andra can contribute its knowledge of bacterial families in a COx environment. The use of the "Interaction of Rock and Hydraulic Binders" and "Bacteriological Disturbance" experiments in the Meuse/Haute-Marne underground laboratory provides information on the evolution of microbial activity and population. Depending on the interest of other partners, Andra can make samples from these experiments available for analysis.

7.4 Description of experimental set-up

Samples coming from the underground laboratory:

A sampling campaign is planned on the underground laboratory structures (reinforced concrete slab and shaft). The coring will be carried out at the end of 2021 or early 2022. The objective is to obtain aged concrete samples (corrosion, carbonation, chemical evolution in contact with the geological environment). The composition of cast-in-place concrete will be made available to the partners.

The aim of taking reinforced concrete samples in situ is to obtain sufficiently corroded samples to be analysed. Another challenge is to find the position of the reinforcement in order to successfully remove the reinforced concrete, considering that the objective is then to carry out pull-out tests.

7.5 Characterisation of cementitious material to be performed in MAGIC

In the LMDC proposal, the tests performed are pull-out tests under different conditions (sound concrete, with or without an initial bond mechanical damage, with or without top bar effect, with or without corrosion). Pull-out tests will be carried out from the second half of 2022 until the end of 2023. The other characterisation tests planned will consist of determining the compressive strength, modulus of elasticity, Poisson's ratio, density and porosity of the sound concrete. These input data are essential for the numerical simulations.

The standards used are given in Table 7-5. The pull-out tests will follow the international recommendations of RILEM [8].

Figure 7-10: Experimental setup to carry out pull-out test.

Figure 7-11: Experimental setup for the triaxial (left) and creep tests (right) [16].

In the LaMcube proposal, the tests performed are uniaxial and triaxial compression tests including creep conditions. The devices used are shown in Figure 11. The experimental programme also includes three-point bending tests on concrete prisms. The aim is to evaluate the mechanical behaviour of the material (compressive strength, Young's modulus, energy release rate in flexion…) for different levels of carbonation, including samples mechanically degraded under loading before being exposed to accelerated carbonation. An estimate of the test planning over the duration of the project is given in the Table 7-9.

Table 7-9: Estimated planning of tests by action for the LaMcube

Action	Start	Duration
1: Uniaxial and triaxial compression tests on carbonated samples	end of 2021	~ 1 year
2: Uniaxial and triaxial compression creep tests on carbonated samples	mid-year 2022	~ 1 year
3: Uniaxial and triaxial compression tests on initially damaged and carbonated samples	mid-year 2022	~ 6 months
4: Three point bending tests on carbonated samples	mid-year 2023	~ 6 months
5: Triaxial compression tests on microbial degraded samples (Collaboration with SCK-CEN)	beginning of 2023	~ 6 months

7.6 References

[1] NF EN 206/CN. (2014) AFNOR, Concrete - Specification, performance, production and conformity - National addition to the standard NF EN 206.
[2] A. Vinsot, S. Mettler, S. Wechner. In situ characterization of the Callovo-Oxfordian pore water composition Physics and Chemistry of the Earth, 33 (2008), pp. S75-S86.
[3] M. Agnel, A. Vinsot, J-C. Robinet. Experimental protocol for the synthesis of poral water in the Callovo-Oxfordian claystone at 25 °C. Technical Document. CGRPASTR210001.
[4] NF P18-427 (December 1996) AFNOR. Concrete. Determination of the dimensional variations between two opposite faces of hardened concrete test specimens.
[5] NF EN 12390-5 (June 2019) AFNOR. Testing hardened concrete - Part 5: flexural strength of test specimens.
[6] NF EN 12390-3 (June 2019) AFNOR. Testing hardened concrete - Part 3: compressive strength of test specimens.
[7] Emeline Drouet (2010). Impact de la température sur la carbonatation des matériaux cimentaires : prise en compte des transferts hydriques. PhD thesis. École normale supérieure de Cachan.
[8] K. Lundgren, S. Robuschi and K. Zandi. Methodology for Testing Rebar-Concrete Bond in Specimens from Decommissioned Structures. International Journal of Concrete Structures and Materials (2019).
[9] AAC 8.1 (1992) Pull-out test for reinforcement. RILEM Recommendations for the Testing and Use of Constructions Materials, pp. 140-142.
[10] H. Ranaivomanana. Transferts dans les milieux poreux réactifs non saturés: application à la cicatrisation de fissure dans les matériaux cimentaires par carbonatation. PhD thesis. University of Paul Sabatier Toulouse (2010).
[11] Camps, G (2008). Étude des interactions des interactions chemo-mécaniques pour la simulation du cycle de vie d'un élément de stockage en béton. PhD Thesis. University of Paul Sabatier, Toulouse, France.
[12] A. Sellier, L. Lacarriere, M. El Gonnouni, X. Bourbon. Behavior of HPC nuclear waste disposal structures in leaching environment. Nuclear Engineering and Design, Elsevier, 2011, 241 (1), pp.402-414.
[13] CPC 8 (1975) Modulus of elasticity of concrete in compression. RILEM Recommendations for the Testing and Use of Constructions Materials, pp. 124-125.
[14] AFPC-AFREM, « Méthodes recommandées pour la mesure des grandeurs associées à la durabilité ». Report on technical days, Toulouse, 11 and 12 December 1997. Book.
[15] NF P18-459 (AFNOR). « Béton - Essai pour béton durci - Essai de porosité et de masse volumique », March 2010. Standard.
[16] F. Brue (2011). « Rôles de la température et de la composition sur le couplage thermo-hydro-mécanique des bétons ». Ecole Centrale de Lille, 2011. PhD thesis.
[17] Trotignon, L., Thouvenot, P., Munier, I., Cochepin, B., Piault, E., Treille, E., Bourbon, X., Mimid, S., 2011. Numerical Simulation of Atmospheric Carbonation of Concrete Components in a Deep Geological Radwaste Disposal Site During Operating Period. Nuclear Technology 174, 424-437.
[18] Maud Codina (2007). « Les bétons bas pH - Formulation, caractérisation et étude à long terme. » PhD thesis. INSA de Toulouse.

8. German samples

Authors: Kyra Jantschik (GRS) and Johannes Kulenkampff (HZDR)

8.1 Mechanical safety function and performance target

The lining is one key component guaranteeing the safety during the operational and post-operational phase of future nuclear waste repositories in sediments and sedimentary rock formations. Cementious materials are preferably used to produce the lining. The materials are indeed characterized by such a strength and stiffness that they sustain the overburden pressure in short-term. However, their mechanical characteristics might alter through the mechanical loading and other environmental conditions in long-term. For instance, the constant mechanical loading might induce creep deformations, and the percolation of solutions originating in the rock formation might trigger material degradation and consequent preferential flow path evolution, if the lining is left in place in the post-closure phase. It is thus of major interest to better understand those chemo-mechanically coupled processes.

Former experiments with cement-based materials in contact with corrosive solutions showed a significant loss of material stability due to degradation. Chemical and mineralogical investigations of concrete in contact with saline solution of “Standortmodell Nord” (Germany) indicated chemical attack by magnesmium, sulfate and ammonium and precipitation of gypsum and ettringite. The chemical attack results in local damage, increase of porosity and decrease of compressive strength. Regarding the “Standortmodell Nord” temperatures between 30 – 40 °C are expected. [Herold et al 2020] Higher temperatures usually accelerate the kinetics of degradation processes. Different flow-through and triaxial compression experiments are performed on low-pH cement samples in order to evaluate the impact of chemically-induced degradation processes on the mechanical characteristics of cementious materials. The experiment program is complemented by mineralogical, physico-chemical and microstructural analysis.

8.2 Size of samples, concrete recipe

Cylindrical samples are characterized by a length and diameter of 100mm and 50mm, respectively.
The composition of the low-pH-cement S5 that is employed in the experiment program is presented in Table 8-1.

Table 8-1: Formulation of low-pH-cement S5 [Herold et al 2020]

Component	Type	Mass [kg/m^3]
Cement	CEM I, 42.5 N, bulk density 3.10 g/cm3	160.00
Microsilica	bulk density 2.16 g/cm3	120.00
Water	-	160.00
EFA-Fuller	bulk density 2,29 g/cm3	240.00
Sand	0 – 2 mm, bulk density 2.65 g/cm3	792.60
Gravel sand	2 – 8 mm, bulk density 2.65 g/cm3	792.60
Water	-	166.00
		∑ 2271.20

8.3 Available characterisation of cementitious material

Data on the low-pH-cement S5 and its chemo-mechanical characteristics is limited since experiments at GRS and HDZR laboratories are currently under preparation and have not been commenced yet.

8.3.1 Mechanics

8.3.1.1 Compressive strength

Compressive strength experiments were performed on samples stored at an ambient temperature of 30°C and a relative humidity below 50%. Samples were tested after 7 and 28 days of curing. Values of measured compressive strength are presented in Table 2.

Table 8-2: Compressive strengths of low-pH cement S5 [Herold et al 2020]

Time [days]	Compressive strength [MPa]
7	42
28	58

8.3.1.2 Young's modulus

Compressive strength experiments were performed on samples stored at an ambient temperature of 30°C and a relative humidity below 50%. Samples were tested after 7 and 28 days of curing. Values of measured Young's modulus are presented in Table 3.

Table 8-3: Young's modulus of low-pH cement S5 [Herold et al 2020]

Time [days]	Young's modulus [GPa]
7	20
28	22

8.3.2 Chemistry

8.3.2.1 Composition of components in the low-pH concrete

The composition of the different components of low-pH-cement S5 was measured by BGE Technology by means of X-ray fluorescence analysis (XRF). It is presented in Table 8-4.

Table 8-4: Composition of the components of low-pH-cement S5 [Herold et al 2020]

Component	CEM I 42.5 N	Microsilica	EFA-Fuller	Sand	Gravel sand	Water
Mass [kg/m^3]	160	120	240	792,6	792,6	166
Quantity of elements/compounds [Mass-%]						
SiO_2	21.02	96	52.09	95.14	95.14	-
Fe_2O_3	2.85	0.6	8.22	0.82	0.82	-
Al_2O_3	5.04	1.2	20.46	2.13	2.13	-
CaO	64.18	0.3	7.34	0.52	0.52	-
MgO	1.67	0.1	1.92	0.1	0.1	-
SO_3	2.58	0.5	-	-	-	-
SO_4	-	-	1.59	0.11	0.11	-
Na_2O	0.24	0.1	1.31	0.27	0.27	-
K_2O	0.7	0.4	2.05	0.69	0.69	-
Cl	0.016	0.1	-	-	-	-

8.4 Description of experimental set-up

Experiments are performed at GRS and HZDR laboratories. The experiment program comprises two parts: Experiment program part A aims to investigate how the fluid permeability of low-pH-concrete samples develops as a corrosive solutions percolates through them and triggers degradation processes. The degree of degradation can be then estimated by monitoring variations in the fluid permeability and in the chemical characteristics of the outflowing solution. Experiment program part B focusses on the analysis of the mechanical characteristics of the concrete samples, in particular their Young's modulus, Poisson's ratio and parameters adopted for failure crierion definition, after percolation and consequent degradation.

Experiments are expected to commence in autumn/ winter 2021/2022. Results of flow-through and subsequent triaxial compression experiments are expected to be exploitable 3, 6, 12, and 24 months after flow-through experiment initiation.

8.4.1 Part A: Flow through of corrosive solutions through low-pH concrete

In part A concrete samples are percolated with a corrosive solution for about 3, 6, 12, and 24 months at an ambient temperature of 25°C. Solution composition corresponds to the composition of "Konrad"-solution, whose components and other characteristics are presented in Table 8-5.

Table 8-5: Parameter for "Konrad-solution" at 25°C [Herold et al 2020]

Component	Mass [mol/kg H_2O]
Sodium	3.659
Potassium	0.006
Calcium	0.241
Magnesium	0.123
Chloride	4.375
Sulphate	0.009
Carbon	$2.6 \cdot 10^{-5}$
Additional parameter	
pH	7.9
Density	1155 kg/m^3
Viscosity	2.0 mPa·s

In total, 12 samples are percolated at the GRS laboratory. For this purpose, concrete samples are inserted initially in advection cells made up of Plexiglas. The employment of such cells allows microscale measurements by means of computerized tomography (CT) during percolation experiment performance. The annular space between the sample and Plexiglas cylinder is then filled with resin. Upon the curing of the resin in its annulus and its closure, the advection cell is connected to the feed pipes of "Konrad-solution". Solution is injected with an injection pressure around 0.5 MPa. Expecting that the solution percolates through the samples, the outflowing solution is collected in wide mouth bottles. Based on the mass of outflowing solution per unit of time, development of fluid permeability can be calculated. The results are complemented by the chemical analyses of outflowing solution. This multi-scale approach allows to estimate the degree of degradation.

One other concrete sample is investigated at HZDR laboratory. A small volume of Konrad solution, labelled with the PET-nuclide 22Na (activity 3.16 MBq), is injected into the head space between the end cap and the sample. The spreading of the spatial tracer distribution into the sample is then observed over a period up to 24 months. In this time several PET frames are taken with time steps according to progress of the the tracer front (between days and months).

The method of GeoPET has been developed and advanced at HZDR. A number of show case experiments could prove its capability for spatiotemporal quantification of tracer transport experiments (Kulenkampff et al., 2016) with very high sensitivity ("picomolar") and reasonable spatial resolution (about 1 mm). PET can clearly and quantitatively display the propagation of the tracer in the sample. It

is thus a laboratory-scale method that is capable of non-destructive quantitative visualization and parametrization of this particular heterogeneous tracer transport.

In addition, the process of degradation can be estimated by means of CT measurements. Microfocus computerized tomography (µCT) is the commonly applied method for high-resolution 3D structural imaging of geomaterials. µCT-images are foreseen according to the investigated degradation states in triaxial compression short-term strength test.

8.4.2 Part B: Determination of material strength dependent on degree of degradation

Triaxial compression (TC) experiments are carried out by means of a triaxial testing maschine allowing to investigate the behavior of building material samples under thermo-hydro-mechanical conditions. Its major components are the load frame, the axial load piston, the laterally surrounding cell, the axial load cell, the circumferencial strain gauge and two LVDT-transducers for axial deformation measurement. The preferred length and diameter of cylindrical samples are 100mm and 50mm, respectively. The capacity of the axial load cell is limited to a maximum force of 100kN which corresponds to a maximum applicable axial stress of about 50 MPa considering a sample diameter of 50mm. If required, the lateral stress can be increased up to 400 bar and the oil temperature up to 120°C. Further, the development of pore pressure can be measured by means of pore pressure sensors which are positioned at the outlets of the top and bottom faces of the sample.

8.5 Characterisation of cementitious material to be performed in MAGIC

8.5.1 Mechanics

8.5.1.1 Compressive strength

Triaxial compression (TC) experiments are performed on concrete samples upon terminating the percolation with corrosive solution for about 3, 6, 12, or 24 months. Three samples are accordingly analyzed in one TC experiment series per time step. Plexiglas cylinders and resin are removed from the samples by means of a turning lathe. Prepared samples are placed in the triaxial cell and subsequently subjected to an isotropic stress state. The adjusted lateral stress of 1, 3, or 5 MPa is kept constant during the shear phase. A strain-rate of 0.25%/ min is then adopted to deform the samples in axial direction. Upon reaching an axial strain of 1%, the samples are unloaded until they recover 0.25%. The subsequent strain-controlled reload eventually induces failure. Results can be exploited to derive the Young's modulus, the Poisson's ratio and parameters defining a failure criterion. Variations in those parameters can be directly linked to the degree of degradation.

8.5.1.2 Permeability

Fluid permeability is measured in flow-through experiments. Therefore, solution is injected at one sample surface and is collected at the opposite surface. Indeed, permeability may be measured not before solution percolated the sample completely.

Based on Darcy's law for compressible fluids the permeability k is calculated according to:

$$k = \frac{Q \cdot \eta \cdot p_1 \cdot L}{\Delta p \cdot p^* \cdot A}$$

$k = permability\ [m^2]$

$q = volume\ flow\ \left[\frac{m^3}{s}\right]$

$\eta = daynamic\ viscosity\ of\ solution\ \left[\frac{kg}{m \cdot s}\right]$

$p_1 = gas\ pressure\ at\ outflowing\ surface\ \left[\frac{kg}{m \cdot s^2}\right]$

$p_2 = gas\ pressure\ at\ inflowing\ surface\ \left[\frac{kg}{m \cdot s^2}\right]$

$L = Length\ of\ the\ sample\ [m]$

$\Delta p = difference\ pressure\ (p_2 - p_1)\ \left[\frac{kg}{m \cdot s^2}\right]$

$p^* = average\ intrnal\ pressure\ in\ the\ pores\ \left(\frac{p_1 + p_2}{2}\right)\ \left[\frac{kg}{m \cdot s^2}\right]$

$A = cross\ section\ area\ of\ the\ sample\ [m^2]$

8.5.1.3 Observation of fluid penetration

Positron emission tomography will be applied to monitor fluid injection over a period of months, and with a spatial resolution of 1 mm. The flow rate is determined with high sensitivity from µCT-based fluid level measurements in the reservoir, while the fluid pressure is kept constant. This enables fluid permeability determination during the PET experiment.

8.5.1.4 Geo-PET

GeoPET is a versatile method that can be adapted to the experimental conditions. However, only the tracer is detectable with PET. It yields no information about the solid phase. Usually single pores are not resolved with this method. This is not required, because the tracer propagation is observed as tracer flux integrated over the voxel volume.

The method can be applied both for pure molecular diffusion of the tracer ions, when no pressure is applied to the fluid. If the shape of the sample volume deviates from simple geometrical bodies, the diffusion coefficient and - if applicable – its anisotropy and inhomogeneity is derived from model fitting with FEM.

If pressure is applied to the fluid, and the flow rate exceeds the propagation by molecular diffusion, it becomes a process tomography method of the advective process. It yields permeability and information about the transport pathway and velocity distribution on the mm-scale. The progress of the tracer directly yields fluid velocity on the mm-scale and its distribution, as long as the tracer is non-reactive. Otherwise, the tracer propagation analysis has to include geochemical modelling. Apart from velocity, the propagation pathway will be reconstructed, yielding information about the effective transport volume.

8.5.1.5 Structure changes (CT)

Generally, µCT yields the spatial density distribution of the solid phase. The resolution depends on the machine parameters (focal spot size, detector pixel number, and magnification). The typical spatial resolution of samples with the size of complete cores is in the order of 50 µm, smaller samples allow higher resolution that is proportional to their size.

Alteration of the samples could cause structure changes on the resolved scale, and density (gray level) differences, when density is varied due to chemical reactions or structural changes below the resolved scale.

Detectable structure changes can be quantified directly by image analysis of the segmented pore space. Interpretation of density effects is less significant and could be erroneous. If such changes are detected, other methods (e.g. XRD, REM) will be applied for verification.

8.5.1.6 Porosity

Representative samples will be characterized with µCT of the complete samples. These tomograms are also required for PET reconstruction. The expected resolution of the complete samples is 50 µm. Where required, µCT-images will be recorded on small subsamples, in order to detect smaller, possibly interconnected pores. Segmentation of these tomograms is the basis for pore size analysis.

8.5.2 Chemistry

8.5.2.1 Mineralogy

Composition of minerals is determined by means of powder X-ray diffraction (XRD). Even though, XRD does not allow to analyse all phases in cement, changes in phase composition might be estimated in accordance with changes in composition of outflowing solution. XRD analysis is performed on non-percolated and percolated samples after the triaxial compression experiments. Percolated samples are cut perpendicularly to the center axis in several sections. The step-by-step analysis allows the detection of changes in phase composition along the direction of injection. If proven to be of interest, adopted analysis methods might complement the XRD-analysis in ongoing project.

8.5.2.2 Composition of outflowing solution

Analysis of solution composition is conducted with ICP-OES (DIN EN ISO 11885:2009-09) and ICP-MS (DIN EN ISO 17294-2) measurements. The measuring process needs to be adapted with respect to high-saline solutions. Chloride is measured by titration (DIN 38405 Teil 1). The outflowing solution is collected in wide mouth bottles which are exchanged once 20 ml of solution are collected. The solution of each bottle is analysed separately, so variations in solution composition can be linked to variations in fluid permeability.

8.5.2.3 pH

pH is continuous measured in collected solutions of percolations experiments corresponding to DIN EN ISO 10523:2012-04.

8.5.2.4 Electric conductivity

Collected solutions of percolations experiments will be investigated continuous regarding to its electric conductivity. Electric conductivity is measured regarding to DIN EN 27 888(DEV C8).

8.5.2.5 Diffusion coefficients

The tracer diffuses from the homogeneous resorvoir into the unknown material, according to Fick's law. The propagation could be local and patchy, homogeneous, and anisotrope..The determination depends on the measuring results. For example, homogeneous diffusion along the cylinder axis of a cylindrical sample can be directly parameterized with the 1D-diffusion law.

If the pattern becomes patchy and inhomogeneous, evaluation might become intriguing.

In principle, local diffusion properties could be derived from the spatiotemporal tracer distribution, but parameterization would require inverse modelling computations. Instead, we considered descriptive statistics of the radial diffusion profile, i.e. quantiles and the interquantile range of the axial tracer concentration. These measures are robust measures of the tracer diffusion. As mean diffusion depth, we here defined the interquartile range. However, up to now there is no routine evaluation method available. For this case that is substantial when local alterations occur, i.e. by mechanical or chemical impact.

8.6 References

[Herold et al 2020] Herold, P., Simo, E., Räuschel, H., Engelhardt, H-J., te Kook, J., Pflüger, B., Scior, C., Studeny, A. 2020: Ausbau von Grubenbauen für ein HAW-Endlager in Tonstein, BGE TECHNOLOGY GmbH, BGE TEC 2020-26

[Kulenkampf et al 2016] Kulenkampff J., Gründig M., Zakhnini A., Lippmann-Pipke J. 2016: Geoscientific process monitoring with positron emission tomography (GeoPET). Solid Earth 7, 1217-2031.

9. Swiss samples

Authors: Michele Griffa (Empa), Sergey Churakov, Thomas Gimmi and Bin Ma (PSI).

9.1 1Mechanical safety function and performance target

According to the current design, two types of radioactive waste repositories are considered in Switzerland. One contains the high-level waste from the reprocessing and spent fuel elements (SF/HLW). Another contains long and intermediate level waste (L/ILW) from the operation and decommissioning. The SF/HLW and L/ILW repositories can be co-located in a combined repository within Opalinus Clay (OPA) as the envisaged host rock. Due to the differences in inventory, thermal output and the waste volumes, the repository design and the barrier materials for SF/HLW and L/ILW are very different (see Figure 1). SF/HLW are stored in steel casks and enclosed by a bentonite barrier, which serves as backfilling material. In the current design, cementitious materials are applied for the tunnel support system. The main (safety) functional feature of the latter is related to mechanical strength necessary to withstand the mechanical convergence of the tunnel during the construction and operational phases.

Cement-based composites are the major components of the L/ILW disposal systems (see Figure 9-2). Cement paste is the primary waste matrix for radioactive waste. The containers are made of concrete and the void space within the container will be filled with a mortar. The disposal caverns for the L/ILW repository are supported by a tunnel support system made of reinforced shotcrete and concrete, which protect the walls from rock fall and take up the loads during the construction and emplacement phases. The space between the disposal containers and the cavern wall is filled with a grain-supported mortar, which takes up the mechanical stresses by grain-to-grain contact while providing gas storage volume and space for gas escape between the aggregates. After the emplacement of the waste containers and filling the void space with mortar, the caverns are closed with a sealing system, consisting of an initial seal made of a sand-bentonite mixture, a transition layer and, finally, closed with a concrete plug. The tunnel galleries will be filled with clay-based material.

Current documentation of repository design uses generic descriptions of the material, without explicit specification of the recipe for the cementitious material. These are requested at the stage of the construction licence application. Ordinary Portland cement (OPC) is often considered as the reference cementitious binder for the L/ILW repository. However, for the plugs and the tunnel support system of the HLW repository, this can also be a low pH cement. Primary chemical processes leading to the degradation of the massive cement-based constructions are the tunnel convergence, carbonation, internal cement degradation and the interaction with OPA pore water, as the repository will start to become saturated with water during its long-term evolution.

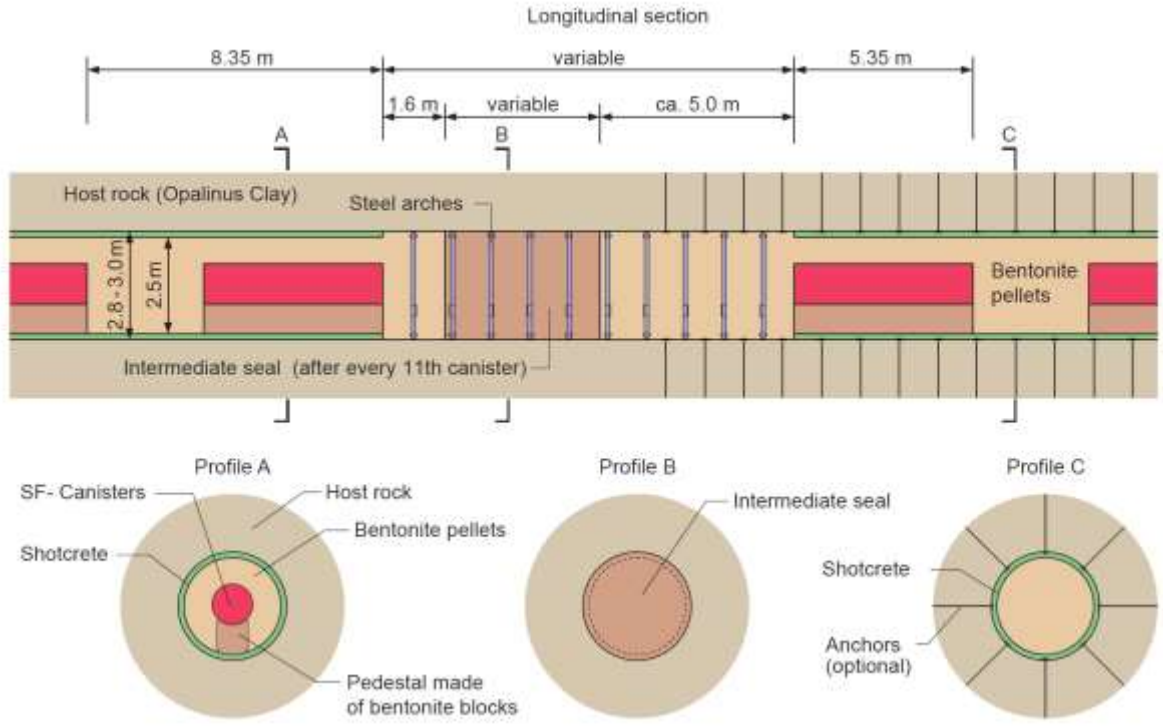

Figure 9-1: Conceptualization of the repository design for the high-level waste [1]

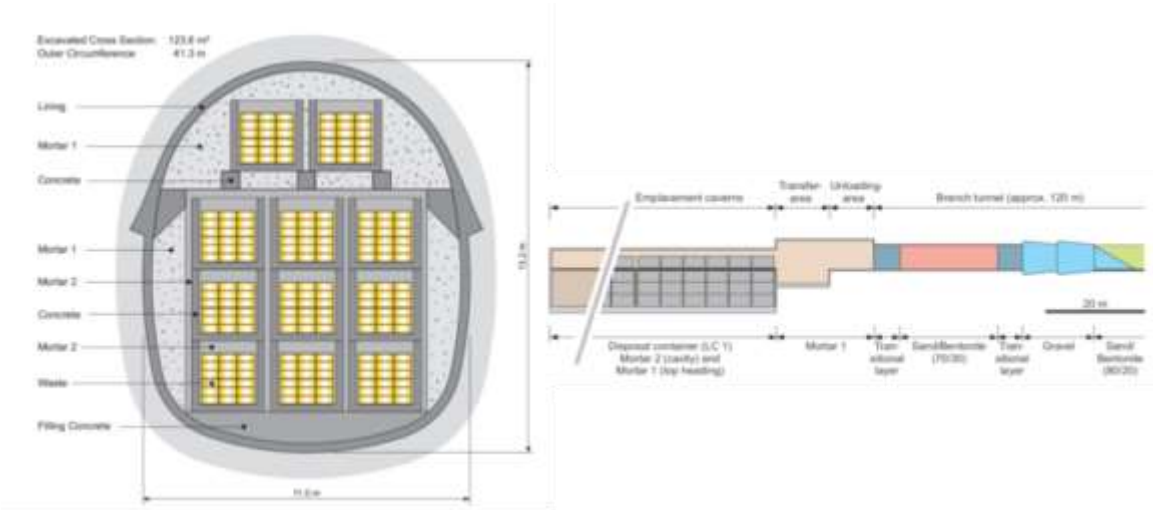

Figure 9-2: Cross section of a L/ILW repository emplacement cavern after closure (left) and possible design of the longitudinal section of the L/ILW emplacement cavern (right) [2]

9.2 Size of samples, concrete recipe

9.2.1 Introduction: Casting, curing and specimen preparation history

Within the scope of this study, concrete/mortar types used within the framework of the CI (Cement-clay Interface) experimental at the Mont Terri Underground Research Laboratory (URL) will be investigated. Within the scope of the CI experiment, the chemical interactions between various cement types and bentonite or the OPA under in situ conditions have been investigated and characterized (for details regarding the CI experiment, see the review article by Mäder et al. [3]). For this purpose, various boreholes have been filled with various cement paste/mortar/concrete types, which have been sampled approximately every two years to investigate the extent of the cement-clay interactions.

Within the scope of the study for Task 2 of the MAGIC WP, 5 distinct concrete/mortar types are going to be investigated, with distinct mix designs and age but sharing common features.

For each concrete/mortar type investigated, the respective specimens will be/are cored out of larger material volumes originally cast within plastic barrels as experimental model specimens for the CI campaign itself and based upon the same cementitious components as employed within the scope of the CI campaign.

Each barrel was originally filled at its bottom with the concrete/mortar type up to a certain height, e.g., 30 cm, to create a bottom layer. At least 28 days afterwards, a core of OPA (the host rock at Mt. Terri and the envisaged host rock for the Swiss nuclear waste repository), with diameter of about 284 mm and variable length, obtained from the two boreholes of the CI campaign, was positioned approximately in the center and on the cast bottom layer. The volume surrounding such OPA core was then filled with a new batch of the same concrete/mortar type, up to the barrel's top. The key feature is that the cementitious material was the same as emplaced in the CI experiment. After completing the casting, the barrel was closed with its plastic lid (thus not air-tight sealed).

Such barrels were produced within the CI campaign to realize simplified model systems of the OPA-concrete or OPA-mortar interfaces, being them more easily accessible for sampling than the actual, corresponding interfaces realized in the rock laboratory by filling the two boreholes of the campaign with the distinct concrete/mortar types.

The barrels were filled either in 2007 or in 2012, at distinct stages of the CI campaign (started in 2007). They were either 120 or 60 L in volume. Each barrel was filled with a distinct concrete/mortar type, as employed in the CI experiment. The actual details for each barrel are provided below. The main motivation for casting barrels with mortars, instead of only concrete, stemmed from difficulties encountered when analysing cores of the actual interface systems in the rock laboratory obtained from the first sampling campaign in 2009. The difficulties mainly consisted of reduced surface available, on polished cross-sections or on thin-sections, for chemical and mineralogical analysis of cement paste regions, due to the presence of the coarse aggregates.

Common to each barrel were the boundary conditions and the specimen coring protocols.

All the barrels were stored up to 2018 at the Mt. Terri Laboratory, in the same tunnel where the CI campaign's boreholes (named BCI-6 and BCI-7, see Figure 9-1 in 3 for their locations at the CI experimental site) are located. In 2018, the barrels were moved to NAGRA's storage site in Mellingen (Switzerland). At the Mt. Terri Laboratory tunnel, the average RH and temperature were 45-65% and 21°C, respectively. At the NAGRA's Mellingen storage site, ambient conditions were the norm.

In July 2021, the barrels were moved to Empa and stored also at ambient conditions, similarly as done at NAGRA's storage site, all the time, except during transportation to Empa's Center for X-ray Analytics for preliminarily locating within the barrel the vertical position of the OPA core. The latter was performed by high energy X-ray tomography (see Figure 9-3 and Figure 9-4).

After such location, the top and bottom parts of each barrel, not containing the OPA core, thus containing only concrete/mortar far away from it, were sliced off (see Figure 9-5) in August 2021 in order to provide access to surfaces where the OPA core was visible and where the actual concrete specimens could be cored out/cut out.

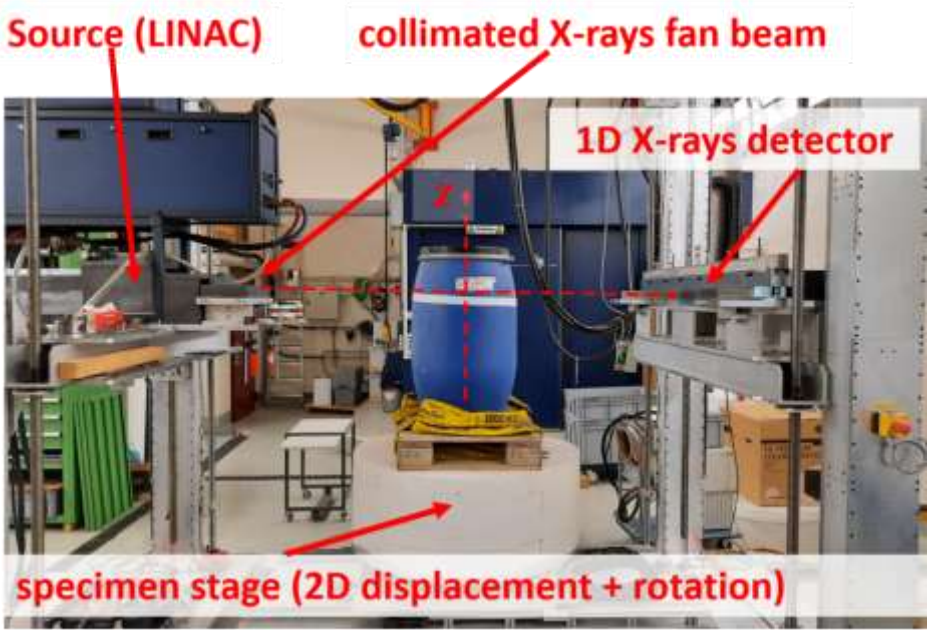

Figure 9-3: Example of the high energy X-ray tomography measurements configuration, which were performed on the barrels to approximately locate the position of the Opalinus Clay (OPA) core embedded in the cast concrete/mortar. The X-ray beam, produced by a compact linear electron accelerator (LINAC), was collimated to produce a so-called fan beam, which irradiates the investigated object only at one position along its vertical height (Z-axis in the photo). X-ray tomography was performed, for each barrel, only at three heights along such direction, thus producing only three 2D cross-sectional images (tomographic slices). Such slices provided the internal reconstruction of the barrel at the respective heights. The photon beam energy was 6 Mev. The pixel size of each tomographic slice was 0.2 mm.

The coring/cutting of the specimens with distinct shape and size mentioned in the following took place in August/September 2021. Between the barrels' slicing-off and such coring/cutting, the sliced barrels were stored in a climatic chamber at 70% RH and 20°C to avoid as much as possible drying and respective eventual shrinkage cracking of the concrete/mortar volumes.

The coring/cutting of the specimens of each barrel took place at distinct distances from the interface with the OPA core (see Figure 6 for an example) in order to sample from concrete/mortar regions which might have distinct microstructural properties because of their interactions with the OPA pore-water 3–5. The choice of the specimens' positions was mainly based on (1) sampling at as many distances as possible and (2) avoiding regions containing visible cracks. The possible distances between the center of each cylindrical core/prismatic cut specimen and the OPA core's boundary were chosen systematically but slightly varied depending on the barrel type and state (e.g., presence of cracks on the accessible surface) of the concrete/mortar regions. Given a barrel, its specimens were labelled according with the scheme XY, where X=A,B,C,… corresponds to a typical distance of the specimen's center from the concrete(mortar)/OPA core interface and Y=1,2,3,… is a non-negative integer index enumerating the specimens at such typical distance, distributed around the OPA core. See Figure 6 for an example of such specimen labeling for one barrel. The outermost (along the radial direction) specimens were always cored/cut at about 10 mm away from the barrel's external surface, to avoid to sample from regions affected by boundary effects, e.g., inhomogeneous aggregate packing, and to avoid specimen perturbation by the coring/cutting itself.

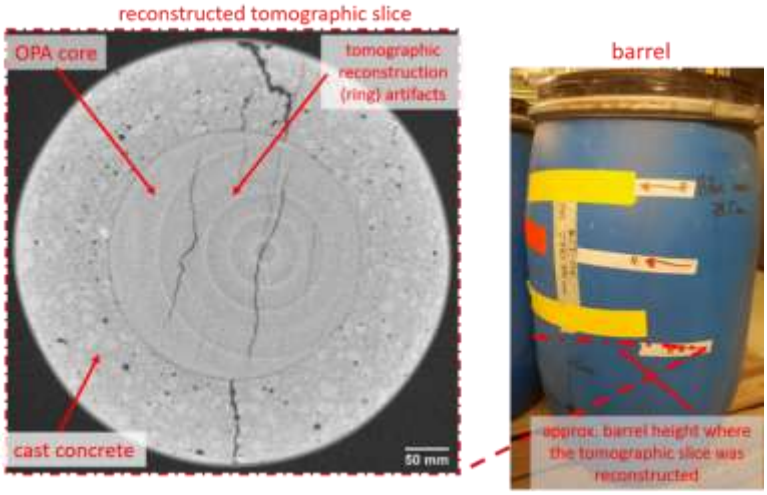

Figure 9-4: An example of results from high energy X-ray tomography of the barrels. The image on the left side shows one tomographic slice acquired for the barrel of the interface system 2276 (photograph on the right side, see below for that barrel's details), where the OPC concrete was cast around the Opalinus Clay (OPA) core. The horizontal dashed red line in the photograph on the right provides an indication of the barrel's height at which the slice on the left was reconstructed by high energy X-ray tomography. The pixel size of the tomographic slices was always 0.2 mm. Brighter grey pixels indicate higher local X-ray attenuation, due to either higher local mass density or higher local effective atomic number or a combination of the two. The bright, concentric rings in the slice are tomographic reconstruction artefacts, called ring artefacts, stemming from defective X-ray detector's pixels.

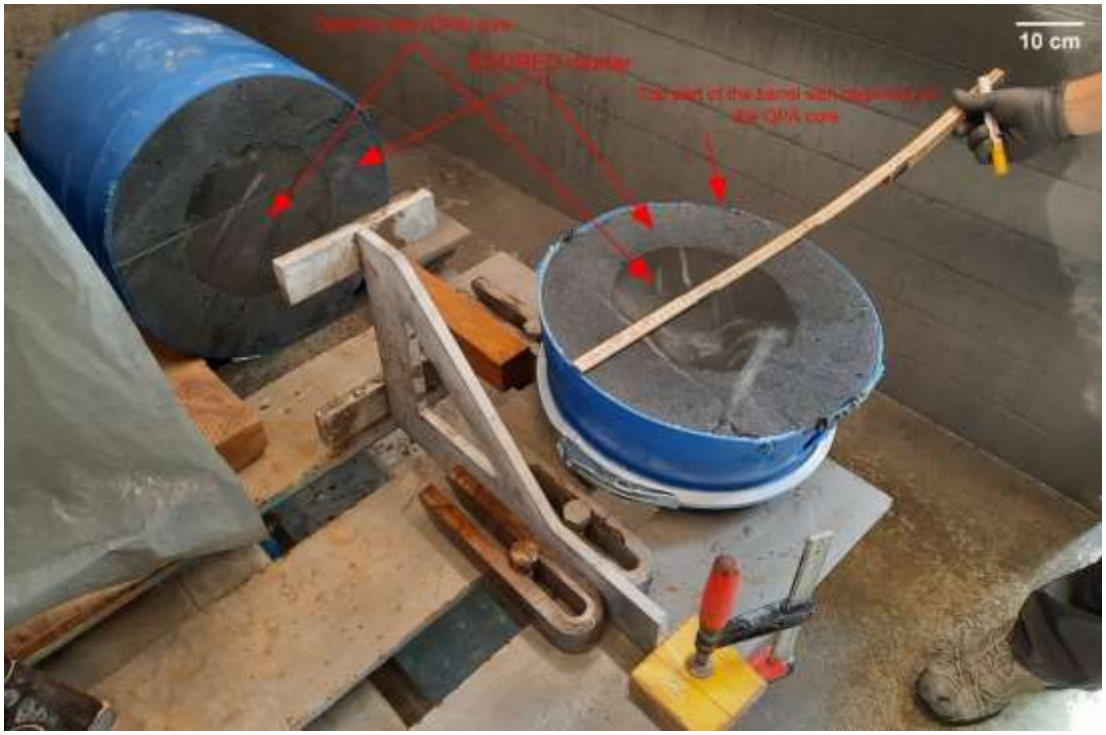

Figure 9-5: Example of slicing off of the top part of a barrel, containing only/mainly concrete/mortar, to provide access for coring/cutting specimens in the concrete/mortar volume and surrounding the Opalinus Clay (OPA) core. The barrel in this case was the one containing the interface system 2278 (ESDRED mortar/OPA interface) described below.

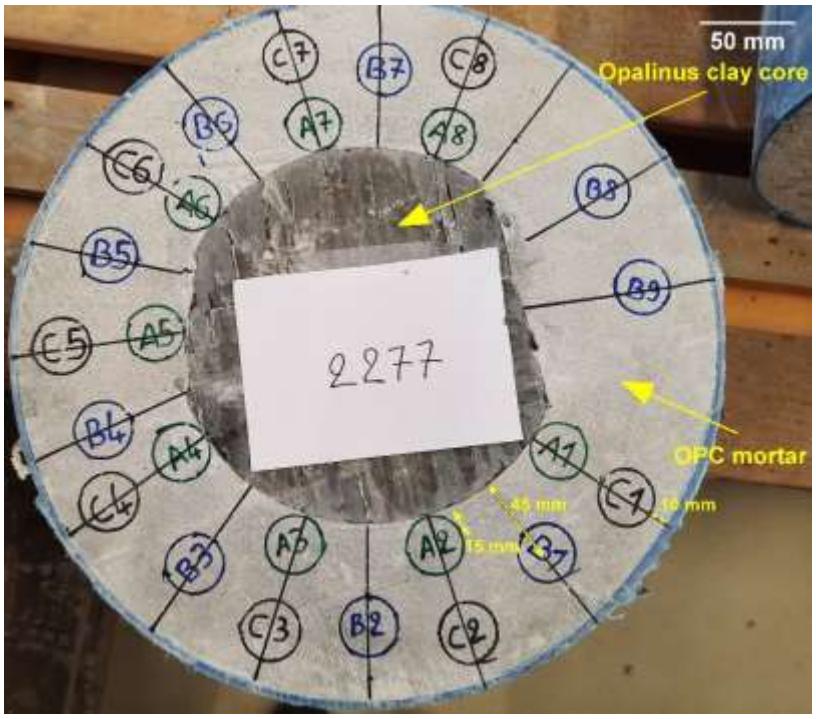

Figure 9-6: Example of choice of locations for specimen coring from one sliced-off barrel and of respective specimen labeling scheme. The barrel was the one of the interface system 2277 (OPC mortar/Opalinus Clay (OPA) core, see details below). The locations labelled as AY, ∀ Y=1,2,…, were for cylindrical cores of 28 mm diameter directly close to the interface. The locations labelled as BY, ∀ Y=1,2,…, are for 28 mm-diameter cores whose centers were about 45 mm away from the interface. The CY, ∀ Y=1,2,…, labelled locations were also for 28 mm-diameter cores 10 mm away from the barrel's external boundary and with center about 60-65 mm far away from the interface.

The cored/cut specimens were then packed in sealed plastic bags and stored in a climatic chamber at 90% RH and 20°C, to avoid as much as possible both carbonation and drying shrinkage-induced cracking, respectively. They will be removed from such chamber and unpacked only for the respective measurements on them.

We remark that both the slicing-off of the top and bottom parts of the barrels as well as the coring/cutting of the actual specimens were performed with water as lubricant. Ideally, the use of water during both operations should have been avoided, in order not to perturb the microstructural state of the concrete/mortar. However, that was not feasible at all during the slicing-off of the top/bottom parts of the barrels, given the large volume of concrete/OPA core to be cut through. Concerning the coring/cutting of the final specimens, the operation was first tested without using water. Some of the respectively cored specimens exhibited aggregates removal and signs of core surface wear. Thus, we decided to use water during such procedure to minimize the risk of such spurious perturbation on the specimens. We considered such risk more important to be avoided than the risk of microstructural changes due to, e.g., hydration of left clinker grains, given the concrete/mortar ages (14 and 9 years, respectively).

9.2.2 Mix design and detailed history of each barrel

Interface system 2274 (ESDRED concrete, 14 years old)

Barrel information:

The barrel had a volume of 120 L and contained an OPA core about 300 mm-long and about 284 mm in diameter. Such core was obtained from the drilling of the BCI-6 vertical borehole of the CI campaign (see again Fig. 1 in [3] for the location of such vertical borehole at the CI experimental site). It was the borehole segment at a depth between 615 and 645 cm from the floor of the tunnel.

The plastic barrel was first filled in March 2007 with the chosen concrete, up to a height of about 30 cm. In April 2007, the OPA core was positioned and the rest of the barrel's volume was filled with the chosen concrete.

Table 9-1: Mix design [4]; Water-to-binder ratio (w/b): 0.5

Component	Type	kg·m^{-3} for each component
Cement	CEM I 42.5 N ("Normo 4" by Holcim Switzerland)	210
Supplementary Cementitious Material (SCM)	Silica fume ("SikaFume HR/TU" by Sika Switzerland), 100 nm average grain diameter	140
Water	Tap water	175
Aggregate	Rounded river sediment, 0 – 8 mm sieve size range	1800
Additive/Admixture 1	Superplasticizer ("Glenium C321" by Degussa Switzerland)	4.2
Additive/Admixture 2	Accelerator ("Sigunit L53 AF" by Sika Switzerland)	16.8

Table 9-2: Specimen size and Nr. of specimens per size

Specimen shape	Specimen size	Nr.	Target measurement(s)
Cylindrical core	40 mm Ø,≈221 mm length	6	Dynamic linear Young modulus ($E^{dyn}{}_{lin}$), longitudinal linear Q^{-1}, all by Single Mode linear Resonant Ultrasound Spectroscopy (SIMORUS), nonlinear Young modulus ($E^{dyn}{}_{nonlin}$) by nonlinear SIMORUS (in short SIMONRUS), X-ray tomography
Cylindrical core	40 mm Ø,≈221 mm length	6	Dynamic shear modulus ($G^{dyn}{}_{lin}$), shear linear Q^{-1}, all from SIMORUS measurements, X-ray tomography
Cylindrical core	40 mm Ø,≈80 mm length	6‡	Uniaxial compressive strength (f_c)
Cylindrical core	40 mm Ø,≈120 mm length	6•	Quasi-static linear Young modulus ($E^{qs}{}_{lin}$)
Cylindrical core	10 mm Ø,≈40 mm length	3	X-ray tomography

‡ Specimens to be obtained from those used for the dynamic shear modulus measurements by cutting smaller segments, when not possible to be directly cored out of the barrel.

• Specimens to be obtained from those used for the dynamic Young modulus measurements by cutting smaller segments, when not possible to be directly cored out of the barrel.

Table 9-3: Average distance from the concrete/OPA core interface

Average distance [mm]◊	Nr. of specimens
20	6
50 – 65	6

◊ Nominal/approximate distance between the center of the specimen and the concrete/OPA core interface. For each cored specimen, the exact distance will be measured and provided in the results.

Interface system 2275 (LAC concrete, 14 years old)

Barrel information:

This barrel also had a volume of 120 L and contained an OPA core about 350 mm-long and about 284 mm in diameter. Such core was also obtained from the drilling of the BCI-6 vertical borehole. It was the borehole segment at a depth between 558 and 593 cm from the floor of the tunnel.

This plastic barrel was filled at the same time as the 2274 one, following a similar protocol (bottom layer cast in March 2007, positioning of the OPA core and casting of the concrete around it in April 2007).

Table 9-4: Mix design [4]; water-to-binder ratio (w/b): 1.08

Component	Type	kg·m^{-3} for each component
Cement	CEM III/B 42.5 L ("Juranit" by Jura Cement Switzerland)	206
Additional Supplementary Cementitious Material (SCM)	Nanosilica ("Aerosil 200" by Degussa Switzerland), 12 nm average grain diameter	22.9
Water	Tap water	247
Aggregate 1	Rounded river sediment, 0 – 16 mm sieve size range	1704
Additive	Superplasticizer ("Glenium C321" by Degussa Switzerland)	6

Table 9-5: Specimen size and Nr. of specimens per size

Specimen shape	Specimen size	Nr.	Target measurement(s)
Cylindrical core	40 mm Ø,≈221 mm length	6	Dynamic linear Young modulus ($E^{dyn}{}_{lin}$), longitudinal linear Q^{-1}, all by SIMORUS, nonlinear Young modulus ($E^{dyn}{}_{nonlin}$) by SIMONRUS, X-ray tomography
Cylindrical core	40 mm Ø,≈221 mm length	6	Dynamic shear modulus ($G^{dyn}{}_{lin}$), shear linear Q^{-1}, all by SIMORUS, X-ray tomography
Cylindrical core	40 mm Ø,≈80 mm length	6‡	Uniaxial compressive strength (f_c)
Cylindrical core	40 mm Ø,≈120 mm length	6•	Quasi-static linear Young modulus ($E^{qs}{}_{lin}$)
Cylindrical core	10 mm Ø,≈40 mm length	3	X-ray tomography

‡ Specimens to be obtained from those used for the dynamic shear modulus measurements by cutting smaller segments, when not possible to be directly cored out of the barrel.

• Specimens to be obtained from those used for the dynamic Young modulus measurements by cutting smaller segments, when not possible to be directly cored out of the barrel.

Table 9-6: Average distance from the concrete/OPA core interface

Average distance [mm]◊	Nr. of specimens
20	6
50 – 65	6

◊ Nominal/approximate distance between the center of the specimen and the concrete/OPA core interface. For each cored specimen, the exact distance will be measured and provided in the results.

Interface system 2276 (OPC concrete, 14 years old)

Barrel information:

This barrel had a volume of 120 L as the previous two ones. It contained an OPA core about 350 mm-long and about 284 mm in diameter. The OPA core in this barrel was also obtained from the drilling of

the BCI-6 vertical borehole. It was the borehole segment at a depth between 275 and 310 cm from the tunnel's floor.
This barrel was also filled at the same time and similarly for the previous two ones.

Table 9-7: Mix design§; Water-to-binder ratio (w/b): 0.8

Component	Type	kg·m^{-3} for each component
Cement	CEM I 42.5 R HS ("Protego 4R" by Holcim Switzerland)	238
Water	Tap water	190
Aggregate	Rounded river sediment, 0 – 16 mm sieve size range	1904

§ The mix design is provided in one of the technical reports of the CI experimental campaign, accessible only to the partners of the consortium running the campaign.

Table 9-8: Specimen size and Nr. of specimens per size

Specimen shape	Specimen size	Nr.	Target measurement(s)
Cylindrical core	40 mm Ø,≈221 mm length	6	Dynamic linear Young modulus ($E^{dyn}{}_{lin}$), longitudinal linear Q^{-1}, all by SIMORUS, nonlinear Young modulus ($E^{dyn}{}_{nonlin}$) by SIMONRUS, X-ray tomography
Cylindrical core	40 mm Ø,≈221 mm length	6	Dynamic shear modulus ($G^{dyn}{}_{lin}$), shear linear Q^{-1}, all by SIMORUS, X-ray tomography
Cylindrical core	40 mm Ø,≈80 mm length	6‡	Uniaxial compressive strength (f_c)
Cylindrical core	40 mm Ø,≈120 mm length	6•	Quasi-static linear Young modulus ($E^{qs}{}_{lin}$)
Cylindrical core	10 mm Ø,≈40 mm length	3	X-ray tomography

‡ Specimens to be obtained from those used for the dynamic shear modulus measurements by cutting smaller segments, when not possible to be directly cored out of the barrel.
• Specimens to be obtained from those used for the dynamic Young modulus measurements by cutting smaller segments, when not possible to be directly cored out of the barrel.

Table 9-9: Average distance from the concrete/OPA core interface

Average distance [mm]◊	Nr. of specimens
20	6
50 – 65	6

◊ Nominal/approximate distance between the center of the specimen and the concrete/OPA core interface. For each cored specimen, the exact distance will be measured and provided in the results.

Interface system 2277 (OPC mortar, 9 years old)

Barrel information:

This barrel had a smaller volume (60 L) compared to the three previous ones. It was filled during the 2nd sampling campaign in winter 2012 at the CI experiment site. It contained an OPA core about 200 mm-long and about 284 mm in diameter, being the segment at a depth between 360 and 380 cm from the tunnel's floor of the whole core obtained from the sampling, inclined borehole BCI-13 (see again Figure 9-1 in [3] for the location of such borehole at the CI experiment site).

Table 9-10: Mix design†; water-to-binder ratio (w/b): 0.47; fresh mass density (kg m^{-3}): 2050

Component	Type	kg·m^{-3} for each component
Cement	CEM I 42.5 N ("Normo 4" by Holcim Switzerland)	899
Water	Tap water	423
Aggregate	Sand, 0.1 – 0.3 mm sieve size range	728

† The mix design is provided in one of the technical reports of the CI experimental campaign, accessible only to the partners of the consortium running the campaign.

Table 9-11: Specimen size and Nr. of specimens per size

Specimen shape	Specimen size	Nr.	Target measurement(s)
Cylindrical core	28 mm Ø,≈155 mm length	9	Dynamic linear Young modulus ($E^{dyn}{}_{lin}$), longitudinal linear Q^{-1}, all by SIMORUS, nonlinear Young modulus ($E^{dyn}{}_{nonlin}$) by SIMONRUS, X-ray tomography
Cylindrical core	28 mm Ø,≈155 mm length	9	Dynamic shear modulus ($G^{dyn}{}_{lin}$), shear linear Q^{-1}, all by SIMORUS, X-ray tomography
Cylindrical core	28 mm Ø,≈56 mm length	9‡	Uniaxial compressive strength (f_c)
Cylindrical core	28 mm Ø,≈84 mm length	9•	Quasi-static linear Young modulus ($E^{qs}{}_{lin}$)
Cylindrical core	10 mm Ø,≈40 mm length	3	X-ray tomography

‡ Specimens to be obtained from those used for the dynamic shear modulus measurements by cutting smaller segments, when not possible to be directly cored out of the barrel.

• Specimens to be obtained from those used for the dynamic Young modulus measurements by cutting smaller segments, when not possible to be directly cored out of the barrel.

Table 9-12: Average distance from the concrete/OPA core interface

Approximate distance [mm]◊	Nr. of specimens
15	6
40 – 45	6
50 – 60	6

◊ Nominal/approximate distance between the center of the specimen and the mortar/OPA core interface. For each cored specimen, the exact distance will be measured and provided in the results.

Interface system 2278 (ESDRED mortar, 9 years old)

This barrel also had a volume of 60 L. It was filled simultaneously to the 2277 one, during the 2nd sampling campaign in winter 2012 at the CI experiment site. It contained an OPA core about 200 mm-long and about 284 mm in diameter, being the segment at depth between 340 cm and 360 cm of the same long core extracted from the same sampling borehole BCI-13.

Table 9-13: Mix design†; water-to-binder ratio (w/b): 0.5; fresh mass density (kg m^{-3}): 1860

Component	Type	kg·m^{-3} for each component
Cement	CEM I 42.5 N ("Normo 4" by Holcim Switzerland)	495
Supplementary Cementitious Material (SCM)	Silica fume ("SikaFume HR/TU" by Sika Switzerland), 100 nm average grain diameter	332
Water	Tap water	411
Aggregate	Sand, 0.1 – 0.3 mm sieve size range	573
Additive 1	Superplasticizer ("ACE 331" by BASF)	9.7
Additive 2	Accelerator ("Sigunit L53 AF" by Sika Switzerland)	40

† The mix design is provided in one of the technical reports of the CI experimental campaign, accessible only to the partners of the consortium running the campaign.

Table 9-14: Specimen size and Nr. of specimens per size

Specimen shape	Specimen size	Nr.	Target measurement(s)
Cylindrical core	28 mm Ø,≈155 mm length	9	Dynamic linear Young modulus ($E^{dyn}{}_{lin}$), longitudinal linear Q^{-1}, all by SIMORUS, nonlinear Young modulus ($E^{dyn}{}_{nonlin}$) by SIMONRUS, X-ray tomography
Cylindrical core	28 mm Ø,≈155 mm length	9	Dynamic shear modulus ($G^{dyn}{}_{lin}$), shear linear Q^{-1}, all by SIMORUS, X-ray tomography
Cylindrical core	28 mm Ø,≈56 mm length	9‡	Uniaxial compressive strength (f_c)
Cylindrical core	28 mm Ø,≈84 mm length	9•	Quasi-static linear Young modulus ($E^{qs}{}_{lin}$)
Cylindrical core	10 mm Ø,≈40 mm length	3	X-ray tomography

‡ Specimens to be obtained from those used for the dynamic shear modulus measurements by cutting smaller segments, when not possible to be directly cored out of the barrel.

• Specimens to be obtained from those used for the dynamic Young modulus measurements by cutting smaller segments, when not possible to be directly cored out of the barrel.

Table 9-15: Average distance from the concrete/OPA core interface

Average distance [mm]◊	Nr. of specimens
15	6
40 – 45	6
47 – 55	6

◊ Nominal/approximate distance between the center of the specimen and the mortar/OPA core interface. For each cored specimen, the exact distance will be measured and provided in the results.

9.3 Available characterisation of cementitious material

9.3.1 Poromechanics

9.3.1.1 Compressive strength

The 90-day compressive strength was measured according to the SN EN 12390-3 standard on additional three cubic (150 × 150 × 150 mm^3) specimens cast on the same dates when the barrels were filled but stored in a testing laboratory environment, under water at a temperature of about 20°C. The values were provided in a technical note accessible only to the partners of the CI experimental campaign. The average value from the three tested specimens is reported in Table 9-16.

Such measurements were performed only for the concretes used in the interface systems 2274, 2275 and 2276, produced in 2007. Corresponding measurement results for the mortars cast in 2012 to manufacture the interface systems 2277 and 2278 could not be retrieved.

Table 9-16: 90-day compressive strength of the same type of concrete cast in the barrels, as reported in a technical note accessible only to the CI campaign's partners. The average of three values measured on respective specimens and according to the SN EN 12390-3 standard was reported in such technical note.

Concrete type	90-day compressive strength [MPa]
ESDRED (interface system 2274)	79.2
LAC (interface system 2275)	33.7
OPC (interface system 2276)	29.7

9.3.1.2 Young's modulus

No data about quasi-static Young's modulus measurements could be found for any of the cementitious materials used to manufacture the interface systems.

9.3.1.3 Porosity

No porosity measurement has been so far performed on specimens either obtained from the same barrels as those used for the MAGIC Task 2 or from similar barrels.

However, local porosity measurements were performed on concrete/OPA clay interfaces obtained from actual on site cores. Such cores were acquired in 2012 via the CI campaign's sampling boreholes BC-13, BCI-14 and BCI-15 (see Fig.1 in [3]). These cores contained LAC concrete/OPA, ESDRED concrete/OPA and OPC concrete/OPA interfaces, respectively. The respective concretes were cast in 2007 within the vertical boreholes BCI-7 (LAC/OPA and ESDRED/OPA interfaces, respectively) and BCI-6 (OPC/OPA interface). They had the same mix designs as the respective concretes cast at the same time in the 120 L barrels used for this MAGIC Task 2. Thus, such cores were 5 years old and were the actual on site interface systems to be mimicked by those realized in the barrels.

Local porosity measurements were performed by Lerouge et al. for regions across each interface type by using the ^{14}C MMA autoradiography methodology 6. Data for the LAC concrete/OPA interface are publicly available in 7, while data for the other two interface types are provided only in technical reports available to the CI campaign's partners. All the reported data for the concrete sides of those 3 interface types are provided in Table 9-17. It has to be reminded and remarked that (1) such local porosity values refer to the cement paste/mortar matrix regions, since aggregates (fine or coarse) typically do not get impregnated by the ^{14}C-labelled MMA, thus they do not contribute to the autoradiographs' pixel values, and (2) the pixel size of such autoradiographs was 10.4 × 10.4 μm^2 [7].

No pore size distribution measurements, e.g., obtained by MIP or gas adsorption-based methods has ever been reported for these concrete types, either from actual on site cored specimens or from specimens cored from the model systems cast in the barrels.

Table 9-17: Local porosity values of the three distinct concrete types as measured by ^{14}C MMA-based autoradiography for regions at distinct average distances from the concrete/OPA interfaces. Adaptation from [7] and from a technical report of the CI experimental campaign available only to the campaign's partners.

Concrete type of the interface	Spatial location of the measurement	Local porosity [%]□
LAC	Whole concrete region available in the thin section	24
	5 mm from the interface	74
	30 mm from the interface	52.7
ESDRED	Whole concrete region available in the thin section	24
	2 mm from the interface	52
	14 mm from the interface	52
OPC	Whole concrete region available in the thin section	29
	< 1 mm from the interface	71
	13 mm from the interface	76

□ Average value estimated for distinct regions as slightly different distances from the concrete/OPA interface. The average distance is provided in the mid column.

9.3.1.4 Mass density

Additional characterizations of the concrete types used to manufacture the interface systems 2274, 2275 and 2276 include 90-day measurements of mass density, performed according to the SN EN 12390-7 standard (see Table 9-18) on the same specimens used for the 90-day compressive strength measurements.

Table 9-18: 90-day mass density measurements performed according to the SN EN 12390-7 standard on the same specimens used for the 90-day compressive strength measurements. Since such specimens were stored for 90 days under water, the measured values refer to a water-saturated state. The values are the average ones from the three distinct specimens, for each concrete type. They were documented in a technical report available only to the partners of the CI experimental campaign.

Concrete type	90-day mass density [kg·m^{-3}]
ESDRED (interface system 2274)	2250
LAC (interface system 2275)	2220
OPC (interface system 2276)	2360

9.3.2 Chemistry

9.3.2.1 Mineralogy

The chemical and mineralogical characterizations of the concrete side of the interface have been the most extensive ones performed on such interface systems. They have been mainly performed for actual on site interface systems obtained from specimens cored via boreholes. They have relied on a very broad palette of analytical (spectroscopic and not) and microscopy approaches including:

SEM performed in back-scatter mode + EDX analysis (both mapping and point analysis) [3,4,7,8]

- Reflective optical microscopy of thin sections [3,4,7]
- Electron Probe Micro-Analysis (EPMA) [3,7]
- Raman spectroscopy [4,7]
- Infrared (IR) spectroscopy [3,4,7,8]
- Micro-X-ray fluorescence analysis (µ-XRF) [7]
- Powder XRD [7,8] and synchrotron micro-XRD (µ-XRD) [9,10]
- Solid state NMR spectroscopy, e.g., ^{29}Si MAS NRM [7,8]
- Thermo-gravimetric analysis (TGA) [8]

The first investigations involved 2-year old interfaces [4] while more recent ones focused on 10-year old ones [10]. All the investigations performed so far focused on characterizing the mineralogical and

microstructural changes, both on the concrete and on the OPA sides, due to diffusion of ionic species across the interface and respective chemical reactions.

Concerning the concrete side of the interface, changes have been observed up to distances of several mm from the interface [3,4,7]. The exact extent of the modified concrete regions varied significantly depending upon the concrete type, age and feature variables used to characterize the changes. However, the characteristic length scale was within several mm in almost all cases.

Specific objects of investigation have been, among several, the following ones:

- The characterization of the regions with modified carbonate state [4];
- The identification and characterization of distinct and successive zones with altered chemical, mineralogical and pore space properties [3,4,7], including assessing their spatial extents;
- Among the chemical changes, the formation of M-S-H phases due to Mg species's migration from the clay side [3,4,7,8];
- The redistribution of sulphate-based species still within the concrete side of the interface, towards regions far away from the interface characterized by higher pH values [4].

Significant work has been also dedicated, along the way, to optimize analytical techniques for identifying the complex variety of phases resulting from the reactive transport of the clay pore water into the concrete region [9,10].

A unique pattern of phase dissolution/formation has not yet completely emerged and investigations on older age interface systems are planned for the future, with the overarching goal of supporting the formulation and validation of reactive transport computational model [3].

9.3.2.2 Pore-water chemistry

The pore solution's concentration for several ionic species (Ca^{2+}, Mg^{2+}, Na^{+}, K^{+}, SO_4^{-}, Cl^{-}, CO_3^{2-}) and its pH were measured for the LAC and ESDRED corresponding cement pastes by Lothenbach et al. 11,12 and summarized in Table 1 of [4] and Table 1 of [3]. The measurements were performed on model cement paste systems at distinct hydration ages spanning the range from 1 hour from casting up to about 4 years. The pore solution was obtained by vacuum or pressure filtration at an age of 1 day and by the steel die method [13] from hardened specimens at later ages. We remark that such model cement paste systems were not obtained by cutting/coring from larger volumes, with the simultaneous use of flushing water, as needed for the specimens to be investigated for MAGIC's Task 2.2. They were cast already with the appropriate size for the steel die method. Thus the pore solution's ionic concentration and pH analysis results were not biased by the interaction with additional, externally-supplied water. A similar pore solution's analysis cannot and will not performed on the MAGIC's Task 2.2 specimens, because of the risk of such bias. Inductive coupled plasma-based optical emission spectroscopy (ICP-OES) was then used on the extracted batches for concentration analysis, while pH measurements were performed with a Knick pH meter [11,12].

The pH of such pastes varied between a maximum of 13.3 (for the OPC paste at 4 years) to 11.7 (for the ESDRED paste at 4 years) (see Table 1 in [4]).

9.3.2.3 Other characterisations

No other chemical or textural characterization have been performed on the concrete side of the interfaces beyond those mentioned above.

No microbiology characterization was performed for any of the studied interface system, at any time.

9.4 Description of experimental set-up

As mentioned in paragraph 9.2, all the specimens are cores obtained from the experimental models of the actual in situ concrete/OPA interfaces studied in the ongoing CI experimental campaign at the Mt Terri Rock Laboratory. Overviews of the overall CI experimental campaign are provided in [3,4].

See paragraph 9.2 for a detailed explanation of the experimental models of the interfaces which are the sources of the specimens we use for MAGIC's Task 2 and how such cored specimens are obtained and stored till their characterizations.

9.5 Characterisation of cementitious material to be performed in MAGIC

9.5.1 Poromechanical characterisations

For each concrete/mortar type listed in paragraph 9.2, the same identical set of poromechanical characterizations is planned to be performed.

As described in paragraph 9.2, for each concrete/mortar type, coring positions were chosen at either two or three distinct average distances from the interface with the OPA core.

A key target of the characterizations is to assess any eventual dependence of poromechanical properties from the distance from the OPA core surface.

This analysis target is especially relevant for the 14-year old specimens (interface systems 2274, 2275 and 2276). Indeed, the data about corresponding in situ interface systems, so far published in the literature, indicate the existence of a highly heterogeneous spatial distribution of chemical and microstructural properties of the concrete side of the interfaces. Such distribution was shown to be a function of the distance from the interface even at ages earlier than 14 years [3,4,7]. The existing knowledge gaps concern whether such heterogeneous spatial distribution might mirror itself into changes of the macroscopic poromechanical properties as a function of the distance from the interface and, if yes, what are the degree and scale of such changes.

The minimum number of specimens for each characterization is indicated, for each concrete/mortar type, in paragraph 9.2. For each average distance from the interface, at least 3 specimens will be used for each characterization and, where possible, more than 3.

In addition to the specimens cored from the barrels belonging to the CI experimental campaign, new concrete/mortar specimens with the same mix designs described in paragraph 9.2 will be cast and used for determining bounds of the same poromechanical properties/parameters measured on the cores obtained from the barrels. The newly cast specimens will have the same shape and size as those cored from the barrels and will be subjected to the same storage boundary conditions. Such specimens could not play the role of actual reference specimens, given the different age. However, they could provide, as mentioned above, insight into bounds or range of values of the measured poromechanical properties for the same concrete/mortar type not being exposed at all to the OPA pore-water.

9.5.1.1 Dynamic and quasi-static linear (visco-)elastic moduli

We will measure the dynamic, linear Young ($E^{dyn}{}_{lin}$) and shear ($G^{dyn}{}_{lin}$) moduli (also called in rheology as storage moduli or real parts of the respective complex elastic moduli) as basic mechanical properties and to be used as well as damage proxy variables. "Damage" is here intentionally used with a broad meaning to indicate any meso- and microstructural alteration of the cementitious side of the interface systems, in respect to the state of the same cementitious materials far away from the interface.

We will use for these measurements SIngle MOde Resonant Ultrasound Spectroscopy (SIMORUS, in short), which is a special version of Resonant Ultrasound Spectroscopy (RUS), a non-destructive, elastic wave-based measurement method developed in Condensed Matter Physics and widely used in Mineral Physics for measuring the full elastic constant tensor of minerals [14–16]. SIMORUS consists of performing RUS measurements by exciting one vibration eigenmodes type of the specimen at a time and by using specimens with specific shapes and (large) aspect ratios. The latter features allow simplifying the solution of the inverse problem consisting of estimating the elastic constants from resonance frequencies measurements, by additionally knowing the specimen's mass density and shape/size. We will use the experimental configurations indicated by the ASTM C215-14 standard [17] for exciting

longitudinal and torsional eigenmodes (longitudinal and torsional SIMORUS) to measure $E^{dyn}{}_{lin}$ and $G^{dyn}{}_{lin}$,, respectively.

The Q-factor (in short Q) of the resonance curve of each vibration eigenmode type (longitudinal and torsional) will also be estimated given its direct relationship with the respective loss modulus (or imaginary part of the respective complex elastic modulus) 18, related with wave amplitude attenuation factor α of the material, defined as:

$$\alpha_i = \frac{2\pi}{Q \cdot \lambda_{i,j}}$$

where the index i indicates the vibration *eigen*mode type ($i = long$ or $i = tors$), the index j=1,2,… indicates the order of the vibration *eigen*mode of the given type i and $\lambda_{i,j}$ is the wavelength of the excited vibration eigenmode, being equal to a multiple of the specimen's length for elongated cylindrical specimens, the multiple factor being fixed for each specific eigenmode. α is related, among others, to the intrinsic viscosity properties of the materials [18]. As a proxy variable of wave amplitude attenuation, thus also of viscosity, we will directly report Q^{-1}. Both parameters and loss elastic moduli in general are more sensitive damage proxy variables than storage moduli, for concrete [19].

The SIMORUS measurements will be performed within a glove box (see Figure 9-7) conditioned at 90% RH and 20°C, in order to avoid, during the measurements themselves, any change of the specimens' water saturation degree. The latter is known to be a parameter significantly influencing both complex linear elastic moduli.

The two moduli will be measured on two distinct specimen sets given technical constraints on the implementation of the respective vibration sources.

The quasi-static linear Young modulus ($E^{qs}{}_{lin}$) will be measured according to an adaptation of the EN 12390-13 standard on a distinct set of specimens wherever a sufficient number of specimens could be cored out or, otherwise, on specimens obtained from cutting those used for the $E^{dyn}{}_{lin}$. The end goal is to have available sufficient data to establish a phenomenological mapping between the $E^{dyn}{}_{lin}$ values and the $E^{qs}{}_{lin}$ ones. Such mapping should then enable the comparison with quasi-static values measured by other MAGIC Task 2 participants. The main rationale for measuring dynamic values and not only quasi-static ones is that the measurement of the latter is not completely non-destructive [20–24], thus not allowing reliable time-lapse investigations, needed in case the same cored specimens would need to be subjected to laboratory-accelerated degradation, e.g., to sulfate attack testing or accelerated carbonation.

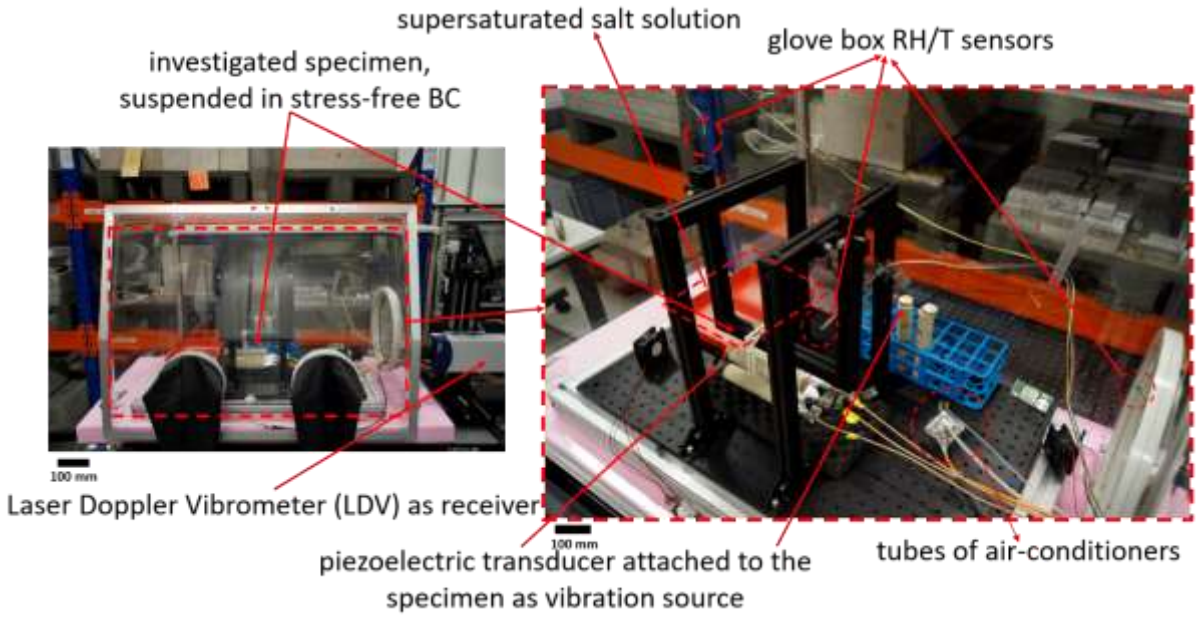

Figure 9-7: View of the setup for performing SIngle MOde linear and Nonlinear Resonant Ultrasound Spectroscopy (SIMO(N)RUS) measurements on rod-like (i.e., elongated) specimens under controlled temperature and relative humidity (RH) conditions. The specimen (in this example, a cylindrical Berea sandstone core, 28 mm in length, 150 mm in diameter) hangs on plastic supports located at the nodal regions for its 1st longitudinal vibration eigenmode, in order to realize stress-free boundary conditions (BC). It is excited by a piezoelectric disk attached to its bottom side. The corresponding vibration signal is measured in a non-contact way by a single point Laser Doppler Vibrometer (LDV). The specimen is located inside a glove box conditioned at a chosen RH value by the use of a respective supersaturated salt solution laid in containers and by additional, external air conditioners. The LDV is located outside of the glove box, its laser beam shining on the specimen's top surface through a small window on one side of the glove box.

9.5.1.2 Uniaxial compressive strength

We will perform uniaxial compressive strength measurements according with the EN 12504-1 standard on either additionally cored specimens or, wherever not available, on specimens derived from cutting those used for the $G^{dyn}{}_{lin}$ measurements. As indicated in the tables in paragraph 9.2, the specimens will have aspect ratio (diameter-to-length) equal to 2.

9.5.1.3 Dynamic nonlinear elastic moduli as damage proxy variables

On the same specimens subjected to the SIMORUS measurements, we will perform SIngle MOde Nonlinear RUS (SIMONRUS) to measure the respective nonlinear elastic moduli [25,26], which are known to be extremely more sensitive to damage than complex linear elastic moduli [27]. The latter feature has been shown for damage produced in concrete by the alkali-silica reaction (ASR) [28–36], carbonation [37–40], sulfate attack [41–43], thermal shocks [44–48], freeze-thaw cycles [41,49,50] and cracking induced by drying shrinkage [51–53].

SIMONRUS consists in performing multiple corresponding SIMORUS measurements at increasing strain wave amplitude, in order to study the dependence of the effective elastic moduli on the latter parameter, coded by the nonlinear elastic moduli. The SIMONRUS measurements will thus be performed in the same glove box used for the SIMORUS ones and will follow immediately the latter during the same measurement sessions. While performing SIMONRUS by exciting longitudinal vibration eigenmodes of elongated specimens is a consolidated practice, allowing estimating the dynamic nonlinear Young modulus $E^{dyn}{}_{nonlin}$, corresponding measurements with torsional vibration eigenmodes, to estimate the dynamic nonlinear shear modulus $G^{dyn}{}_{nonlin}$, are less conventional and

feasible. We will perform SIMONRUS measurement with both configurations, although we are cannot guarantee, for the time being, successful results for the estimation of $G^{dyn}{}_{nonlin}$.

The key goal of these SIMONRUS measurements is to obtain, by estimates of $E^{dyn}{}_{nonlin}$, and eventually also of $G^{dyn}{}_{nonlin}$, more sensitive indications of any eventual damage in specimens at distinct distances from the interface with the OPA cores.

9.5.1.4 Meso- and microstructural characterization by X-ray tomography analysis

X-ray tomography is planned to be performed on each specimen to be subjected to the SIMO(N)RUS measurements, in order to look for any mesoscale and microscale (up to the achievable tomographic spatial resolution, which, for such specimen, will range between 30 and 70 µm) structural differences between specimens at distinct distances from the interface with the OPA core.

These measurements will serve two purposes: (1) a qualitative assessment of the general mesostructure of the cored specimens, in order to exclude from the measurement campaign any specimen with eventual spurious damage, e.g., macroscopic cracks, likely not related with the chemical interaction of the cementitious material with the OPA core's pore-water; (2) a qualitative assessment of the local porosity spatial distribution, obtained via the 3D image analysis methodology described next.

We will perform X-ray tomography also on a smaller number of smaller cores (10 mm in diameter), sampled at distinct distances from the interface of the OPA core as well, for the same two purposes mentioned above but with the possibility of achieving for them higher (order of 10 µm) tomographic spatial resolution.

Independently of the specimen size, the tomograms will not cover the whole volume of each specimen, rather only a selected region of interest (ROI), due to lack of sufficient resources, which would be needed to tomograph any specimen along its entire length.

Qualitative local porosity spatial distribution analysis

Independently of the core diameter (40, 28 or 10 mm), the achievable tomographic spatial resolution in the respective tomograms will allow actual identification (segmentation, in image analysis jargon) of the largest pores within the cementitious matrix, e.g., air voids, porous patches and cracks with thickness/length larger than the spatial resolution. They contribute to a small fraction of the overall pore space. However, information about the unresolved part of the cementitious matrix's pore space is encoded in the spatial distribution of the tomogram's voxel values, with the cementitious matrix's more porous regions leading to smaller voxel values. Local, unresolved micro-cracks would also contribute to lower the voxel values of regions containing them, compared with less cracked regions.

We will perform a type of image analysis, belonging to the domain of texture analysis [54,55], which will allow evaluating the statistical distribution of voxel values by encoding also spatial information, in terms of size and orientation of zones with distinct voxel value ranges [56,57]. Such analysis could allow distinguishing between specimens, based upon different bulk texture properties, or, for a given specimen, between distinct regions, allowing thus to create a qualitative spatial map of local porosity. The target of this analysis is assessing the existence of any gradient in local porosity along, e.g., the radial direction of the barrel, i.e., at distinct distances from the interface with the OPA core.

9.5.1.5 Porosity and pore size distribution analysis

To complement and eventually validate the qualitative results from the texture analysis of the X-ray tomograms, we will perform Mercury Intrusion Porosimetry (MIP) on small batches of specimens obtained from coring out small plugs at identical distances from the interface with the OPA core where the larger cores for the ultrasound and X-ray tomography measurements. The aim is to estimate semi-quantitatively local porosity and pore size distribution of regions close-by those of the larger cores.

9.5.2 Chemical and mineralogical characterizations

While sampling for the MIP measurements, a rather limited number of small plugs will be cored out at identical distances from the interface with the OPA core in order to perform only some of the chemical/mineralogical characterizations listed in paragraph 9.3.2.1. They will include powder XRD analysis and Raman/FTIR spectroscopy. Larger cores (28 or 40 mm in diameter) will be drilled out at similar distances, as where the ultrasound/X-ray tomography cores were obtained, for SEM and EDX analysis of respective polished cross-sections. The main goal would be to complement the poromechanical knowledge, gathered by the ultrasounds and X-ray tomography measurements, with spatially resolved chemical and mineralogical data. The latter could be compared also with corresponding data for younger specimens already published in the literature.

9.6 Time plan vs delivered data/information

	June – Dec. 2021 (months 25 - 31)		Jan. – June 2022 (months 32 – 37)		July – Dec. 2022 (months 38 – 43)		Jan. – June 2023 (months 44 - 49)		July – Dec. 2023 (months 50 – 55)		Jan. – May 2024 (months 56 - 60)	
Exp. campaign design and specimen preparation												
Linear (visco-)elastic moduli				●					●			
Nonlinear elastic moduli					●					●		
X-ray tomography analysis				●						●		
Porosity and PSD¶ analysis						●				●		
Chemical and mineralogical characterizations					●					●		

●: point of delivery of data and their curation into the IDPC (Interactive Data Platform for Cement)
¶ PSD: Pore Size Distribution analysis by MIP measurements

9.7 References

(1) Leupin, O. X.; Smith, P.; Marschall, P.; Johnson, D.; Savage, D.; Cloet, V.; Schneider, J.; Senger, R. High-Level Waste Repository-Induced Effects; Nagra Technical Report; NTB-14-13; Nagra: Switzerland, 2014.

(2) Leupin, O. X.; Smith, P.; Marschall, P.; Johnson, P.; Savage, D.; Cloet, V.; Schneider, J.; Senger, R. Nagra Technical Report; NTB-14-14; Nagra: Switzerland, 2014.

(3) Mäder, U.; Jenni, A.; Lerouge, C.; Gaboreau, S.; Miyoshi, S.; Kimura, Y.; Cloet, V.; Fukaya, M.; Claret, F.; Otake, T.; Shibata, M.; Lothenbach, B. 5-Year Chemico-Physical Evolution of Concrete–Claystone Interfaces, Mont Terri Rock Laboratory (Switzerland). Swiss J. Geosci. 2017, 110, 307–327. https://doi.org/10.1007/s00015-016-0240-5.

(4) Jenni, A.; Mäder, U.; Lerouge, C.; Gaboreau, S.; Schwyn, B. In Situ Interaction between Different Concretes and Opalinus Clay. Phys. Chem. Earth Parts ABC 2014, 70–71, 71–83. https://doi.org/10.1016/j.pce.2013.11.004.

(5) Shafizadeh, A.; Gimmi, T.; Van Loon, L. R.; Kaestner, A. P.; Mäder, U. K.; Churakov, S. V. Time-Resolved Porosity Changes at Cement-Clay Interfaces Derived from Neutron Imaging. Cem. Concr. Res. 2020, 127, 105924. https://doi.org/10.1016/j.cemconres.2019.105924.

(6) Pret, D. Nouvelles Méthodes Quantitatives de Cartographie de La Minèralogie et de La Porositè Dans Les Matériaux Argileux: Application Aux Bentonites Compactées Des Barrières Ouvragées. PhD Thesis, Univeristy of Poitiers, France, 2003.

(7) Lerouge, C.; Gaboreau, S.; Grangeon, S.; Claret, F.; Warmont, F.; Jenni, A.; Cloet, V.; Mäder, U. In Situ Interactions between Opalinus Clay and Low Alkali Concrete. Phys. Chem. Earth Parts ABC 2017, 99, 3–21. https://doi.org/10.1016/j.pce.2017.01.005.

(8) Dauzeres, A.; Achiedo, G.; Nied, D.; Bernard, E.; Alahrache, S.; Lothenbach, B. Magnesium Perturbation in Low-PH Concretes Placed in Clayey Environment—Solid Characterizations and Modeling. Cem. Concr. Res. 2016, 79, 137–150. https://doi.org/10.1016/j.cemconres.2015.09.002.

(9) Dähn, R.; Popov, D.; Schaub, Ph.; Pattison, P.; Grolimund, D.; Mäder, U.; Jenni, A.; Wieland, E. X-Ray Micro-Diffraction Studies of Heterogeneous Interfaces between Cementitious Materials and Geological Formations. Phys. Chem. Earth Parts ABC 2014, 70–71, 96–103. https://doi.org/10.1016/j.pce.2013.10.010.

(10) Bernard, E.; Jenni, A.; Fisch, M.; Grolimund, D.; Mäder, U. Micro-X-Ray Diffraction and Chemical Mapping of Aged Interfaces between Cement Pastes and Opalinus Clay. Appl. Geochem. 2020, 115, 104538. https://doi.org/10.1016/j.apgeochem.2020.104538.

(11) Lothenbach, B.; Le Saout, G.; Ben Haha, M.; Figi, R.; Wieland, E. Hydration of a Low-Alkali CEM III/B–SiO2 Cement (LAC). Cem. Concr. Res. 2012, 42 (2), 410–423. https://doi.org/10.1016/j.cemconres.2011.11.008.

(12) Lothenbach, B.; Rentsch, D.; Wieland, E. Hydration of a Silica Fume Blended Low-Alkali Shotcrete Cement. Phys. Chem. Earth Parts ABC 2014, 70–71, 3–16. https://doi.org/10.1016/j.pce.2013.09.007.

(13) Longuet, P.; Burglen, L.; Zelwer, A. La Phase Liquide Du Ciment Hydraté. Rev. Matér. Constr. 1973, 676, 35–41.

(14) Migliori, A.; Sarrao, J. L. Resonant Ultrasound Spectroscopy. Applications to Physics, Materials Measurements, and Nondestructive Evaluation; John Wiley & Sons, Ltd: New York, NY, USA, 1997.

(15) Ulrich, T.; McCall, K. R.; Guyer, R. A. Determination of Elastic Moduli of Rock Samples Using Resonant Ultrasound Spectroscopy. J. Acoust. Soc. Am. 2002, 111 (4), 1667–1674. https://doi.org/10.1121/1.1463447.

(16) Zadler, B. J.; Le Rousseau, J. H. L.; Scales, J. A.; Smith, M. L. Resonant Ultrasound Spectroscopy: Theory and Application. Geophys. J. Int. 2004, 156 (1), 154–169. https://doi.org/10.1111/j.1365-246X.2004.02093.x.

(17) ASTM C09 Committee. Test Method for Fundamental Transverse, Longitudinal, and Torsional Resonant Frequencies of Concrete Specimens; Standard ASTM C215-14; ASTM International, 2014. https://doi.org/10.1520/C0215-14.

(18) Lakes, R. S. Chapter 3. Dynamic Behavior. In Viscoelastic materials; Cambridge University Press: Cambridge, 2009; pp 55–90.
(19) Saint-Pierre, F.; Rivard, P.; Ballivy, G. Measurement of Alkali–Silica Reaction Progression by Ultrasonic Waves Attenuation. Cem. Concr. Res. 2007, 37 (6), 948–956. https://doi.org/10.1016/j.cemconres.2007.02.022.
(20) Walsh, J. B. The Effect of Cracks on the Compressibility of Rock. J. Geophys. Res. 1965, 70 (2), 381–389. https://doi.org/10.1029/JZ070i002p00381.
(21) Walsh, J. B. The Effect of Cracks on the Uniaxial Elastic Compression of Rocks. J. Geophys. Res. 1965, 70 (2), 399–411. https://doi.org/10.1029/JZ070i002p00399.
(22) Batzle, M. L.; Simmons, G.; Siegfried, R. W. Microcrack Closure in Rocks under Stress: Direct Observation. J. Geophys. Res. 1980, 85 (B12), 7072. https://doi.org/10.1029/JB085iB12p07072.
(23) Nemati, K. M.; Monteiro, P. J. M.; Scrivener, K. L. Analysis of Compressive Stress-Induced Cracks in Concrete. ACI Mater. J. 1998, 95 (5). https://doi.org/10.14359/404.
(24) Nemati, K. M.; Monteiro, P. J. M.; Cook, N. G. W. A New Method for Studying Stress-Induced Microcracks in Concrete. J. Mater. Civ. Eng. 1998, 10 (3), 128–134. https://doi.org/10.1061/(ASCE)0899-1561(1998)10:3(128).
(25) Johnson, P.; Sutin, A. Slow Dynamics and Anomalous Nonlinear Fast Dynamics in Diverse Solids. J. Acoust. Soc. Am. 2005, 117 (1), 124–130. https://doi.org/10.1121/1.1823351.
(26) Bentahar, M.; El Aqra, H.; El Guerjouma, R.; Griffa, M.; Scalerandi, M. Hysteretic Elasticity in Damaged Concrete: Quantitative Analysis of Slow and Fast Dynamics. Phys. Rev. B 2006, 73 (1), 014116. https://doi.org/10.1103/PhysRevB.73.014116.
(27) Zaitsev, V. Y. Nonlinear Acoustics in Studies of Structural Features of Materials. MRS Bull. 2019, 44 (5), 350–360. https://doi.org/10.1557/mrs.2019.109.
(28) Chen, J.; Kim, J.-Y.; Kurtis, K. E.; Jacobs, L. J. Theoretical and Experimental Study of the Nonlinear Resonance Vibration of Cementitious Materials with an Application to Damage Characterization. J. Acoust. Soc. Am. 2011, 130 (5), 2728–2737. https://doi.org/10.1121/1.3647303.
(29) Jin, J.; Xi, W.; Riviere, J.; Shokouhi, P. Single-Impact Nonlinear Resonant Acoustic Spectroscopy for Monitoring the Progressive Alkali–Silica Reaction in Concrete. J. Nondestruct. Eval. 2019, 38 (3), 77. https://doi.org/10.1007/s10921-019-0614-5.
(30) Sargolzahi, M.; Kodjo, S. A.; Rivard, P.; Rhazi, J. Effectiveness of Nondestructive Testing for the Evaluation of Alkali–Silica Reaction in Concrete. Constr. Build. Mater. 2010, 24 (8), 1398–1403. https://doi.org/10.1016/j.conbuildmat.2010.01.018.
(31) Kodjo, A. S.; Rivard, P.; Cohen-Tenoudji, F.; Gallias, J.-L. Impact of the Alkali–Silica Reaction Products on Slow Dynamics Behavior of Concrete. Cem. Concr. Res. 2011, 41 (4), 422–428. https://doi.org/10.1016/j.cemconres.2011.01.011.
(32) Leśnicki, K. J.; Kim, J.-Y.; Kurtis, K. E.; Jacobs, L. J. Characterization of ASR Damage in Concrete Using Nonlinear Impact Resonance Acoustic Spectroscopy Technique. NDT E Int. 2011, 44 (8), 721–727. https://doi.org/10.1016/j.ndteint.2011.07.010.
(33) Leśnicki, K. J.; Kim, J.-Y.; Kurtis, K. E.; Jacobs, L. J. Assessment of Alkali–Silica Reaction Damage through Quantification of Concrete Nonlinearity. Mater. Struct. 2013, 46 (3), 497–509. https://doi.org/10.1617/s11527-012-9942-y.
(34) Ju, T.; Achenbach, J. D.; Jacobs, L. J.; Guimaraes, M.; Qu, J. Ultrasonic Nondestructive Evaluation of Alkali–Silica Reaction Damage in Concrete Prism Samples. Mater. Struct. 2017, 50 (1), 60. https://doi.org/10.1617/s11527-016-0869-6.
(35) Kim, G.; Giannini, E.; Klenke, N.; Kim, J.-Y.; Kurtis, K. E.; Jacobs, L. J. Measuring Alkali-Silica Reaction (ASR) Microscale Damage in Large-Scale Concrete Slabs Using Nonlinear Rayleigh Surface Waves. J. Nondestruct. Eval. 2017, 36 (2), 29. https://doi.org/10.1007/s10921-017-0410-z.
(36) Kim, G.; Park, S.; Kim, J.-Y.; Kurtis, K. E.; Hayes, N. W.; Jacobs, L. J. Nonlinear Rayleigh Surface Waves to Characterize Microscale Damage Due to Alkali-Silica Reaction (ASR) in Full-Scale, Nuclear Concrete Specimens. Constr. Build. Mater. 2018, 186, 1114–1118. https://doi.org/10.1016/j.conbuildmat.2018.08.022.

(37) Kim, G.; In, C.-W.; Kim, J.-Y.; Jacobs, L. J.; Kurtis, K. E. Nondestructive Detection and Characterization of Carbonation in Concrete; Baltimore, Maryland, USA, 2014; pp 805–813. https://doi.org/10.1063/1.4864904.
(38) Kim, G.; Kim, J.-Y.; Kurtis, K. E.; Jacobs, L. J.; Le Pape, Y.; Guimaraes, M. Quantitative Evaluation of Carbonation in Concrete Using Nonlinear Ultrasound. Mater. Struct. 2016, 49 (1–2), 399–409. https://doi.org/10.1617/s11527-014-0506-1.
(39) Bouchaala, F.; Payan, C.; Garnier, V.; Balayssac, J. P. Carbonation Assessment in Concrete by Nonlinear Ultrasound. Cem. Concr. Res. 2011, 41 (5), 557–559. https://doi.org/10.1016/j.cemconres.2011.02.006.
(40) Eiras, J. N.; Kundu, T.; Popovics, J. S.; Monzó, J.; Borrachero, M. V.; Payá, J. Effect of Carbonation on the Linear and Nonlinear Dynamic Properties of Cement-Based Materials. Opt. Eng. 2015, 55 (1), 011004. https://doi.org/10.1117/1.OE.55.1.011004.
(41) Chen, J.; Bharata, R.; Yin, T.; Wang, Q.; Wang, H.; Zhang, T. Assessment of Sulfate Attack and Freeze–Thaw Cycle Damage of Cement-Based Materials by a Nonlinear Acoustic Technique. Mater. Struct. 2017, 50 (2), 105. https://doi.org/10.1617/s11527-016-0949-7.
(42) Genovés, V.; Soriano, L.; Borrachero, M. V.; Eiras, J.; Payá, J. Preliminary Study on Short-Term Sulphate Attack Evaluation by Non-Linear Impact Resonance Acoustic Spectroscopy Technique. Constr. Build. Mater. 2015, 78, 295–302. https://doi.org/10.1016/j.conbuildmat.2015.01.016.
(43) Genovés, V.; Vargas, F.; Gosálbez, J.; Carrión, A.; Borrachero, M. V.; Payá, J. Ultrasonic and Impact Spectroscopy Monitoring on Internal Sulphate Attack of Cement-Based Materials. Mater. Des. 2017, 125, 46–54. https://doi.org/10.1016/j.matdes.2017.03.068.
(44) Genovés, V.; Carrión, A.; Escobar, D.; Gosálbez, J.; Monzó, J.; Borrachero, M. V.; Payá, J. Nonlinear Acoustic Spectroscopy and Frequency Sweep Ultrasonics: Case on Thermal Damage Assessment in Mortar. J. Nondestruct. Eval. 2019, 38 (3), 61. https://doi.org/10.1007/s10921-019-0599-0.
(45) Payan, C.; Ulrich, T. J.; Le Bas, P. Y.; Saleh, T.; Guimaraes, M. Quantitative Linear and Nonlinear Resonance Inspection Techniques and Analysis for Material Characterization: Application to Concrete Thermal Damage. J. Acoust. Soc. Am. 2014, 136 (2), 537–546. https://doi.org/10.1121/1.4887451.
(46) Yim, H. J.; Kim, J. H.; Park, S.-J.; Kwak, H.-G. Characterization of Thermally Damaged Concrete Using a Nonlinear Ultrasonic Method. Cem. Concr. Res. 2012, 42 (11), 1438–1446. https://doi.org/10.1016/j.cemconres.2012.08.006.
(47) Scalerandi, M.; Griffa, M.; Antonaci, P.; Wyrzykowski, M.; Lura, P. Nonlinear Elastic Response of Thermally Damaged Consolidated Granular Media. J. Appl. Phys. 2013, 113 (15), 154902. https://doi.org/10.1063/1.4801801.
(48) Yang, C.; Chen, J. Fully Noncontact Nonlinear Ultrasonic Characterization of Thermal Damage in Concrete and Correlation with Microscopic Evidence of Material Cracking. Cem. Concr. Res. 2019, 123, 105797. https://doi.org/10.1016/j.cemconres.2019.105797.
(49) Eiras, J. N.; Monzó, J.; Payá, J.; Kundu, T.; Popovics, J. S. Non-Classical Nonlinear Feature Extraction from Standard Resonance Vibration Data for Damage Detection. J. Acoust. Soc. Am. 2014, 135 (2), EL82–EL87. https://doi.org/10.1121/1.4862882.
(50) Kim, J.; Park, S.-J.; Yim, H. Nonlinear Resonance Vibration Assessment to Evaluate the Freezing and Thawing Resistance of Concrete. Materials 2019, 12 (2), 325. https://doi.org/10.3390/ma12020325.
(51) Kim, G.; In, C.-W.; Kim, J.-Y.; Kurtis, K. E.; Jacobs, L. J. Air-Coupled Detection of Nonlinear Rayleigh Surface Waves in Concrete—Application to Microcracking Detection. NDT E Int. 2014, 67, 64–70. https://doi.org/10.1016/j.ndteint.2014.07.004.
(52) Eiras, J. N.; Popovics, J. S.; Borrachero, M. V.; Monzó, J.; Payá, J. The Effects of Moisture and Micro-Structural Modifications in Drying Mortars on Vibration-Based NDT Methods. Constr. Build. Mater. 2015, 94, 565–571. https://doi.org/10.1016/j.conbuildmat.2015.07.078.
(53) Kim, G.; Kim, J.-Y.; Kurtis, K. E.; Jacobs, L. J. Drying Shrinkage in Concrete Assessed by Nonlinear Ultrasound. Cem. Concr. Res. 2017, 92, 16–20. https://doi.org/10.1016/j.cemconres.2016.11.010.

(54) Haralick, R. M.; Shanmugam, K.; Dinstein, I. Texture Features for Image Classification. IEEE Trans. Syst. Man Cybern. 1973, 3 (6), 610–621.
(55) Thibault, G.; Angulo, J.; Meyer, F. Advanced Statistical Matrices for Texture Characterization: Application to Cell Classification. IEEE Trans. Biomed. Eng. 2014, 61 (3), 630–637. https://doi.org/10.1109/TBME.2013.2284600.
(56) Singh, A.; Armstrong, R. T.; Regenauer-Lieb, K.; Mostaghimi, P. Rock Characterization Using Gray-Level Co-Occurrence Matrix: An Objective Perspective of Digital Rock Statistics. Water Resour. Res. 2019, 55 (3), 1912–1927. https://doi.org/10.1029/2018WR023342.
(57) Singh, A.; Regenauer-Lieb, K.; Walsh, S. D. C.; Armstrong, R. T.; Griethuysen, J. J. M.; Mostaghimi, P. On Representative Elementary Volumes of Grayscale Micro-CT Images of Porous Media. Geophys. Res. Lett. 2020, 47 (15). https://doi.org/10.1029/2020GL088594.

Appendix A. Template

Agreed with participants in Task 2 at MAGIC Task 2 kick-off meeting on 9 July 2021

MAGIC deliverable 16.3 (D 16.3) *Selected experiments for assessing the evolution of concrete, their mechanical safety function and performance targets* should be finished before 1 November 2021. D 16.3 should be for each studied type of cementitious material with aggregates (e.g. mortar or concrete):

- How it mechanically functions in the Engineered Barrier System (EBS) for geological disposal of radioactive waste;
- What is the goal of your experiment with this material;
- What information is already available;
- What is your planning.

For each studied type of cementitious material with aggregates studied in MAGIC provide a description of:

1. Mechanical safety function and performance target

The cementitious material with aggregates is used within the EBS to satisfy safety functions. In MAGIC, there is a special interest in the mechanical safety function i.e. what is mechanically the role that the cementitious material performs? An image of the disposal cell where your cementitious material is located can be beneficial in order to understand why this cementitious material is envisaged to be used. A performance target in order to satisfy the mechanical safety function is attached to the description of this safety function. It can be a very simple mechanical property e.g. a minimum in compressive strength. The description of the performance target should elucidate the derivation of the performance target. Also indicate what temperatures your cementitious material can endure in your disposal concept and how these temperatures have been derived. Your expectations of the chemo-mechanical evolution of your cementitious material at disposal conditions are also listed in this Chapter e.g. with a different subheading. This description of the evolution can be very specific such as expected degraded thickness.

2. Size of samples, concrete recipe

Only cementitious materials with aggregates are investigated in Task 2 since this task is dedicated to the study of the chemo-mechanical behaviour at the macroscale taking into account the cement/aggregate behaviour. The size of the samples (and number of the samples) is important for the mechanical analysis. A description of the concrete recipe used to make the samples is highly recommended to be included in your description in order to further identify commonalities and differences between the studied materials in MAGIC and compare their performance. Please indicate your recipe of your cementitious material in kg/m3 for each ingredient in a Table e.g.

Component	Type	kg m^{-3} for each component
Cement	Type of cement	e.g. 400
Water	-	
Aggregate 1	Type of aggregate e.g. sand: size of aggregate (mm)	
Aggregate 2	Type of aggregate: size of aggregate (mm)	
Additive 1 e.g. plasticiser		
Additive 2		

If such a description of a recipe is not possible than highlight other features (e.g. it concerns Roman concrete: the age of the samples where it is found et cetera).

Also indicate the fabrication, curing history et cetera.

3. Available characterisation of cementitious material

Many running experiments have been selected for MAGIC in order to focus on the long-term behaviour of the cementitious material with aggregates. Consequently, it is therefore expected that a lot of characterisation has been performed before MAGIC. Please provide these characterisations in terms of Mechanics, Chemistry and Microbiology (if available) and how these characterisations have been measured and use a separate heading for each property.

3.1 Mechanics

Please describe in this paragraph the available mechanical properties of the studied type of cementitious materials. Please indicate whether it concerns unloaded or loaded cementitious material, intact or damaged. If loaded, indicate a description of the load.

There is a minimum information that needs to be provided i.e. compressive strength and/or Young's modulus for each type of cementitious material after 28 days.

3.1.1 Compressive strength

Provide the reference state of your cementitious materials i.e. after 28 days following NEN-EN-12390-3. For the other available measurements: indicate the number and age of samples during measurement and the exposing environment of the measured cementitious material before the measurement.

3.1.2 Young's modulus

If you do not have a measurement of the compressive strength, then please provide the Young's modulus and how you have measured the Young's modulus.

Additional mechanical properties to be included in this section can tensile strength, creep et cetera.

3.1.3 Porosity

Also properties associated to mechanics can be included in this Chapter for example porosity. An increase in porosity is associated to a decrease in compressive strength. Please not limit your description to the value of the porosity but also indicated how the porosity has been measured. E.g. gravimetry, Mercury porosimetry?

Is the distribution in size of pores also available??

3.1.4 Et cetera other

Other examples than porosity can be permeability of water, diffusion of water. Please also indicate the age of the samples with the value of the measured permeability of water. Other examples are creep and saturation degree.

3.2 Chemistry

Please describe in this paragraph the available chemical knowledge of the studied type of cementitious materials.

3.2.1 Mineralogy

It is very difficult to measured many cementitious minerals with XRD except Portlandite. Please indicate how the mineralogy is measured or derived.

3.2.2 Pore water chemistry

It is also very difficult to measure pore water chemistry of cementitious materials. Please indicate how the pore water chemistry is measured or derived.

3.2.3 Et cetera

Other examples can be redox potential

3.3. Microbiology (if available)

Please provide a description of how the microbial activity is measured.

4. Description of experimental set-up

Please indicate the type of experiment e.g. laboratory or in-situ experiment.

If samples are coming from an Underground Research Facility (URF) than the name of the URF is sufficient if only samples are taken for analysis. A laboratory experiment includes the description of your experimental set-up.

Highlight the goal of your experiment. What is your aim? What are the risks and challenges?

5. Characterisation of cementitious material to be performed in MAGIC

Please provide the characterisations that will be measured in MAGIC similarly as in Chapter 3 in terms of Mechanics, Chemistry and Microbiology (if performed). But in this Chapter also a planning of the determination of these properties needs to be provided. At which dates are the measurements expected? Researchers within MAGIC can use the results if they are aware of your planning.

If samples of cementitious material are made within MAGIC than include a measurement of the compressive strength or Young's modulus after 28 days. If the exposing condition to the cementitious material is changed, provide the mechanical property before the exposure as well as after exposure.

Also similarly as in Chapter 3, how these characterisations will be measured (i.e. .according to which norm) and use a separate heading for each property.

Appendix B. Properties used for the calculations in the description of the Dutch samples

Material	Property	Unit	Value	Source	Value	Source
Concrete	Young's modulus	[GPa]	25	COMSOL Library	33.5	From a compressive strength of 45 N mm^{-2}
	Poisson's ratio		0.20		0.22	(Cloet, Lothenbach et al. 2019)
	Density	[kg m^{-3}]	2300		2450	
	Thermal conductivity	[$Wm^{-1}K^{-1}$]	1.8		2.3 (wet) 1.4 (dry)	
	Heat capacity at constant pressure	[J $kg^{-1}K^{-1}$]	880			
	Thermal expansion	[K^{-1}]	10^{-6}		10^{-6}	
Structural steel	Young's modulus	[GPa]	200		207	
	Poisson's ratio		0.30		0.30	
	Density	[kg m^{-3}]	7850			
	Thermal conductivity	[$Wm^{-1}K^{-1}$]	44.5		52	
	Heat capacity at constant pressure	[J $kg^{-1}K^{-1}$]	475			
	Thermal expansion	[K^{-1}]	12.3×10^{-6}		12×10^{-6}	

Feature	Parameter	Value and unit	Source	Justification / comments
Heat source in CSD-v	Thermal power as a function of time	Watt / canister	(AREVA, 2007)	A polynomial fit is made of the thermal power of the typical residue supplied by the waste processing facility
Heat volume in CSD-v	Volume of heat source	0.17 m^3		Volume of waste
Waste form glass	Heat conductivity	1.02 W $m^{-1}K^{-1}$		At 100°C; that is the minimum available thermal conductivity; the thermal conductivity slightly increases with temperature e.g. at 500°C: 1.25 W $m^{-1}K^{-1}$
	Specific density	2800 kg m^{-3}		
	Specific heat capacity	880 J kg^{-1} K^{-1}		
Stainless steel canister and envelope	Thermal conductivity	16.2 W $m^{-1}K^{-1}$	(Steel, 1986)	AK Steel 304/304 L, at 100°C, datasheet is public available
	Specific density	8030 kg m^{-3}		
	Specific heat capacity	500 J $kg^{-1}K^{-1}$		
Air gap	Thermal conductivity			COMSOL built-in material
	Specific density			
	Specific heat capacity			
Overpack Carbon steel	thermal conductivity	44.5 W $m^{-1}K^{-1}$		COMSOL built-in material
	specific density	7850 kg m^{-3}		
	specific heat capacity	475 J $kg^{-1}K^{-1}$		
Filler + concrete buffer and gallery	thermal conductivity	1.8 $Wm^{-1}K^{-1}$		COMSOL built-in material; similar values in the Belgian programme (Weetjens 2009)
	specific density	2300 kg m^{-3}		
	specific heat capacity	880 J $kg^{-1}K^{-1}$		
Foamed concrete	thermal conductivity	0.80 W $m^{-1}K^{-1}$	(CUR, 1995)	Density 1600 kg m^{-3}: wet 0.80 W/mK 95% RH
	specific density	1600 kg m^{-3}		Tailor-made product with a compressive strength at least 10 MPa to accommodate lithostatic pressure at 500 metre depth
	specific heat capacity	840 J $kg^{-1}K^{-1}$	Joostdevree.nl	Wet larger than dry due to large heat capacity of water
Host rock Boom Clay	thermal conductivity	1.45 W $m^{-1}K^{-1}$	(Weetjens, 2009)	Combination of horizontal and vertical conductivity
	specific density	2000 kg m^{-3}	(Mazurek et al, 2003)	Results from large scale in-situ test in a clay pit; water-saturated Boom Clay p.230; also in NIROND,2013 p.89
	specific heat capacity	1420 J $kg^{-1}K^{-1}$	(NIROND, 2013)	Deduced from 2.84×10^6 J $m^{-3}K^{-1}$ see p.125 in NIROND
	temperature	299.15 K	Verweij et al., 2016)	Generic temperature of Boom Clay at 500 metre depth in range 22°C to 26°C; chosen 26°C

For vitrified waste, decay of many short-lived radionuclides takes place in the period smaller than 30 years. Their contribution to the thermal power is assumed not be included in the following figure from AREVA that shows the heat generating power per waste canister as a function of time.

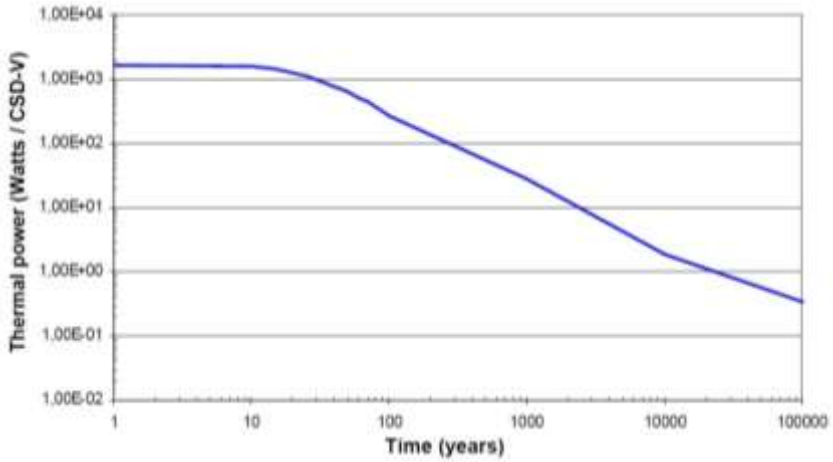

A polynomial needs to be made for the implementation of the thermal power into a calculation. The thermal power is a sum of exponentials:

$$Q(t) = \sum_i A_i e^{\alpha_i [t + t_{storage}]}$$

The coefficients obtained with a fit by the eye are shown in the next table for a storage period, $t_{storage}$, of 0 years. Coefficients to use in a sum exponentials for thermal power of CSD-v as a function of time; A_i in Watts/CSD-v and α in year^{-1}.

	A1	A2	A3	α_1	α_2	α_3
[Watt/canister]	1637	200	15	-0.025	-0.0025	-0.00025

There are other coefficients available in literature. The use of these of these other coefficients may underestimate the heating power as a function of time. For example, vitrified HLW was named UC-V in the 6th framework programme RED-IMPACT (Greneche et al., 2007). The following figure shows the currently used thermal power as a function of time compared to the one extracted from RED-IMPACT.

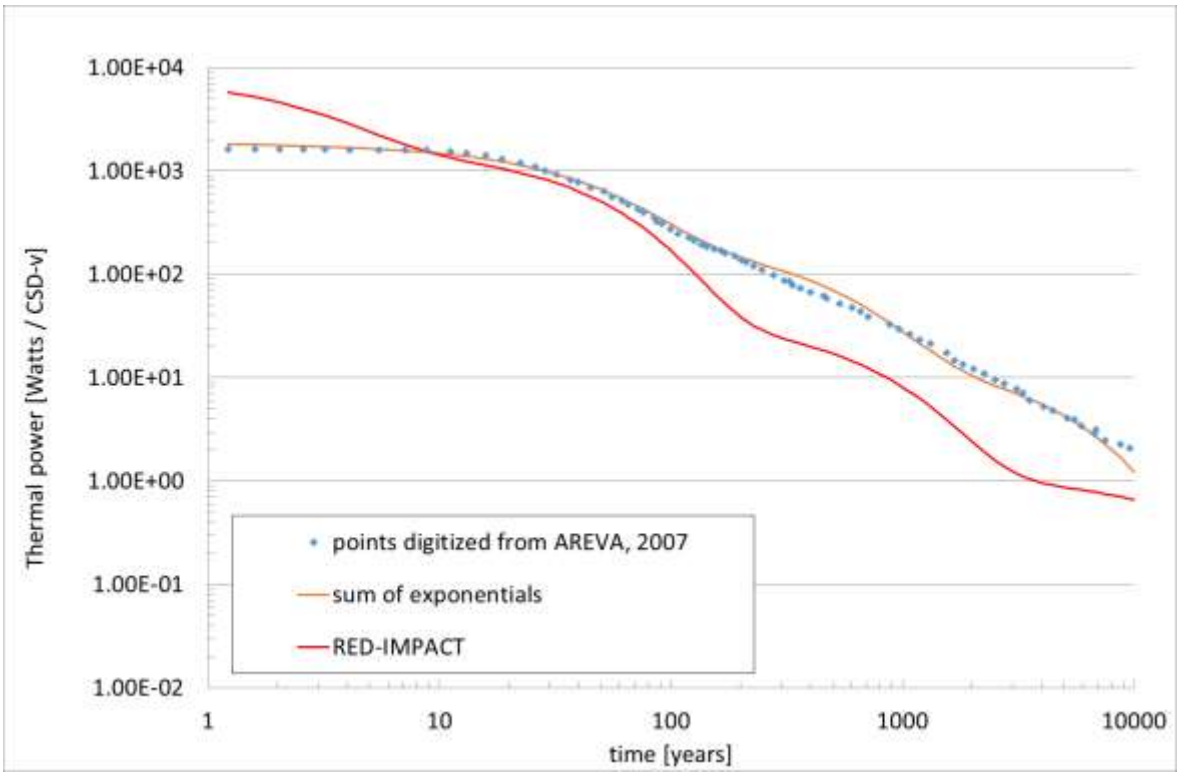
1.00E+04
1.00E+03
1.00E+02
1.00E+01
1.00E+00
1.00E-01
1.00E-02
Thermal power [Watts / CSD-v]
1
10
100
1000
10000
time [years]
points digitized from AREVA, 2007
sum of exponentials
RED-IMPACT